

**INCLUSIVE PION SINGLE CHARGE EXCHANGE IN  ${}^4\text{He}$   
IN THE  $\Delta$ -RESONANCE REGION**

by

Mark Yu Da Wang  
S.B., Massachusetts Institute of Technology  
1987

Submitted to the Department of Physics  
in partial fulfillment of the requirements for the degree of

**DOCTOR OF SCIENCE**

at the

**MASSACHUSETTS INSTITUTE OF TECHNOLOGY**  
September 1994

© Massachusetts Institute of Technology 1994

Signature of author \_\_\_\_\_

Department of Physics  
September 6, 1994

Certified by \_\_\_\_\_

June L. Matthews  
Thesis Supervisor

Accepted by \_\_\_\_\_

George F. Koster  
Chairman, Graduate Committee

MASSACHUSETTS INSTITUTE  
OF TECHNOLOGY

OCT 14 1994

LIBRARIES

Science



INCLUSIVE PION SINGLE CHARGE EXCHANGE IN  ${}^4\text{He}$   
IN THE  $\Delta$ -RESONANCE REGION

by

Mark Yu Da Wang

Submitted to the Department of Physics on September 6, 1994

in partial fulfillment of the requirements

for the Degree of

Doctor of Science

The doubly-differential cross sections,  $d^2\sigma/d\Omega dE$ , for the inclusive  ${}^4\text{He}(\pi^-, \pi^0)X$  reaction have been measured with outgoing  $\pi^0$  spectra measured at angles of  $30^\circ$ ,  $50^\circ$ ,  $80^\circ$ ,  $105^\circ$ , and  $130^\circ$  for an incident beam energy of 160 MeV. The angular distribution,  $d\sigma/d\Omega$ , and total cross section,  $\sigma$ , are presented as well. The data were taken during an experiment performed at the Clinton P. Anderson Meson Physics Facility at the Los Alamos National Laboratory (LAMPF) using a liquid He target and the LAMPF  $\pi^0$  spectrometer.

This measurement is of pion single-charge-exchange (SCX), which, along with double-charge-exchange (DCX) and inelastic scattering (where the pion does not change charge), is one of three possible reactions leading to a pion in the final state. In  ${}^4\text{He}$ , measurements of the other two reactions have been performed in the  $\Delta$ -resonance region, where scattering is affected by the strong  $\Delta(1232)$  resonance in the  $\pi - N$  system. The data presented in this thesis allow for a direct comparison of the reaction mechanisms for each process.

Inelastic scattering in  ${}^4\text{He}$  is dominated by scattering from a single nucleon or quasifree scattering, while double-scattering dominates DCX (two like nucleons are required by charge conservation for this reaction to occur). Pion absorption is a competing reaction, as higher-order scattering processes leading to a pion in the final state are made improbable due to the strong possibility the pion will be absorbed at each interaction. SCX, however, cannot proceed through the intermediate  ${}^5S_2$   $\Delta - N$  state, which is the primary two-body absorption channel, due to isospin, parity, and angular momentum arguments.

The data show that SCX in  ${}^4\text{He}$  is dominated by quasifree scattering. The angular distribution supports this as it resembles SCX from the free proton at backward scattering angles. At forward angles, the angular distribution is suppressed by Pauli blocking. A comparison between the doubly-differential cross sections for SCX and inelastic scattering indicates that (1) the magnitudes follow those predicted by simple isospin arguments, (2) the scattering processes behind both are very similar. Calculations based on the plane wave impulse approximation and distorted wave impulse approximation (PWIA and DWIA) have been made of the cross section for the SCX reaction. The more realistic DWIA calculation agrees reasonably well with the data.

Thesis Supervisor: Dr. June Matthews  
Title: Professor of Physics



# Acknowledgments

I would like to thank many people for their help and support during my graduate school days. The successful completion of this thesis could not have been possible without their help.

First, I would like to thank Professor June Matthews who, as both my bachelors and doctoral thesis advisor, has been the most influential person in my academic development. During the many experiments I have participated on as a member of her research group, I often chose to sit overlapping shifts with June because it always proved to be an intense educational experience to be kept so focussed and alert. Later, during the years of data replay and the writing of this thesis, I learned from her the care and persistence required to harvest the joys of research. Finally, I appreciated her interest in my personal as well as academic life.

Professor Edward Kinney of the University of Colorado (B-B-Q Ralphie!) deserves enormous thanks not only for being the co-spokesperson on this experiment, but also for being a close friend. I've always felt our similar backgrounds made for excellent compatibility. He has been the most patient of friends, and his unwavering support really was undeserved.

This experiment and the others I've participated on at LAMPF could never have been successful without the efforts of many, and the collaborators who participated on this experiment did a Herculean job. Peter Gram was a surrogate advisor from LAMPF since 1986 and many times showed me a different face of physics research. Wilson Fong made a major contribution by trying pencil erasers to clean PCOS contacts! He was also an ideal roommate and tennis partner. Thanks for many hours of lost sleep to Marla Dowell, Hojoon Park, Mark Whitton, and Don Roberts. Thanks to Jim Knudson for his help with the spectrometer and his wonderful electronics diagram. The cryogenics crew at LAMPF, especially Rudy, Larry, and Jan, made heroic efforts to save this experiment after the May 26, 1990 target disaster. Cole Smith from UVA (nice car!) should be included in this group of lifesavers.

Much of the code used during data acquisition and data replay were from Steinar Høibråten.

He, along with Stephen Pate and Chris Maher, were three postdocs who were tremendous friends as well as colleagues. Two of them can actually play a little basketball (one went to basketball camp, in fact). More code used during the analysis of the results came from Mark Yuly, who provided almost immediate responses to my cries for help these last few months.

It's been a privilege to be at MIT with some wonderful faculty members. Thanks to Professors Redwine and Bernstein for being on my thesis committee and for critiquing my thesis. It was Bob's comment, "Your thesis only benefits you through its completion" which made graduating much more urgent. Professor Moniz's 8.712 class was the best physics course I had ever had.

There are many other graduate students who have been cool too. The two at the top of the list are Bill (Whoa! Whoa!) Schmitt and Chung-Pei Ma, who both became good friends and frequent eating partners. Richard Florizone made sure I ate well after they graduated.

Joanne Gregory deserves a line to herself (and an institute award) for all her help.

I need to acknowledge, of course, many people who made me smile but who aren't associated with physics. My years as a floor tutor in Baker House were the four happiest years of my life. Thanks Professor Watson and Myra, Sylvain and Susie, Don, Dava, Deirdre, Steve B., Steve S., Steve W. and Elizabeth. Thanks to the gang: Gloria, Giang, Masa, Jim (swish!), Ann, Ji, Augie, Per, Raj S., Raj P., Chris S., Sherk. Thanks Jackie M., Jina (hope you're doing well, wherever you are), Eddie (dUde), Alice, Andria P., Mike & Stella. Thanks to my housemates: Lou, Karen, Robert, and Mike. The last of the old-timers from MacGregor, Eric Twietmeyer and Pat Lord, have also now gotten their degrees.

This thesis represents the completion of the last of three goals I set before myself about three years ago; the others involved my personal and family relationships. My closest friend since 1985 and bride, Sally Chung, has given me steadfast support to bridge the oceans between us. My sister, Cindy, planned our wedding while I worked to finish up this thesis. Frank and Judy helped more than they will ever know. My parents and I have begun a new relationship, and even though they have moved twelve time zones away, we are closer than ever.

*You will be vacationing  
in Monte Carlo.*

A fortune cookie prophecy I received Summer 1987,  
just before entering graduate school.





# Table of Contents

Abstract .....	3
Acknowledgments.....	5
Table of Contents .....	9
List of Figures .....	11
List of Tables .....	14
Chapter 1: Introduction .....	15
1.1 The Pion and the Strong Force.....	15
1.2 Overview of Pion Physics at Intermediate Energies.....	17
1.3 Pion-Nucleon Reactions in the $\Delta$ -Resonance Region .....	20
1.3.1 Pion-Nucleon Scattering Cross Sections .....	22
1.3.2 Angular Dependence of Pion-Nucleon Reactions .....	24
1.4 Pion – Nucleus Inelastic Scattering .....	26
1.5 Pion Absorption .....	31
1.6 Pion Double-Charge-Exchange in Nuclei.....	32
1.7 Pion Single-Charge-Exchange in Nuclei .....	38
1.8 Scientific Motivation for this Measurement .....	45
Chapter 2: Experimental Setup and Procedures.....	47
2.1 Incident Beam .....	47
2.1.1 Beam Monitoring .....	50
2.1.2 Calibration of the Ionization Chamber: Activations .....	51
2.2 Cryogenic Target .....	54
2.3 The Detector: The LAMPF $\pi^0$ Spectrometer .....	57
2.3.1 Detection Principle.....	57
2.3.2 Detector Design .....	59
2.3.3 Wire Chambers .....	61
2.3.4 Spectrometer Setup.....	62
2.4 Event Trigger and Electronics .....	66
2.4.1 Recorded Information and Software .....	68
2.4.2 Coincidence Timing.....	69
2.4.3 Pedestals and Stabilization.....	69
2.5 Normalization and Conversion Efficiencies .....	70
Chapter 3: Data Analysis .....	73
3.1 Determination of the Incident Pion Flux .....	75
3.2 Determination of $\pi^0$ Yield .....	76
3.2.1 Pb-glass Analysis .....	78

3.2.2 Time Resolution: Elimination of Random Events .....	80
3.2.3 Wire Chamber Analysis .....	82
3.2.4 Hot Wires .....	85
3.2.5 Wire Chamber Efficiencies .....	85
3.3 XCUT .....	88
3.4 Calculating the Acceptance of the Spectrometer .....	93
3.4.1 Photon Attenuation Losses .....	97
3.5 Conversion Efficiencies .....	100
3.6 Determination of Systematic Errors .....	107
 Chapter 4: Experimental Results .....	 109
4.1 Presentation of the Data .....	109
4.2 Doubly-Differential Cross Sections .....	111
4.3 Singly-Differential Cross Sections .....	119
4.4 Total Cross Section .....	120
 Chapter 5: Discussion of SCX Results .....	 121
5.1 Effective Number of Nucleons: $N_{\text{eff}}$ .....	121
5.1.1 Pauli Blocking .....	122
5.2 SCX Quasifree Peaks .....	123
5.3 Comparison with inelastic scattering data .....	126
5.4 Impulse Approximation Calculations .....	134
5.4.1 Impulse Approximation Formalism .....	134
5.4.2 Distorted Wave Impulse Approximation (DWIA) .....	136
5.4.3 Initial Energy and Final Energy Prescriptions .....	138
5.4.4 Plane Wave Impulse Approximation (PWIA) .....	138
5.5 Comparison of the Data with the Calculation .....	139
 Chapter 6: Summary and Conclusions .....	 151
 Appendix A: SCX on a T=0 Pair of Nucleons .....	 155
 Appendix B: Correction for Ionization Chamber Gating .....	 157
 Appendix C: Piang Modification Details .....	 161
 Appendix D: Tables of Cross Sections .....	 167
 Bibliography .....	 173
 Biographical Note .....	 179

## List of Figures

Figure 1.1: Pion inelastic and charge-exchange reactions .....	17
Figure 1.2: Schematic picture of the $\Delta$ -N reaction mechanism .....	19
Figure 1.3: Pion-Nucleon reactions and the $\Delta(1232)$ resonance .....	21
Figure 1.4: Total cross sections for elastic scattering and SCX in the $\Delta$ -resonance region .....	24
Figure 1.5: The differential cross section for $\pi^-p \rightarrow \pi^0n$ at 160 MeV .....	26
Figure 1.6: Doubly differential cross sections for ${}^4\text{He}(\pi^+, \pi^+)X$ at 180 MeV .....	28
Figure 1.7: Differential cross sections for ${}^4\text{He}(\pi^+, \pi^+)X$ and ${}^4\text{He}(\pi^-, \pi^-)X$ .....	30
Figure 1.8: Doubly differential cross sections for ${}^3\text{He}(\pi^-, \pi^+)X$ and for ${}^4\text{He}(\pi^+, \pi^-)X$ at $25^\circ$ ...	34
Figure 1.9: Calculations by E. Kinney for the ${}^4\text{He}(\pi^+, \pi^-)X$ reaction at 240 MeV and $25^\circ$ .....	35
Figure 1.10: Cross sections for $(\pi^+, \pi^-)$ DCX on several nuclei at 240 MeV and $25^\circ$ .....	37
Figure 1.11: Cross sections for ${}^4\text{He}(\pi^+, \pi^-)4p$ and ${}^{16}\text{O}(\pi^+, \pi^-)X$ at 240 MeV and $25^\circ$ .....	38
Figure 1.12: Single charge exchange on a T=0 nucleon pair.....	39
Figure 1.13: Doubly differential cross sections for inclusive SCX on a range of nuclei .....	40
Figure 1.14: Cross sections for ${}^{16}\text{O}(\pi^+, \pi^0)X$ and ${}^{16}\text{O}(\pi^+, \pi^+)X$ at $T_{\pi^+} = 163$ MeV .....	42
Figure 1.15: Differential cross sections for the inclusive SCX reaction on a range of nuclei.....	43
Figure 1.16: Angular distribution of the ${}^3\text{He}(\pi^-, \pi^0)$ reaction at 200 MeV .....	45
Figure 2.1: Experimental Area A at LAMPF.....	48
Figure 2.2: Photograph of the East cave at the P <sup>3</sup> channel in experimental hall A.....	49
Figure 2.3: Diagram of the beam transport elements for the P <sup>3</sup> channel .....	49
Figure 2.4: Diagram of the beam monitoring devices .....	51
Figure 2.5: Diagram of the scintillator activation detector setup.....	53
Figure 2.6: Photograph of the cryogenic ${}^4\text{He}$ target with the nickel vacuum vessel .....	55
Figure 2.7: Schematics of the cryogenic target with both vacuum vessels .....	56
Figure 2.8: $\pi^0$ decay photons in the center-of-mass and laboratory frames .....	58
Figure 2.9: Photograph of the LAMPF $\pi^0$ spectrometer.....	63
Figure 2.10: Schematic of the LAMPF $\pi^0$ spectrometer .....	64
Figure 2.11: Diagram of opening angles and detector setup .....	65
Figure 2.12: Diagram of the $\pi^0$ event trigger circuit.....	67

Figure 2.13: Diagram of the $\pi^0$ event enable circuit .....	68
Figure 3.1: Summary of activation data.....	76
Figure 3.2: An ADC spectrum which displays evidence of a pedestal shift.....	80
Figure 3.3: Plot of the time resolution of the spectrometer .....	81
Figure 3.4: Flowchart illustrating logic involving the wire chambers.....	83
Figure 3.5: Traceback in each place of three wire chambers.....	84
Figure 3.6: The X distribution for $\pi^0$ s of 96 MeV .....	89
Figure 3.7: The X distributions for $\pi^0$ s of 113 MeV and 140 MeV .....	90
Figure 3.8: XCUT limit as a function of $\pi^0$ energy .....	92
Figure 3.9: Typical kinetic energy spectrum for a data run .....	94
Figure 3.10: Spectrometer acceptance for detecting $\pi^0$ s in three $10^\circ$ scattering bins .....	96
Figure 3.11: Spectrometer acceptance for the $\eta = 70^\circ$ (setup A) and $\eta = 95^\circ$ setups .....	100
Figure 3.12: $\pi^0$ energy spectra from $\text{CH}_2$ and $^{12}\text{C}$ at $80^\circ$ .....	102
Figure 3.13: Proton yields from the normalization measurements .....	103
Figure 3.14: Conversion Efficiencies for XCUT=0.25.....	104
Figure 3.15: Conversion Efficiencies for XCUT=0.50.....	106
Figure 4.1: Doubly-differential cross sections for ${}^4\text{He}(\pi^-, \pi^0)\text{X}$ at 160 MeV and $30^\circ$ .....	114
Figure 4.2: Doubly-differential cross sections for ${}^4\text{He}(\pi^-, \pi^0)\text{X}$ at 160 MeV and $50^\circ$ .....	115
Figure 4.3: Doubly-differential cross sections for ${}^4\text{He}(\pi^-, \pi^0)\text{X}$ at 160 MeV and $80^\circ$ .....	116
Figure 4.4: Doubly-differential cross sections for ${}^4\text{He}(\pi^-, \pi^0)\text{X}$ at 160 MeV and $105^\circ$ .....	117
Figure 4.5: Doubly-differential cross sections for ${}^4\text{He}(\pi^-, \pi^0)\text{X}$ at 160 MeV and $130^\circ$ .....	118
Figure 4.6: Differential cross section for ${}^4\text{He}(\pi^-, \pi^0)\text{X}$ at 160 MeV .....	119
Figure 4.7: Calculation of total cross section for ${}^4\text{He}(\pi^-, \pi^0)\text{X}$ at 160 MeV .....	120
Figure 5.1: Determination of $N_{\text{eff}}$ from differential cross section .....	122
Figure 5.2: Fits used to determine the centroid and width of the SCX quasifree peak. ....	125
Figure 5.3: Doubly-differential cross section for ${}^4\text{He}(\pi^+, \pi^+)\text{X}$ at 160 MeV and $50^\circ$ .....	126
Figure 5.4: Doubly-differential cross section for ${}^4\text{He}(\pi^+, \pi^+)\text{X}$ at 160 MeV and $130^\circ$ .....	127
Figure 5.5: Comparison at $50^\circ$ of ${}^4\text{He}(\pi^-, \pi^0)\text{X}$ and ${}^4\text{He}(\pi^+, \pi^+)\text{X}$ at 160 MeV .....	130

Figure 5.6: Comparison at 130° of ${}^4\text{He}(\pi^-, \pi^0)\text{X}$ and ${}^4\text{He}(\pi^+, \pi^+)\text{X}$ at 160 MeV .....	130
Figure 5.7: Comparison of SCX, DCX and inelastic scattering at 50° .....	133
Figure 5.8: Quasifree scattering diagram for the $\text{A}(\pi, \pi'\text{N})\text{S}$ reaction.....	135
Figure 5.9: Results of the PWIA and DWIA calculations .....	140
Figure 5.10: Comparison of DWIA results with data at 30° .....	142
Figure 5.11: Comparison of DWIA results with data at 50° .....	143
Figure 5.12: Comparison of DWIA results with data at 80° .....	144
Figure 5.13: Comparison of DWIA results with data at 105° .....	145
Figure 5.14: Comparison of DWIA results with data at 130° .....	146
Figure 5.15: Semilogarithmic plot of DWIA results at 30°, 50°, and 80° .....	147
Figure 5.16: Semilogarithmic plot of DWIA results at 105° and 130° .....	148
Figure 5.17: Comparison of angular distribution of DWIA results with data .....	149
Figure A-1: SCX on a T=0 pair of nucleons.....	155
Figure B-1: Linear relationship for improperly-gated ionization chamber counts .....	158
Figure C-1: Diagram of cryogenic target with the nickel vacuum vessel.....	162
Figure C-2: Diagram of cryogenic target with the mylar vacuum vessel .....	163
Figure C-3: Diagram of the large Fe plate of the support stand .....	164

## List of Tables

Table 2.1: Spectrometer setup parameters .....	66
Table 3.1: Typical values for wire chamber efficiencies .....	88
Table 4.1: Combinations of vacuum vessels and background target cells .....	110
Table 5.1: Positions and widths of SCX quasifree peaks .....	124
Table B-1: Slope and intercept for ionization chamber counts .....	158
Table C-1: Dimensions and coordinates of cryogenic target with nickel vacuum vessel .....	165
Table C-2: Dimensions and coordinates of cryogenic target with mylar vacuum vessel .....	166
Table D-1: Doubly-differential cross sections for ${}^4\text{He}(\pi^-, \pi^0)\text{X}$ at 160 MeV and $30^\circ$ .....	167
Table D-2: Doubly-differential cross sections for ${}^4\text{He}(\pi^-, \pi^0)\text{X}$ at 160 MeV and $50^\circ$ .....	168
Table D-3: Doubly-differential cross sections for ${}^4\text{He}(\pi^-, \pi^0)\text{X}$ at 160 MeV and $80^\circ$ .....	169
Table D-4: Doubly-differential cross sections for ${}^4\text{He}(\pi^-, \pi^0)\text{X}$ at 160 MeV and $105^\circ$ .....	170
Table D-5: Doubly-differential cross sections for ${}^4\text{He}(\pi^-, \pi^0)\text{X}$ at 160 MeV and $130^\circ$ .....	171

## Chapter 1: Introduction

This thesis presents a measurement of inclusive pion single-charge-exchange in  ${}^4\text{He}$  in the  $\Delta$ -resonance region. Chapter 1 presents a brief overview of pion (scattering) physics, the  $\Delta$ , and the scientific motivations for studying this reaction. In chapter 2, the experimental set up, equipment, and procedures used in the measurement are described. The subsequent data analysis is presented in chapter 3, and the results of the experiments are discussed in chapter 4. The data are compared with the inclusive pion inelastic scattering cross section, predictions based on simple isospin arguments, and theoretical calculations based on the impulse approximation in chapter 5. A brief conclusion is presented in chapter 6.

### 1.1 The Pion and the Strong Force

The four fundamental forces of nature are gravity, the weak force, the electromagnetic force (the last two combined into the electroweak force), and the strong force. Associated with each is a mediator, which are respectively gravitons (undiscovered),  $W^\pm$  and  $Z^0$  bosons, photons, and gluons. Currently, the theory of quantum chromodynamics (QCD) best describes the interactions between quarks, the constituent particles of the strong force, through their exchange of gluons. Free quarks and gluons are thought not to exist in nature; in QCD, both have “color,” and it is believed that real particles must be “colorless.” This is possible by grouping three quarks so that the colors of each combine so the total is colorless, and nucleons are the lightest three-quark constructs possible. Colorless particles may also be created with a quark-antiquark pair in which case the color of the quark cancels with that of its antiparticle. Mesons are described as these quark-antiquark constructs.

For processes in which the composite nature of nucleons and mesons is not exposed, it is sufficient to base a description in terms of the hadronic NN interaction as mediated by mesons. Nuclei are described as collections of nucleons, either protons or neutrons,

which are bound together through their continuous exchange, emission and absorption, of mesons. This is possible because the pion is a spinless particle (a boson) and can be created and absorbed by nucleons within the nucleus in a manner not accessible to spin  $\frac{1}{2}$  baryons and leptons. The mesons resident within the nucleus must be “virtual,” in which case Einstein’s energy-mass relationship is violated for a short period of time as limited by the Heisenberg uncertainty principle. The maximum period of time a virtual meson may exist without violating this principle is given by the expression:

$$t = \frac{\hbar}{mc^2}. \quad (1-1)$$

The range of influence of any virtual meson, or the maximum distance it can travel in this period of time, is correspondingly limited by the uncertainty principle, as given by:

$$x = ct = \frac{\hbar c}{mc^2}. \quad (1-2)$$

In 1935, Yukawa<sup>1</sup> argued that the limited range of the NN interaction to distances on the order of the size of the atomic nucleus ( $\sim 1 \text{ fm} = 10^{-15} \text{ m}$ ) necessitated a mediator whose mass was about  $200 \text{ MeV}/c^2$ . After the initial misidentification as a meson of the muon, a particle later identified as a lepton of similar mass, the pion was discovered in 1947<sup>2,3,4</sup>.

The pion is a pseudoscalar (spin  $S_\pi = 0$ , negative intrinsic parity  $P_\pi = -1$ ), isovector (isospin  $T_\pi = 1$ ) particle. The two charged pions have masses of  $m_{\pi^+} = m_{\pi^-} = 139.6 \text{ MeV}/c^2$ , a mean lifetime of  $\tau_{\pi^+} = \tau_{\pi^-} = 26 \cdot 10^{-9} \text{ s}$ , and primary decay channels  $\pi^+ \rightarrow \mu^+ + \nu_\mu$  and  $\pi^- \rightarrow \mu^- + \bar{\nu}_\mu$ . The neutral pion has a somewhat lighter mass of  $m_{\pi^0} = 135.0 \text{ MeV}/c^2$ , a much shorter lifetime of  $\tau_{\pi^0} = 8.4 \cdot 10^{-17} \text{ s}$ , and a primary decay channel  $\pi^0 \rightarrow \gamma\gamma$ . The mass difference between the charged and neutral pions is thought to be the result of Coulomb effects, and the difference in lifetimes reflects the relative strengths of the weak and electromagnetic forces which govern the two decay channels. The term meson, derived from Greek origins to mean “middle,” reflects the



mass of the pion, as it is between the electron's mass of  $0.511 \text{ MeV}/c^2$  and that of nucleons, either protons or neutrons, whose masses are about  $940 \text{ MeV}/c^2$ . As the lightest meson, the pion is energetically favored to be created over heavier mesons, and it is thought to mediate the important long-range part of the NN force. The heavier  $\rho$ - and  $\omega$ -mesons contribute to the short-range nuclear interaction.

## 1.2 Overview of Pion Physics at Intermediate Energies

While the virtual pion may be resident within the nucleus, it can also exist as a real particle before decaying via the weak or electromagnetic interaction. Since the early 1970's, the construction of three "meson factories"<sup>5</sup> (LAMPF in Los Alamos, New Mexico; TRIUMF in Vancouver, British Columbia; and PSI in Zürich, Switzerland) have allowed scientists to use intense beams of pions to study the nucleus, mesons, and the forces which govern their interactions. The pion is used as a projectile incident upon a chosen target nucleus, and the distributions of energies and scattering angles of the outgoing particles are then measured to learn about the collision between pion and nucleus.

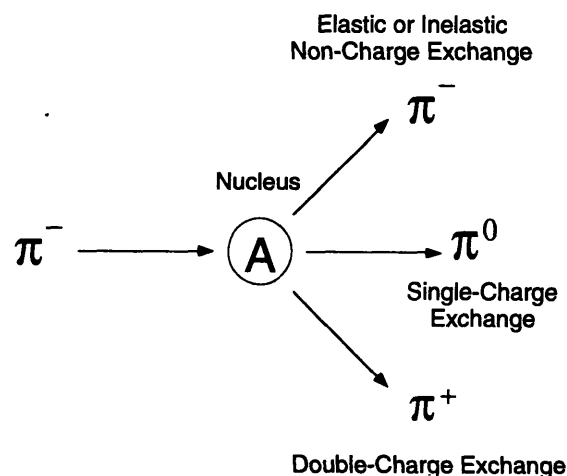


Figure 1.1: The pion can be used as an incident projectile upon a target nucleus to probe aspects of the nuclear force. Since the pion has three charge states to which it can scatter, there are three categories of charge-exchange experiments which are possible. This thesis presents a measurement of pion single-charge-exchange on the  ${}^4\text{He}$  nucleus.

Because the pion has three charge states,  $+1$ ,  $0$ ,  $-1$  in units of the electron charge, an incident charged pion may scatter from the nucleus in one of three ways to produce an outgoing pion, as illustrated in figure 1.1. First, if the scattering results in a pion of the same charge being detected, it is an inelastic scattering reaction, which for illustrative purposes may be thought of as a non-charge-exchange (NCX) reaction. Secondly, if a pion of the opposite charge is detected, two units of charge have been exchanged between a pion and an atomic nucleus, and the reaction is a double-charge-exchange (DCX) reaction. Pion single-charge-exchange (SCX) is the third reaction in which one unit of charge is exchanged and a neutral pion is detected. These reactions are three of the fundamental components of the pion-nucleus total cross section, a measure of the interaction probability between the incident pion and nuclear target.

An important question in pion-nucleus scattering is “How many nucleons are involved in a pion scattering reaction?” Due to the strength of the  $\pi N$  interaction, multiple-scattering effects<sup>6</sup>, in which the pion interacts with more than one nucleon in the nucleus before emerging, are guaranteed to be important. For illustration, the outgoing pion from a SCX reaction may have survived several scatterings before emission from a nucleus, both non-charge-exchange and charge-exchange, so that a total of one unit of charge is transferred. Or the pion may have only interacted once with the nucleus. Similarly, it is possible that an inelastic scattering or DCX reaction may be the result of multiple interactions, either charge-exchange or not, so that the emerging (and detected) pion has exchanged a total of zero or two units of charge respectively. It is difficult to determine experimentally which history is correct for any particular detected particle, and measurements of these reactions include contributions from single and multiple scattering. A major goal in studying pion charge-exchange and inelastic scattering reactions is thus to understand the contributions to the cross section from single versus multiple scattering.

The investigation of multiple scattering is connected to the study of pion absorption, a process in which there is no outgoing pion. Whether virtual or real, pions can be created and absorbed by nucleons; since the coupling constant is the same in either case<sup>7</sup>, using

real pions as a nuclear probe provides a method for studying this fundamental aspect of the nuclear system. Absorption is a competing reaction in that the annihilation of the particle prevents the completion of any multiple-scattering sequence leading to inelastic scattering, SCX, or DCX. As will be discussed in greater detail below, inelastic scattering is primarily a single-scattering reaction because absorption makes multiple-scattering processes less probable. DCX, on the other hand, must be a multiple-scattering process in that two nucleons are required to maintain charge conservation. SCX, while not requiring multiple interactions, is not as affected by absorption as inelastic scattering (the argument is presented in appendix A) and may show added signs of multiple scattering. The complementary study of these four processes may lead to a new understanding of the physical processes behind pion-nucleus reactions and the strong force which governs them.

For pions of any charge, all pion-nucleus scattering reactions at intermediate energies,  $T_\pi = 100 - 300$  MeV, are affected by the  $\Delta(1232)$  resonance in the  $\pi - N$  system. Due to the strength of this resonance, a complete description of inelastic scattering, DCX, and SCX reactions in this energy region must incorporate  $\Delta$  production, propagation within the nuclear medium, and decay. Typically, the  $\pi N$  interaction produces an intermediate  $\Delta$  which decays to  $\pi'N'$ . The  $\Delta$  is also a hadron and may interact with a nucleon before decay, and a description of the  $\Delta N$  interaction (shown schematically in figure 1.2) is of great interest in pion physics.

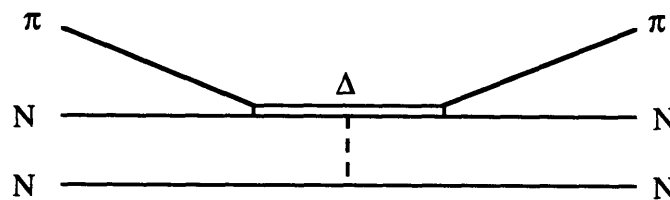


Figure 1.2: Schematic picture of the  $\Delta$ -N reaction mechanism.

An inclusive reaction is one in which the exact final state of the residual system is not determined. (The counterpart to inclusive reactions are exclusive reactions in which a

particular final nuclear state is observed.) For the  ${}^4\text{He}$  nucleus, the residual system, after one unit of charge has been exchanged with the scattered pion, must either be “nnnp” or “pppn,” neither of which exists in stable nuclear form. By making an inclusive measurement, the various unbound final nuclear states all contribute to the cross section, and the results are thought to be less sensitive to details of nuclear structure.

Inclusive pion single charge exchange in  ${}^4\text{He}$  in the  $\Delta$ -resonance region involves the  $\pi\text{N}$  and  $\Delta\text{N}$  interactions in this fundamental reaction. In addition,  ${}^4\text{He}$  is a few-body nucleus whose structure is thought to be understood, making theoretical calculations possible for comparison. Previous inclusive measurements of inelastic scattering and DCX scattering in  ${}^4\text{He}$  exist, and a comparison with SCX is vital in developing a consistent picture of pion-nucleus interactions in this system. The comparison between inelastic scattering and SCX is particularly interesting because absorption is less strongly coupled to the charge-exchange reaction which may show greater indications of multiple scattering. These data, in conjunction with previous measurements of all three reactions on heavier nuclei, aid our understanding of how SCX and the  $\pi\text{N}$  interaction are modified with the addition of nucleons.

### 1.3 Pion-Nucleon Reactions in the $\Delta$ -Resonance Region

The  $\Delta(1232)$  resonance (also known as the  $\Delta_{33}$  resonance) was first discovered by Enrico Fermi in 1951<sup>8</sup> when a large and dramatic resonance in the  $\pi^+ - \text{p}$  scattering cross section was observed. The  $\Delta$  affects all  $\pi - \text{N}$  reactions involving a total energy of 1.1 GeV to 1.3 GeV (figure 1.3). It is viewed in constituent models as resulting from the spin flip transition of one quark within the nucleon, though its composite makeup of three quarks is not exploited in the measurement presented in this thesis.

The lifetime of the  $\Delta$  is extremely short, on the order of  $10^{-23}$  seconds, since the strong interaction is responsible for its decay, and its width is correspondingly large due to the

Heisenberg uncertainty principle. Specific quantum numbers for spin  $J_\Delta = \frac{3}{2}$  and isospin  $T_\Delta = \frac{3}{2}$  can be assigned to the resonance, and for that reason, it is also treated as a particle in theoretical formalism. There are four charge states for the resonance,  $\Delta^{++}$ ,  $\Delta^+$ ,  $\Delta^0$ , and  $\Delta^-$ , corresponding to the four charge combinations possible from three pion charge states and two nucleon charge states.

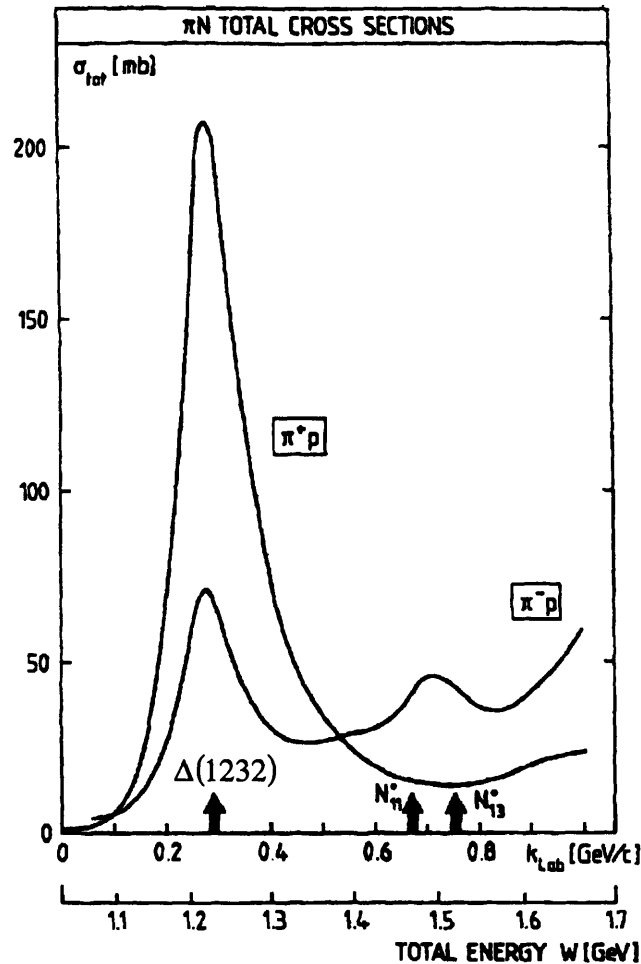


Figure 1.3: Pion-Nucleon reactions between the total energies of 1.1 GeV to 1.3 GeV are dominated by the presence of the  $\Delta(1232)$  Resonance. At higher  $\pi$ -N total energies,  $N^*$  resonances are also shown.

Two features of  $\pi$ -N scattering in the  $\Delta$ -resonance region are of particular interest. First, the ratios of the  $\pi^+$ -N,  $\pi^0$ -N, and  $\pi^-$ -N single-scattering cross sections for inelastic scattering and SCX are related to the isospin properties of the  $\Delta$  ( $T_\Delta = \frac{3}{2}$ ) and

are accurately predicted by simple isospin formalism. Ratios between multiple-scattering cross sections (e.g., the DCX reaction, or inelastic scattering or SCX assuming multiple scattering) may be constructed from the single-scattering values. Secondly, the angular distributions for  $\pi - N$  cross sections reflect the spin of the  $\Delta$  ( $J_\Delta = \frac{3}{2}$ ); they are forward- and backward-peaked, indicating that the pion interacts with the nucleon in a relative p-wave, i.e.,  $L = 1$ , such that the total angular momentum is  $J_{\pi N} = \frac{3}{2}$  (not  $J_{\pi N} = \frac{1}{2}$ ).

### 1.3.1 Pion-Nucleon Scattering Cross Sections

Whether viewed as a particle or a resonance, the  $\Delta$ 's isospin characteristics govern the strength of various  $\pi N$  reaction channels, and a calculation can be made of various transition amplitudes using only isospin formalism. By forming a basis of  $|\pi, N\rangle$  eigenstates and isospin states of the  $\Delta$ ,  $|\mathbf{T}, T_m\rangle$ , the probability of  $\Delta$  formation and decay between specific  $|\pi, N\rangle$  states is given by the square of the corresponding Clebsch-Gordan coefficients associated with the  $T = \frac{3}{2}$  amplitude.

A classic illustration of this procedure is the calculation of the single-scattering (or single-interaction) cross sections for inelastic scattering and SCX on the neutron and proton. Since the pion has isospin  $T_\pi = 1$  and the nucleon  $T_N = \frac{1}{2}$ , the total isospin of the  $\pi - N$  system can be either  $T_{\pi N} = \frac{3}{2}$  or  $\frac{1}{2}$ . Using quantum mechanical bra- and -ket notation, the initial charged pion states  $\langle \pi^+ p |$ ,  $\langle \pi^+ n |$ ,  $\langle \pi^- p |$  and  $\langle \pi^- n |$  can be expanded in isospin states weighted by Clebsch-Gordan coefficients as follows:

$$\langle \pi^+ p | = \left\langle \frac{3}{2}, \frac{3}{2} \right| \quad (1-3)$$

$$\langle \pi^+ n | = \sqrt{\frac{1}{3}} \left\langle \frac{3}{2}, \frac{1}{2} \right| + \sqrt{\frac{2}{3}} \left\langle \frac{1}{2}, \frac{1}{2} \right| \quad (1-4)$$

$$\langle \pi^- p | = \sqrt{\frac{1}{3}} \left\langle \frac{3}{2}, -\frac{1}{2} \right| - \sqrt{\frac{2}{3}} \left\langle \frac{1}{2}, -\frac{1}{2} \right| \quad (1-5)$$

$$\langle \pi^- n | = \left\langle \frac{3}{2}, -\frac{3}{2} \right| \quad (1-6)$$

The final charged pion states are conjugates of the above  $|\pi^- p\rangle$ ,  $|\pi^- n\rangle$ . The uncharged pion states  $|\pi^0 p\rangle$  and  $|\pi^0 n\rangle$ , needed to calculate amplitudes for the SCX reactions, are expanded similarly as follows:

$$|\pi^0 p\rangle = \sqrt{\frac{2}{3}} \left| \frac{3}{2}, \frac{1}{2} \right\rangle - \sqrt{\frac{1}{3}} \left| \frac{1}{2}, \frac{1}{2} \right\rangle \quad (1-7)$$

$$|\pi^0 n\rangle = \sqrt{\frac{2}{3}} \left| \frac{3}{2}, -\frac{1}{2} \right\rangle + \sqrt{\frac{1}{3}} \left| \frac{1}{2}, -\frac{1}{2} \right\rangle \quad (1-8)$$

The amplitudes for the SCX and elastic scattering processes are calculated by forming the following matrix elements formed between  $\pi N$  states. The Hamiltonian of the interaction,  $H_{int}$ , is taken to operate independent of the 3<sup>rd</sup> component of isospin, and amplitudes  $A_{3/2}$  and  $A_{1/2}$  are based only on the total isospin as follows:

$$\langle \pi^+ n | H_{int} | \pi^0 p \rangle = \langle \pi^- p | H_{int} | \pi^0 n \rangle = \sqrt{\frac{2}{9}} A_{3/2} - \sqrt{\frac{2}{9}} A_{1/2} \quad (1-9)$$

$$\langle \pi^+ p | H_{int} | \pi^+ p \rangle = \langle \pi^- n | H_{int} | \pi^- n \rangle = A_{3/2} \quad (1-10)$$

$$\langle \pi^+ n | H_{int} | \pi^+ n \rangle = \langle \pi^- p | H_{int} | \pi^- p \rangle = \sqrt{\frac{1}{9}} A_{3/2} - \sqrt{\frac{4}{9}} A_{1/2} \quad (1-11)$$

Assuming that the transition proceeds through the formation and decay of a  $\Delta$  with total isospin  $T = \frac{3}{2}$ , an additional simplification can be made by assigning  $A_{3/2} = 1$  and  $A_{1/2} = 0$ . The cross sections for these reactions may be associated with the square of the corresponding matrix elements. The ratios between the cross sections for these three reactions are determined to be 9 : 2 : 1 as follows:

$$\begin{aligned} \sigma(\pi^+ p \rightarrow \pi^+ p) : \sigma(\pi^+ n \rightarrow \pi^0 p) : \sigma(\pi^+ n \rightarrow \pi^+ n) \text{ or} \\ \sigma(\pi^- n \rightarrow \pi^- n) : \sigma(\pi^- p \rightarrow \pi^0 n) : \sigma(\pi^- p \rightarrow \pi^- p) \end{aligned} \quad (1-12)$$

$$1 : \frac{2}{9} : \frac{1}{9} \quad (1-13)$$

$$9 : 2 : 1 \quad (1-14)$$

Experimentally, the cross sections involving initial states including a neutron cannot be observed directly as free neutron targets do not exist. Free proton targets do exist, however, and the predictions based on these simple arguments agree well with measurements of  $\pi - p$  cross sections (see figure 1.4). A treatment of this subject can be found in the presentation of isospin in most elementary quantum theory texts.

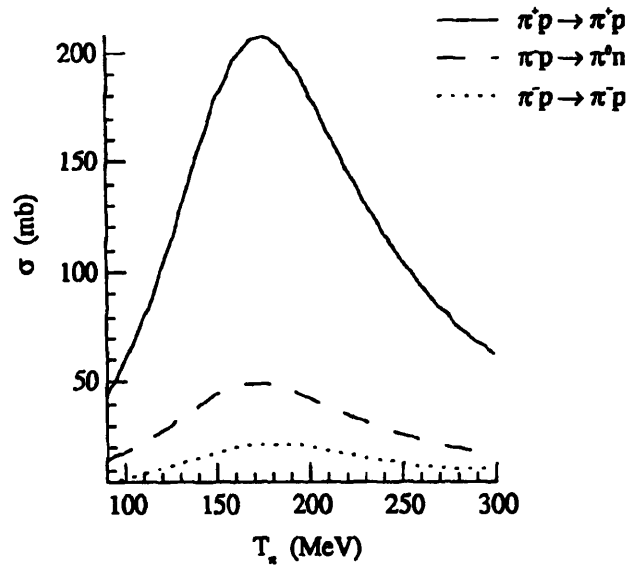


Figure 1.4: The total cross sections for  $\pi^\pm$  elastic scattering and single-charge exchange from the proton follow a 9:2:1 ratio predicted by simple isospin arguments. The curves are from  $\pi - N$  phase shift calculations<sup>9</sup>. These calculations reproduce  $\pi^\pm p$  data quite well. The figure is taken from reference 37.

### 1.3.2 Angular Dependence of Pion-Nucleon Reactions

The angular distribution of  $\pi - N$  reactions, or the differential cross section  $d\sigma/d\Omega$ , can be predicted assuming the reaction proceeds as  $\pi + N \rightarrow \Delta \rightarrow \pi + N$ . The total angular momentum in the process is then equal to the intrinsic spin of the intermediate  $\Delta$ . Since



the pion is spinless and nucleons have spin  $\frac{1}{2}$ , the decay of the  $\Delta$  with  $J = \frac{3}{2}$  leaves the pion and nucleon with one unit of relative orbital momentum. The angular momentum part of the initial and final state wave functions (taking the axis of quantization along the direction of motion so  $m=0$ ) can then be written as:

$$\psi_i\left(\frac{1}{2}, \frac{1}{2}\right) \propto Y_{1,0}(\theta_{\text{cm}})\left|\frac{1}{2}, \frac{1}{2}\right\rangle \quad (1-15)$$

$$\psi_f\left(\frac{3}{2}, \frac{1}{2}\right) \propto \sqrt{\frac{2}{3}}Y_{1,0}(\theta_{\text{cm}})\left|\frac{1}{2}, \frac{1}{2}\right\rangle + \sqrt{\frac{1}{3}}Y_{1,1}(\theta_{\text{cm}})\left|\frac{1}{2}, -\frac{1}{2}\right\rangle \quad (1-16)$$

where the spherical harmonics,  $Y_{l,m}$ , describe the orbital angular momentum, and the  $\left|\frac{1}{2}, \pm\frac{1}{2}\right\rangle$  are the spin states. There are two components to the wave function since the spin of the nucleon may be flipped. The differential cross section is proportional to the square of the matrix element:

$$\begin{aligned} \frac{d\sigma}{d\Omega}(\theta_{\text{cm}}) &\propto |\langle \psi_f | H | \psi_i \rangle|^2 \\ &\propto \left| \left\langle \frac{1}{2}, \frac{1}{2} \cdot \sqrt{\frac{3}{2\pi}} \cos\theta_{\text{cm}} \left| \frac{1}{2}, \frac{1}{2} \right\rangle - \left\langle \frac{1}{2}, -\frac{1}{2} \cdot \sqrt{\frac{3}{8\pi}} \sin\theta_{\text{cm}} e^{i\phi} \left| \frac{1}{2}, -\frac{1}{2} \right\rangle \right|^2 \right. \\ &\propto \frac{3}{2} \cos^2\theta_{\text{cm}} + \frac{3}{8} (1 - \cos^2\theta_{\text{cm}}) \\ &\propto 1 + 3 \cos^2\theta_{\text{cm}} \end{aligned} \quad (1-17)$$

At the peak of the resonance, the  $\pi - N$  differential cross section exhibits this characteristic angular dependence that is peaked at forward- and backward angles. The angular distribution for  $\pi^- p \rightarrow \pi^0 n$  scattering in the center-of-mass frame at  $T_\pi = 160$  MeV, the incident beam energy of this measurement, is shown in figure 1.5. The distribution does not exactly follow equation 1-17 and is not symmetric about  $\theta_{\text{cm}} = 90^\circ$  since the energy is slightly lower than at the peak of the  $\Delta$ -resonance. The peaking at forward- and backward angles, however, is still very much evident.

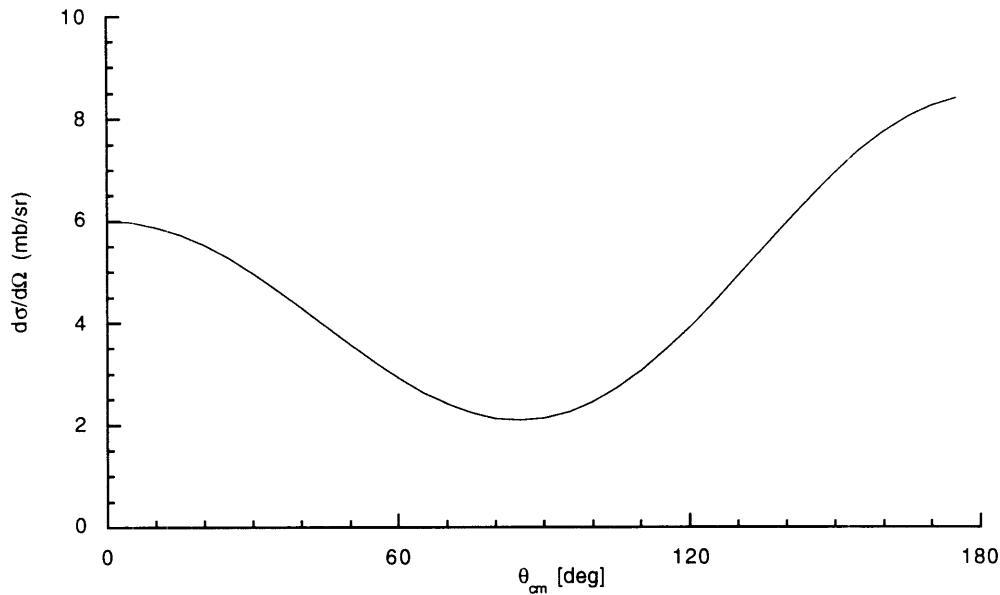


Figure 1.5: The differential cross section for the reaction  $\pi^- p \rightarrow \pi^0 n$  at an incident beam energy  $T_{\pi^-} = 160$  MeV. The curve is based on a phase shift parameterization of the data.<sup>10</sup>

## 1.4 Pion – Nucleus Inelastic Scattering

Understanding how the  $\pi N$  interaction is changed in the presence of other nucleons is one of the fundamental questions in pion-nucleus scattering. Compared with scattering from a single free nucleon, pion-induced reactions in nuclei include many additional inelastic scattering reactions in which the energy is shared among several bodies. For instance, the absorption of a pion by a single free nucleon is energetically forbidden, as is the time-reversal equivalent for this process, emission of a pion by a single free nucleon. Absorption on two or more nucleons is possible, however, as is absorption on a single nucleon in a nucleus. In the latter case, the remaining nucleons share the momentum and total energy (kinetic plus rest mass energy) of the absorbed pion. At energies where pion-induced pion production is energetically impossible, DCX also cannot occur on a single nucleon, as two units of charge cannot be exchanged with one nucleon.

---

The role of the  $\Delta$  in these reactions remains important since the pion does not necessarily interact with the nucleus as a whole and may couple to few- or single-nucleon parts of the nuclear wave function. Quasifree or quasielastic scattering, where the pion scatters from individual, bound nucleons, dominates  $\pi - A$  cross sections. In the  $\Delta$ -resonance region, it is important to note that the  $\pi^+$  is nine times more likely to scatter elastically from the proton than from the neutron. The  $\pi^+$  can thus be thought of as a probe of the proton distributions in nuclei. Similarly, the  $\pi^-$  is nine times more likely to scatter from the neutron than from the proton and is therefore sensitive to neutron distributions in nuclei. As there exist no free neutron targets, scattering from this nucleon must be observed in the presence of nuclear protons. Quasifree  $\pi^-$ -scattering reactions are well-suited for this task.

Pion inelastic scattering reactions have been extensively studied in three modern experiments on  $^4\text{He}$ <sup>11,12,13</sup>. As seen in figure 1.6, the spectra of outgoing pion energies from the  $^4\text{He}(\pi^+, \pi^+)X$  reaction show a sharp elastic peak from scattering coherently off the target nuclei and a prominent, broad peak near the kinematic energy characteristic of two-body pion scattering from a free nucleon which is denoted by arrows at each scattering angle. The peak is at slightly lower energies compared with free  $\pi N$  kinematics, and this is attributed to the binding energy of the nucleons in the nucleus. The width of this peak is due to the Fermi motion of the nucleon within the nuclear potential. The above observations all suggest that quasifree scattering dominates.

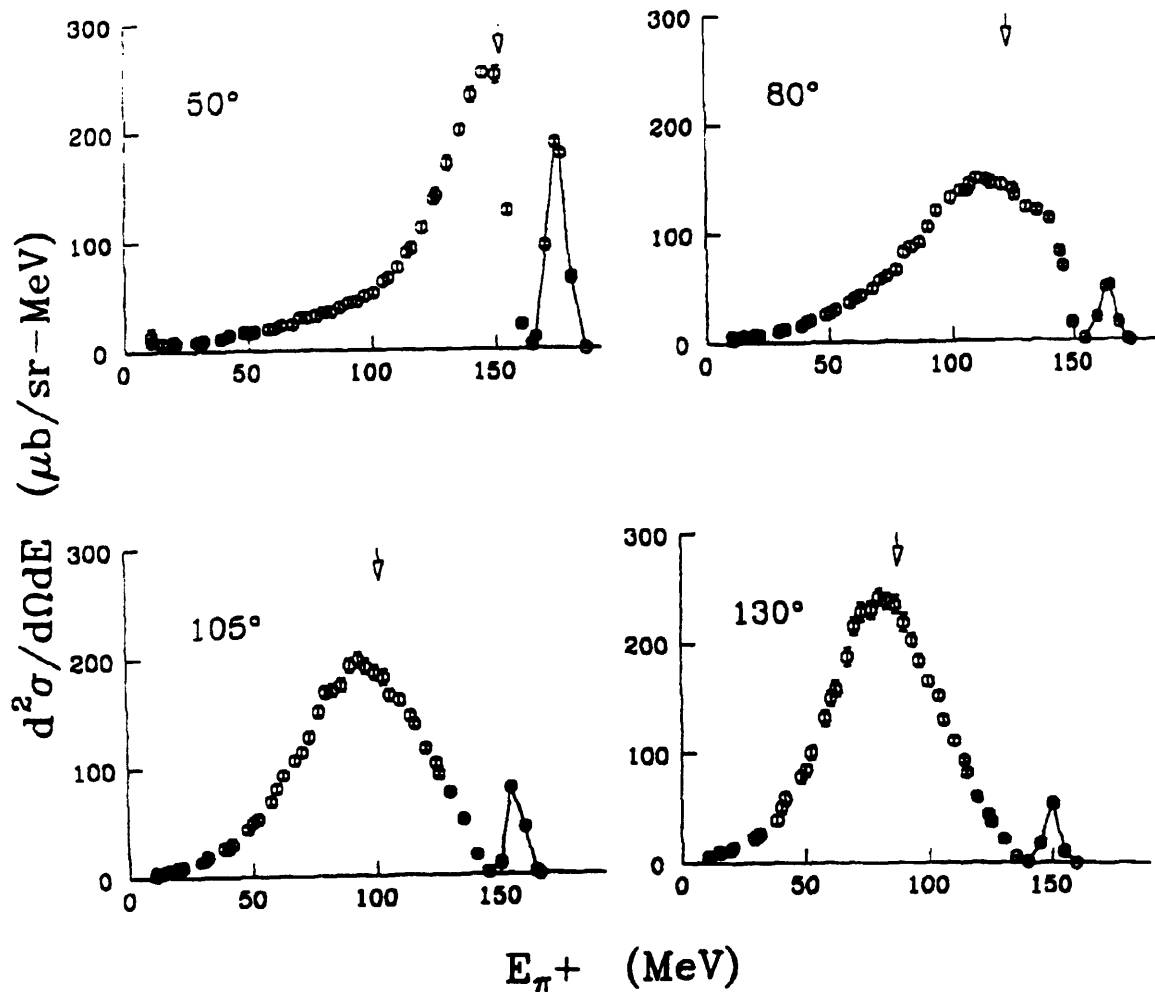


Figure 1.6: Doubly differential cross sections for the reaction  ${}^4\text{He}(\pi^+, \pi^+)X$  at an incident energy of 180 MeV. The sharp peak at high outgoing pion energy is the result of elastic scattering off the nucleus (the elastic cross sections have been multiplied by 0.2), and the lower energy quasielastic peak is caused from scattering off individual, bound nucleons. The arrow indicates the energy corresponding to free  $\pi N$  kinematics. The figure is from reference 13.

These spectra are qualitatively similar to energy spectra from inclusive quasielastic electron scattering from nuclei where a quasifree peak whose width is broadened by Fermi motion is also evident. The similarities between pion- and electron-induced reactions may seem unexpected given the difference in interaction strengths between electromagnetic interactions and strong interactions. Despite the common conclusion of single-scattering,

however, the explanations for both processes are quite different.

In electron scattering, single scattering is a result of the small electromagnetic coupling constant  $\alpha_{EM} = \frac{1}{137}$  which makes additional scattering orders of magnitude less probable than single scattering. On the other hand, inelastic scattering pion reactions do not show effects of multiple scattering because multiple-scattering processes are truncated by pion absorption. The pion's chance for survival decreases with each scattering due to the high probability of being absorbed at each interaction.

Any indication of multiple scattering from the pion inelastic scattering spectra is expected to be featureless and lower in energy than that of the quasifree peak. With each additional scattering, the pion decreases in energy from that of the quasifree peak, a single scattering process. The contribution of double-scattering to the doubly-differential cross section in  ${}^4\text{He}$  has been estimated by Baumgartner *et al.*<sup>11</sup> by utilizing data<sup>14</sup> from the DCX reaction  ${}^4\text{He}(\pi^+, \pi^-)X$ . This analysis concluded that because DCX is strongly energy dependent, the contribution of double nucleon knock-out to the cross section is negligible at energies below 270 MeV, a result not unexpected in a few-body system such as  ${}^4\text{He}$ . In heavier nuclei<sup>12</sup> such as  ${}^{12}\text{C}$ ,  ${}^{16}\text{O}$ ,  ${}^{58}\text{Ni}$ , and  ${}^{208}\text{Pb}$ , the contributions from multiple scattering at intermediate energies, as indicated by a substantial low-energy pion yield, are more significant. Using the DCX cross section  ${}^{16}\text{O}(\pi^+, \pi^-)X$  as a guide, the multiple-scattering contribution in the inelastic scattering  ${}^{16}\text{O}(\pi^+, \pi^+)X$  reaction was found<sup>15,16</sup> to increase from about 8% at  $T_{\pi^+} = 120$  MeV to about 30% at  $T_{\pi^+} = 240$  MeV.

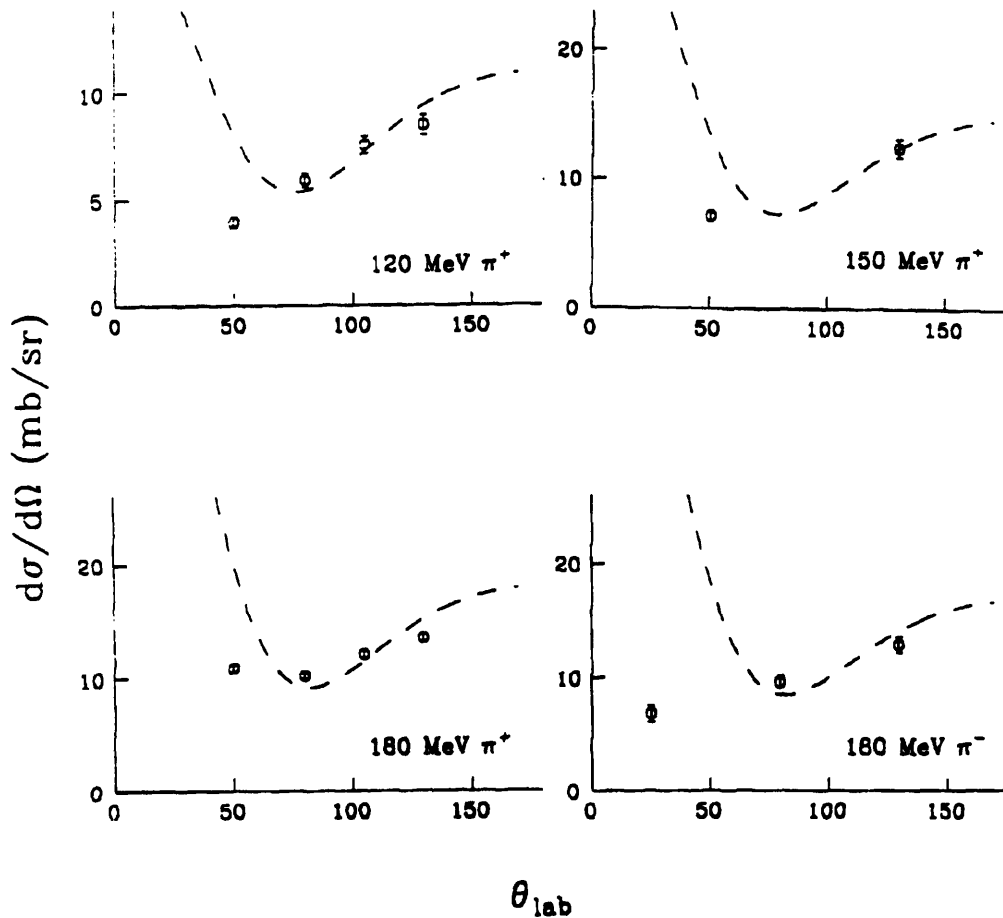


Figure 1.7: The differential cross sections for the reactions  ${}^4\text{He}(\pi^+, \pi^+)X$  and  ${}^4\text{He}(\pi^-, \pi^-)X$  as a function of laboratory scattering angle. The dashed lines indicate the angular distributions of the average free  $\pi$ -N cross section. The reaction in  ${}^4\text{He}$  approximately follows that for the free nucleon except at forward angles which is subject to a suppression due to Pauli blocking. The figure is from reference 13.

The angular dependence of the differential cross sections  $d\sigma/d\Omega_{\text{lab}}$  for inelastic scattering in nuclei follows that for scattering from a free nucleon at backward angles, as seen in  ${}^4\text{He}$  in figure 1.7. This supports the idea that quasifree scattering is predominantly single scattering from an individual, bound nucleon. At forward angles, however, the cross section is suppressed. This is due to an effect known as Pauli Blocking<sup>17</sup>, a nuclear physics application of the Pauli Exclusion Principle which forbids two spin  $\frac{1}{2}$  fermions to have exactly the same quantum numbers. For forward angle scattering, the energy and

---

momentum transferred from the incident particle to the nucleus is small, and the initial kinetic energy is retained in large part by the projectile. The low-energy nucleon states for ground-state nuclei are all occupied, however, and are not available for a struck nucleon to inhabit. The result is to suppress the quasielastic cross section at forward angles.

## 1.5 Pion Absorption

To be complete, any study of pion scattering mechanisms in nuclei must include mention of pion absorption, those processes leading to a final state with no pion. The question of whether inelastic scattering, SCX, and DCX reactions are dominated by single- (for inelastic scattering and SCX), double-, or higher-order-scattering is related to the strength of the competing absorptive process. As seen above in quasifree inelastic scattering experiments, multiple-scattering sequences yielding an emitted pion are unlikely and the reaction is dominated by single-scattering.

The study of pion absorption in nuclei also lends well to a study of multi-nucleon reaction mechanisms. Since absorption cannot occur on a free nucleon, the deuteron is then the lightest nucleus on which a pion can be absorbed. Absorption is not limited, however, to two-nucleon processes. Multi-nucleon absorption, involving all nucleons in a nucleus or subsets of nucleons, can also occur, and it is useful to determine how many nucleons are “spectators” and retain their Fermi momentum. One of the fundamental questions confronting the study of pion absorption is “How many nucleons are involved in absorption?”

In  ${}^4\text{He}$ , the two-nucleon absorption component, typically involving a proton-neutron pair, is believed to be a large component of the total absorption cross section in the region of the  $\Delta$ -resonance. A recent study of  $\pi^+$  absorption in  ${}^4\text{He}$  at  $T_{\pi^+}=114$  and  $162$  MeV<sup>18</sup> has attributed, however, only 50% of the total absorption cross section to two nucleon

processes. A quasi-deuteron absorption model<sup>19</sup> has been quite successful in describing many aspects of the experimental data though the data (in comparison with the model) have also indicated existence of additional multi-nucleon reaction channels besides the two-nucleon component.

Extensive studies of two- and three-body pion absorption in  ${}^3\text{He}$ <sup>20,21,22</sup> also indicated the existence of multi-nucleon absorption modes, though these measurements suffered from limited angular coverage or resolution of the detectors. With the recent construction of large acceptance ( $4\pi$  solid angle) detectors, a new generation of experiments is underway to study pion absorption on  ${}^{3,4}\text{He}$ <sup>23</sup>. The comparison between the two nuclei is expected to help isolate the effects of the additional nucleon. Recent analysis<sup>24</sup> of data on  ${}^3\text{He}$  indicates that 22%, 29%, and 30% of the total absorption cross section are attributable to three-nucleon processes at 118, 162, and 239 MeV incident pion energy, respectively. Reviews of the earlier work on pion absorption have been written by H. Weyer<sup>25</sup> and D. Ashery<sup>26</sup>.

## 1.6 Pion Double-Charge-Exchange in Nuclei

Pion charge exchange reactions complement studies of pion inelastic scattering and absorption in nuclei because they comprise the remaining piece of the pion-nucleus total cross section. Given the requirement that at least two like nucleons be involved, pion double charge exchange (DCX) reactions are well suited for studying multiple-scattering effects in pion-reactions. The experimental signature for DCX is the detection of a pion of charge opposite to that of the incident charged pion.

Recent measurements of DCX in  ${}^3\text{He}$ <sup>27,28</sup> and  ${}^4\text{He}$ <sup>29</sup> in the  $\Delta$ -resonance region have revealed a striking “double-humped” shape in the doubly differential cross section at forward angles (see figure 1.8). This has been explained to be the result of two sequential SCX reactions. The higher energy peak is the product of two forward angle SCX scatterings,



which result in little energy loss. The lower energy peak is the product of two backward angle SCX scatterings, resulting in forward scattering by a pion with substantial energy loss. Both these processes are favored over two intermediate angle scatterings, which would lead to a pion at forward angles with an intermediate energy loss, because quasifree SCX is forward- and backward peaked in the  $\Delta$ -resonance region (section 1.3.2).

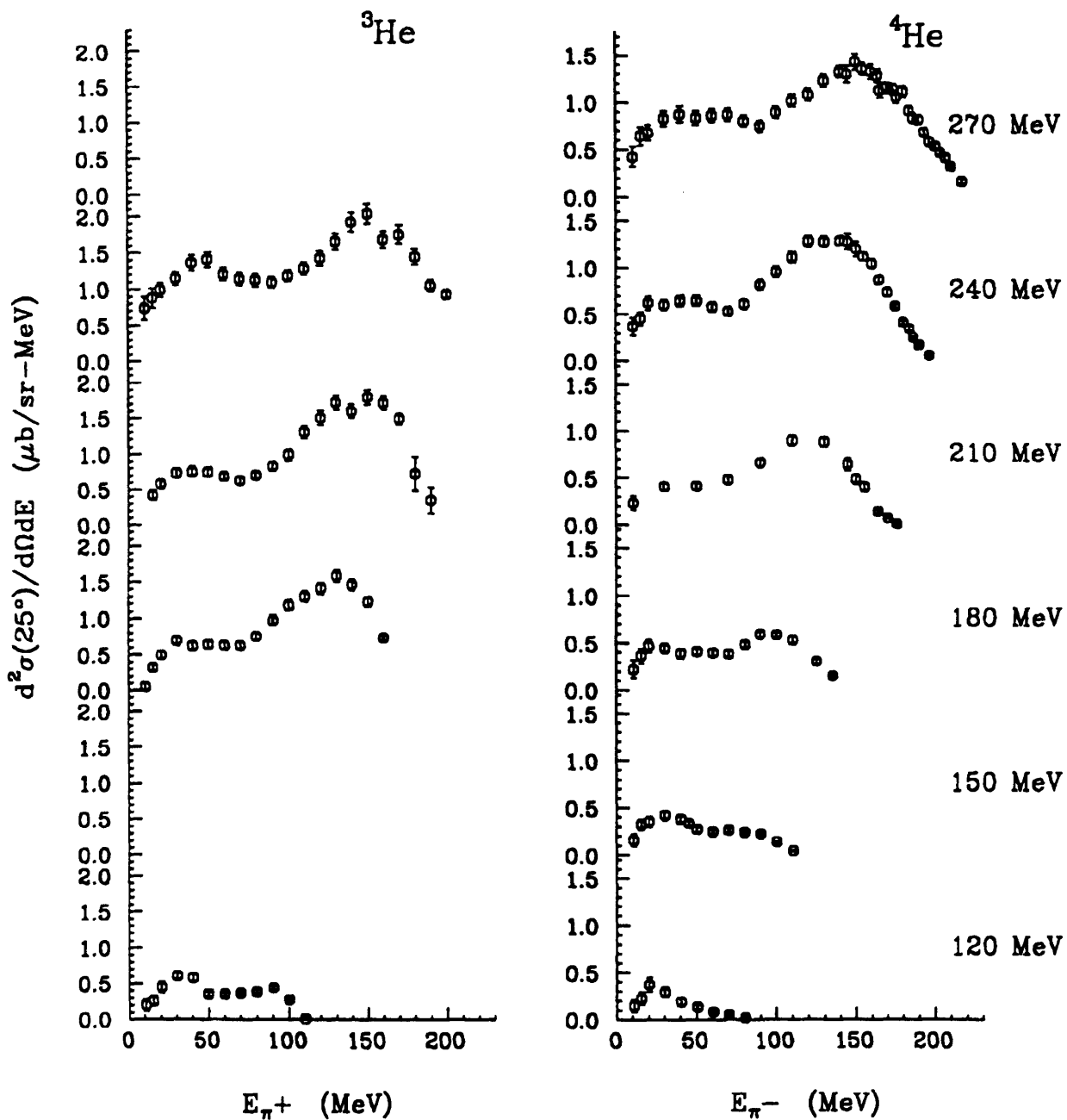


Figure 1.8: The doubly differential cross sections for  ${}^3\text{He}(\pi^-, \pi^+)X$  (left) and for  ${}^4\text{He}(\pi^+, \pi^-)X$  (right) at  $25^\circ$ . The data are plotted for the incident beam energies indicated on the right. The figure is from reference 28.

The simple s-state structure of these nuclei has facilitated calculations of the DCX reaction in  ${}^4\text{He}$  by E. Kinney<sup>30</sup> based on two sequential quasifree SCX reactions (figure 1.9).

While the calculations are unable to reproduce exactly the absolute magnitudes of the doubly-differential cross sections, presumably due to their use of plane wave impulse approximation (PWIA), the qualitative shapes of the spectra at forward angles are well described. This is an indication that two sequential SCX reactions comprise the dominant mechanism. Measurements of the SCX reaction in  ${}^4\text{He}$  should help refine these calculations, provided that the data span wide ranges of reaction angles, incident, and outgoing pion energies, since inclusive DCX must conjoin the two SCX reactions by integrating over all these variables.

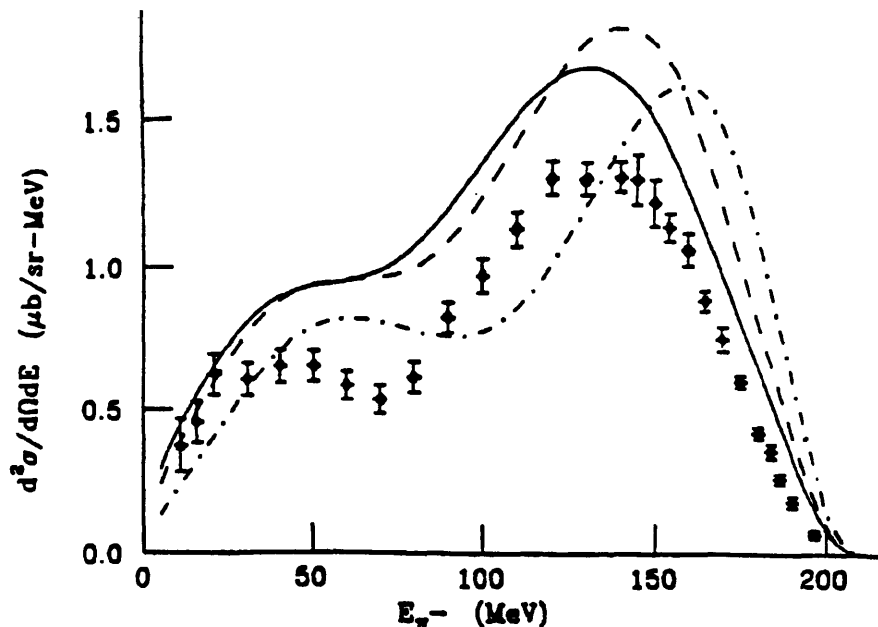


Figure 1.9: The calculations by E. Kinney reproduce the shape of the doubly differential cross section for the  ${}^4\text{He}(\pi^+, \pi^-)X$  reaction at 240 MeV incident pion energy and  $25^\circ$  laboratory scattering angle. The different curves correspond to different values of the average nuclear potential. The figure is from reference 13.

It should be pointed out that the shape of the forward angle DCX spectra at a common incident beam energy changes dramatically for increasing atomic number (figure 1.10). The double-humped feature is seen to a lesser extent in p-shell nuclei<sup>30</sup> such as  ${}^6,7\text{Li}$ , or  ${}^9\text{Be}$ . For larger nuclei<sup>16</sup> such as  ${}^{16}\text{O}$  and  ${}^{40}\text{Ca}$ , this feature disappears altogether as the spectra resemble that of four-body phase space with the energy shared among the outgoing

pion, the two knocked out nucleons, and the recoiling  $A - 2$  nucleus (figure 1.11).

There are several effects which are believed to account for the disappearance of the high-energy peak in DCX spectra from these larger nuclei. First, Pauli blocking of forward angle scattering is more influential in larger nuclei as the Fermi surface is higher due to more low-energy states being occupied by the additional nucleons. The small amounts of energy transferred to the two struck nucleons during sequential forward angle scatterings must be greater than this higher Fermi surface for the reaction to occur, and the cross section is thereby suppressed. Also, the probability for multiple scattering increases with the number of nucleons present, and such processes shift the energy of the outgoing pions to lower energies. Both mechanisms are present in SCX, as presented in the next section, and added understanding of them in a light nucleus such as  ${}^4\text{He}$  may peripherally contribute to an understanding of DCX in heavier nuclei.

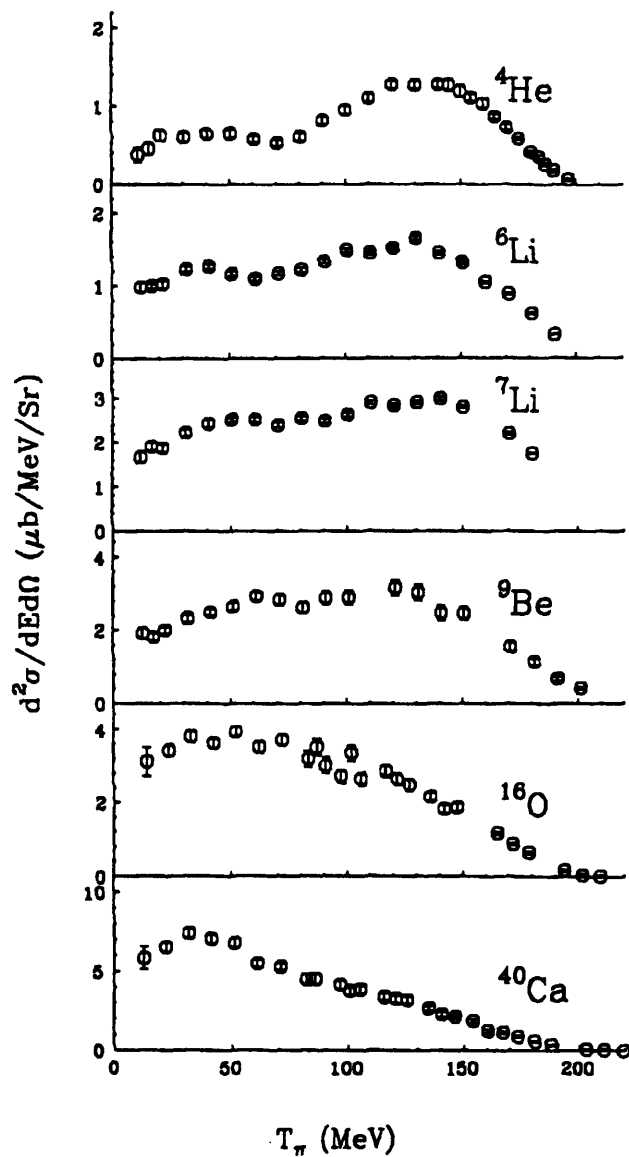


Figure 1.10: The doubly differential cross sections for  $(\pi^+, \pi^-)$  DCX on several nuclei at 240 MeV and a scattering angle of  $25^\circ$ . The double-humped shape in  ${}^4\text{He}$  and light nuclei gradually disappears in heavier nuclei as the higher energy peak becomes less prominent. The figure is from reference 28.

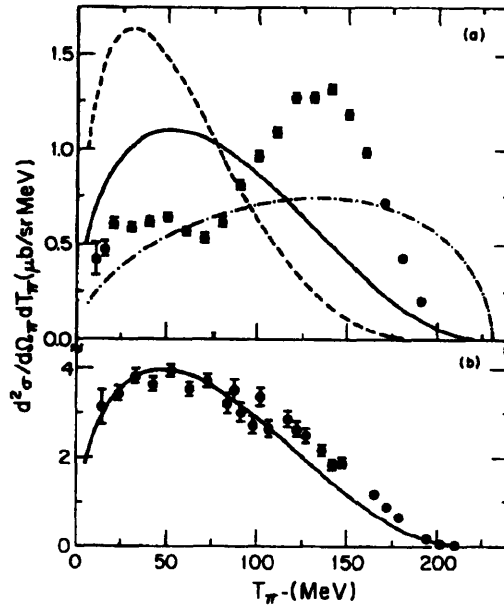


Figure 1.11: The doubly differential cross sections for the reactions (a)  ${}^4\text{He}(\pi^+, \pi^-)4p$  and (b)  ${}^{16}\text{O}(\pi^+, \pi^-)X$  at incident energy 240 MeV and laboratory angle  $25^\circ$ . The dashed and dot-dashed curves in (a) correspond to the distribution of events in five-body and three-body phase space, respectively, while the solid curves in (a) and (b) correspond to four-body phase space. The four-body distribution for  ${}^{16}\text{O}$  has been normalized so that the total volume in phase space is equal to the total DCX cross section. The figure is from reference 29.

## 1.7 Pion Single-Charge-Exchange in Nuclei

Pion single-charge-exchange (SCX) reactions are well suited for studying properties of the nuclear medium not accessible with charged pion scattering. Like inelastic scattering, SCX is dominated by quasielastic scattering from a single nucleon, but multiple-scattering effects are expected to be more prominent because SCX is coupled weakly to the two-nucleon absorption channel. A SCX reaction on a  $T=0$  nucleon pair must lead to a  $T=1$  pair (figure 1.12). The intermediate  $T=1$   ${}^5S_2$   $\Delta N$  state, which is the predominant absorption channel, is forbidden by simple angular momentum, parity, and isospin conservation (the complete argument is presented in Appendix A). This leads to an enhancement of NN and  $\Delta N$  channels and multiple-scattering processes whose effects are diminished in inelastic scattering and DCX reactions due to the strong absorption channel.

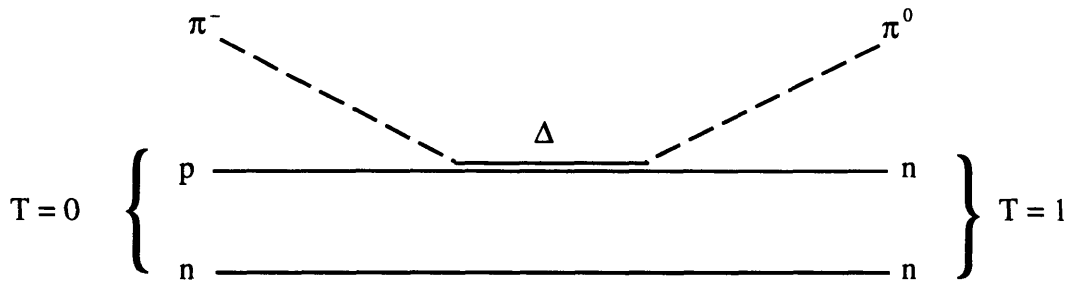


Figure 1.12: Single charge exchange on a  $T=0$  nucleon pair must lead to a  $T=1$  pair. Here the reaction proceeds through the formation and decay of a  $\Delta$ .

In the  $\Delta$ -resonance region, measurements of the inclusive SCX reaction have been performed by Ashery *et al.*<sup>31</sup> on a range of nuclei from  $^{12}\text{C}$  to  $^{208}\text{Pb}$  at an incident beam energy of 160 MeV. The doubly differential cross sections  $d^2\sigma/dE_{\pi^0}d\Omega_{\text{lab}}$  (shown in figure 1.13) display a broad peak similar in energy and shape to the quasifree peak in inelastic scattering reactions.

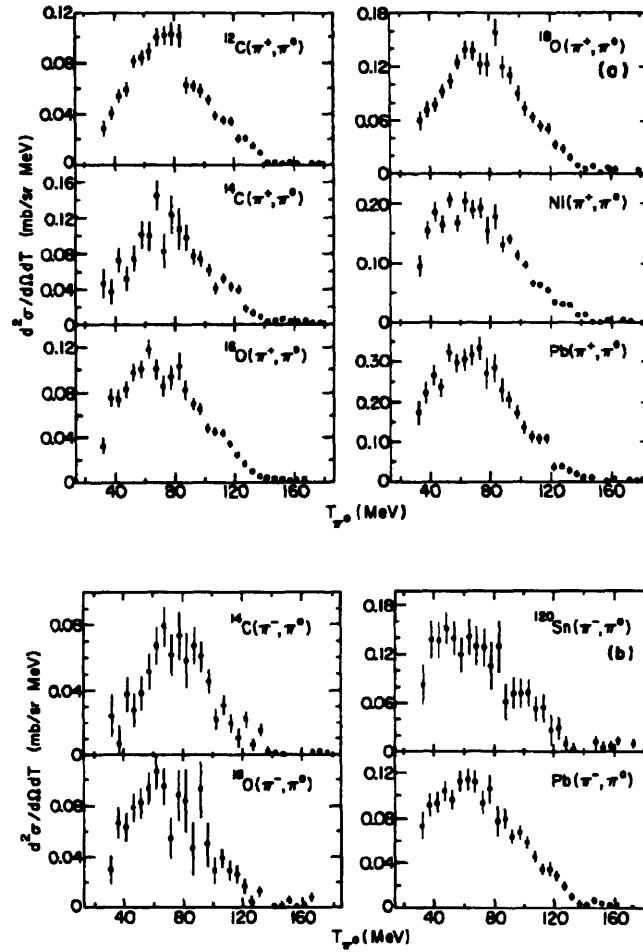


Figure 1.13: The shapes of the doubly differential cross sections for the inclusive SCX reaction on a range of nuclei are characteristic of quasifree scattering from nucleons. All the data were taken with an incident beam energy of 160 MeV. The figure is from reference 31

A comparison<sup>32</sup> of the cross section in the quasifree peak region from  $^{16}\text{O}(\pi^+, \pi^0)\text{X}$  with that in  $^{16}\text{O}(\pi^+, \pi^+)\text{X}$  at the same incident beam energy  $T_{\pi^+} = 163$  MeV shows an excess in the low energy part of the spectrum for the SCX reaction compared with inelastic scattering, an indication of additional multiple-scattering effects (figure 1.14). Furthermore, the peak is shifted to lower energies for the charge-exchange reaction. The two curves shown are theoretical calculations of the inelastic scattering cross section<sup>33</sup> whose differences reflect different treatments of  $\Delta$  propagation and interaction and of the distorted waves. The calculation based on the  $\Delta$ -hole model, which treats the  $\Delta$  as an explicit



---

degree of freedom that is allowed to propagate and interact within the nuclear medium, predicts correctly the doubly-differential cross sections over a wide range of angles and energies. The calculation based on the closure approximation, which is a standard first-order theory, is in unexpectedly good agreement with the SCX data given that the approximation does not agree in general with the elastic scattering data and total cross sections. A detailed understanding of these SCX energy spectra still awaits microscopic theoretical treatment, a difficult calculation in large nuclei. The same task in  ${}^4\text{He}$  may be manageable.

The singly differential cross sections  $d\sigma/d\Omega_{\text{lab}}$  from the Ashery data are shown in figure 1.15 with curves representing the  $p(\pi^-, \pi^0)n$  angular distributions normalized to the data at backward angles. The data agree well with the distributions from SCX on the free proton at backward angles, in support of the quasifree description of the process. The normalization factors, known as  $N_{\text{eff}}$ , are a measure of the effective number of nucleons involved in the reaction. The values of  $N_{\text{eff}}$  from SCX have been found<sup>31</sup> to be similar to those from inelastic scattering. This supports the description of both reactions being dominated by quasifree scattering.

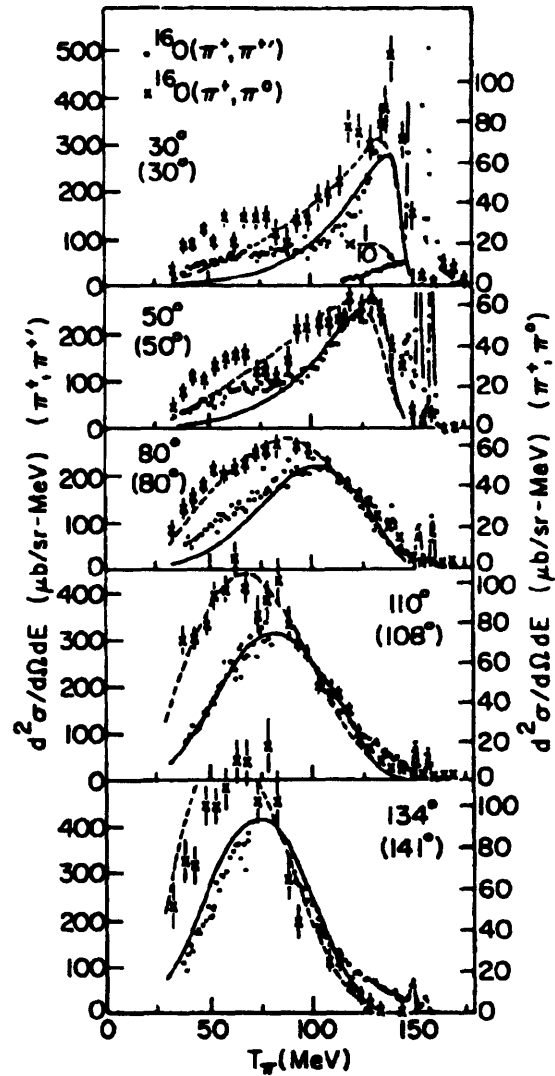


Figure 1.14: The doubly differential cross sections for the  $^{16}\text{O}(\pi^+, \pi^0)\text{X}$  and  $^{16}\text{O}(\pi^+, \pi^+)\text{X}$  reactions at  $T_{\pi^+} = 163$  MeV. The ratio of the scales is that of the corresponding pion-nucleon reactions. Angles in parenthesis are for the  $(\pi^+, \pi^0)$  reaction. The two curves are theoretical calculations of the inelastic scattering process using the  $\Delta$ -hole model (solid line) and closure approximation (dashed line). The figure is from reference 32.

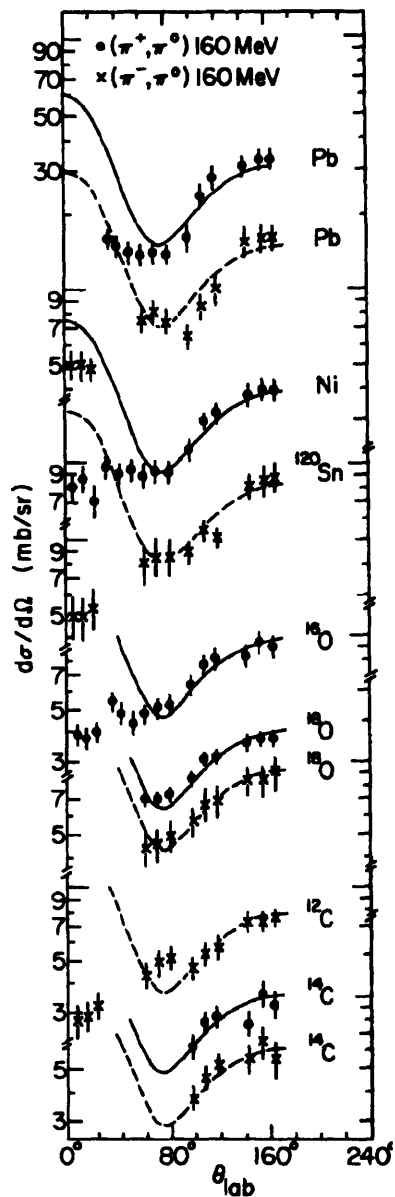


Figure 1.15: The singly differential cross sections for the inclusive SCX reaction on a range of nuclei. The curves are the angular distributions of the  $p(\pi^-, \pi^0)n$  reaction fit to the data at backward angles. The figure is from reference 31

As in the inelastic scattering reaction, Pauli blocking is believed to occur at forward angles, where the data and curve do not agree. A measure of Pauli blocking can be estimated<sup>31</sup> by taking the ratio between the measured cross section and that from the free proton, scaled by  $N_{\text{eff}}$  as follows:

$$B = \frac{\sigma_{\text{scx}}}{N_{\text{eff}} \cdot \sigma(\pi^- p \rightarrow \pi^0 n)} \quad (1-18)$$

For the entire range of nuclei, the value of B was found to be nearly constant<sup>31</sup>, about 0.83, similar to the  $B \sim 0.6 - 0.8$  values observed<sup>34</sup> for charged pion scattering in nuclei ranging from  ${}^7\text{Li}$  to  ${}^{209}\text{Bi}$  at 165 MeV. The inelastic scattering measurements were made at a range of energies from 85 MeV to 315 MeV incident energy, and B was observed to be independent of A and energy for energies above 165 MeV, but not below.

Previous measurements have also been performed by Bowles *et al.*<sup>35</sup> of the inclusive  $(\pi^\pm, \pi^0)$  reaction in nuclei ranging from  ${}^9\text{Be}$  to  ${}^{208}\text{Pb}$  at two beam energies below the  $\Delta$ -resonance, 50 and 100 MeV. The angular distributions and  $\pi^0$  energy spectra for scattering beyond  $60^\circ$  also suggest effects characteristic of quasifree scattering.

Two modern measurements of the SCX reaction exist on a nucleus lighter than  ${}^9\text{Be}$ . Both are measurements over a limited range of outgoing  $\pi^0$  energies and angles of SCX on  ${}^3\text{He}$ . Cooper *et al.*<sup>36</sup> measured the  ${}^3\text{He}(\pi^-, \pi^0)$  reaction at the incident pion energy of  $T_{\pi^-} = 200$  MeV only at forward angles in the laboratory,  $\theta = 0^\circ - 90^\circ$ . Unlike the case of the  ${}^4\text{He}$  nucleus,  $(\pi^-, \pi^0)$  on  ${}^3\text{He}$  may result in an intact recoil nucleus, and the reaction to the tritium ( ${}^3\text{H}$ ) ground state was measured as well. The measurements to the continuum state show effects of quasifree scattering though there is substantial uncertainty in the low-energy parts of the doubly-differential cross sections. The angular distribution of the data (figure 1.16) show effects of Pauli blocking, as expected.

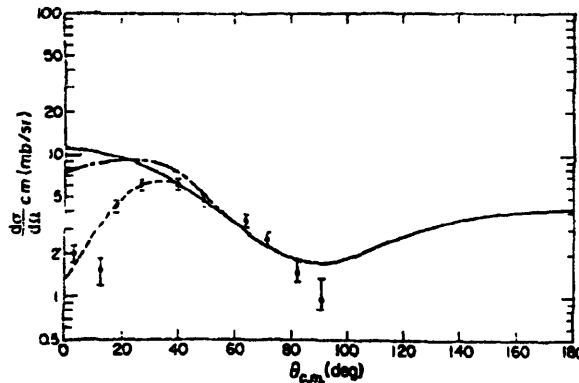


Figure 1.16: The angular distribution of the  ${}^3\text{He}(\pi^-, \pi^0)$  reaction at 200 MeV. The cross section was not measured at backward angles. The solid curve is 1.03 times the free proton SCX cross section. The dashed curve is a smooth curve through the data, and the dash-dot curve has the  ${}^3\text{He}(\pi^-, \pi^0){}^3\text{H}$  cross section added to the dashed curve. The deviation of the data from the solid curve at forward angles is due to the effects of Pauli blocking. The figure is from reference 36.

The other measurement<sup>37</sup> of SCX on this nucleus was of the  ${}^3\text{He}(\pi^\pm, \pi^0)$  reactions at the incident pion energy of  $T_\pi = 245$  MeV only at laboratory angles of  $62^\circ$  and  $128^\circ$ . The doubly-differential cross section reveals the process to be quasi-free. While there is slight indication of multiple scattering, the cross sections were not measured to low enough energy (the data end at 65 MeV or 100 MeV depending on the scattering angle) to be conclusive. The limited angular range of the measurement makes any estimation of the effects of Pauli blocking impossible.

## 1.8 Scientific Motivation for this Measurement

The preceding sections of this chapter, in reviewing pion scattering physics at intermediate energies, present general motivations for this measurement of pion single charge exchange in  ${}^4\text{He}$  in the  $\Delta$ -resonance region. The specific motivations for this measurement come from two comparisons. The first is between SCX and inelastic scattering in  ${}^4\text{He}$ . As stated in section 1.7 (and argued in appendix A), SCX may show additional signs of multiple scattering compared to inelastic scattering given that the reaction cannot proceed

through the intermediate  $T=1$   ${}^5S_2$   $\Delta N$  state, the predominant absorption channel. This is observed in the form of an excess at the low energy part of the SCX spectrum in heavier nuclei<sup>32</sup> such as  ${}^{16}\text{O}$ , and there is a similar excess<sup>37</sup>, if inconclusive, in  ${}^3\text{He}$ . In addition, the comparison between SCX and inelastic scattering in  ${}^{16}\text{O}$  reveals a shift to lower energies for the quasifree peak in the charge-exchange reaction. A comparison of the low energy tails and quasifree peaks in  ${}^4\text{He}$  SCX and inelastic scattering will help study the  $A$ -dependences of these effects.

The second specific motivation for this measurement is the comparison between SCX in  ${}^4\text{He}$  with SCX in heavier nuclei. Ashery *et al.*<sup>31</sup> have measured inclusive SCX reactions on a range of nuclei from  ${}^{12}\text{C}$  to  ${}^{208}\text{Pb}$  at an incident beam energy of 160 MeV. The incident beam energy of the measurement presented in this work is also 160 MeV and thus permits a direct comparison of the reaction in  ${}^4\text{He}$ . Given that quasifree scattering plays such an important role in pion-nucleus reactions at intermediate energies, this measurement should help address the underlying question of how the  $\pi N$  interaction is modified in the nuclear medium.

Data on inelastic scattering and DCX in  ${}^4\text{He}$  exist, and SCX is needed to develop a consistent picture of pion-nucleus interactions in this system. Had this measurement covered a wider range in incident beam energies, as the experiment had proposed, a calculation of DCX based on two, sequential SCX reactions could have employed data from the single-step process. This remains as motivation for a future measurement.

---

## Chapter 2: Experimental Setup and Procedures

All particle physics experiments share several common elements, regardless of the energy scale, physical size, or scientific motivations involved. The first is that there must be an incident beam of some sort, produced by an accelerator. The second is that there must exist a target with which the incident beam is intended to interact. Finally, there must be a detector whose measurements of the energies, angles, etc. of scattered particles are designed to lead to new understandings of the physical processes being studied. As with our experiment, these detectors are connected with data acquisition electronics and a computer whose software package is designed to process the data. This chapter presents a description of these physical elements as well as the procedures used during the experiment which produced the data presented in this thesis.

### 2.1 Incident Beam

The data presented in this thesis come from an experiment conducted at the Clinton P. Anderson Meson Physics Facility (LAMPF) during the summer of 1990 (LAMPF experiment number 1177, “Inclusive Pion Single Charge Exchange in  $^3\text{He}$  and  $^4\text{He}$ ”). The primary beam at this facility<sup>38</sup> is a proton beam whose average intensity is  $\sim 0.5 - 1$  mA and maximum energy is 800 MeV. During this experiment, the duty-factor of the beam was 6.3%. The protons are accelerated in a half-mile long linear accelerator, or linac. Secondary pion beams are produced from the interaction of these protons with two graphite pion production targets which have been placed in the path of the primary beam. These pions can have kinetic energies up to the primary beam energy less the pion rest mass energy. At LAMPF, the meson physics research is conducted in experimental halls adjacent to the production targets, labelled A-1 and A-2 in figure 2.1, which comprise Experimental Area A at LAMPF.

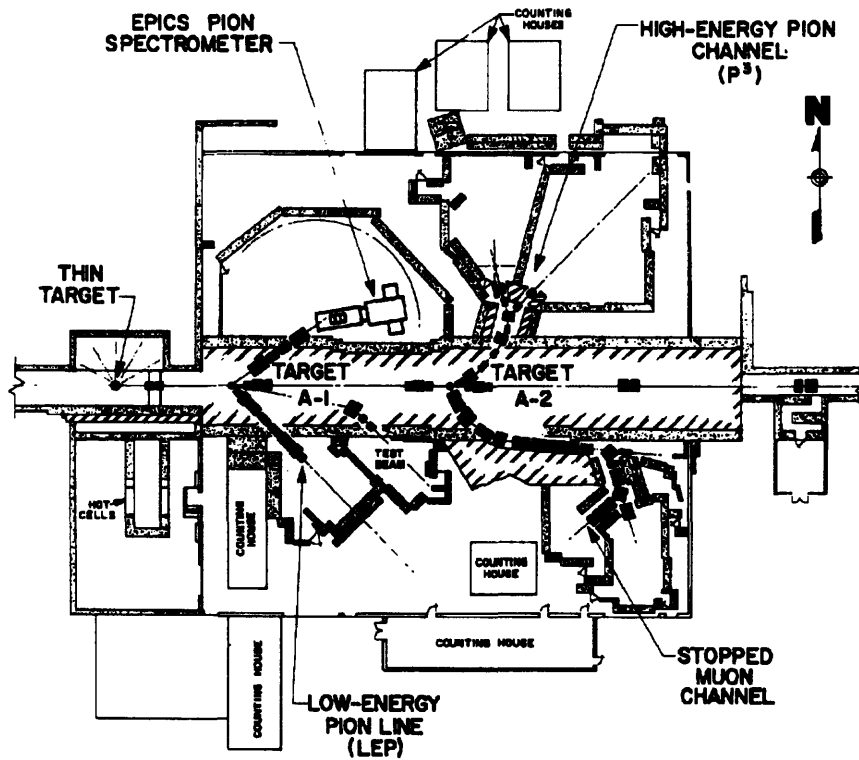


Figure 2.1: Experimental Area A at LAMPF. The two graphite pion production targets are labelled A-1 and A-2. Our experiment was performed in the East cave of the  $P^3$  channel. The drawing is from reference 38.

Our experiment was performed in the East cave of the Pion and Particle Physics ( $P^3$ ) channel (figure 2.2). It is the responsibility of the experimenter to control a series of beam transport elements, between the production target and the experimental cave, which determine the characteristics of the secondary beam. These elements include bending magnets, focussing magnets, and collimating slits, as shown in figure 2.3. Variable amounts of degraders and absorbers can be inserted into the beam path to separate protons and positrons from positively charged pions and electrons from negatively charged pions. In addition to the beam energy and intensity, the momentum bite of the beam is also adjustable, and, in this experiment,  $\Delta p/p$  was set to 2% for most of the data runs. The shape of the beam can also be controlled, and the incident pion beam was tuned to be cylindrically symmetric about the beam line with a full-width at half maximum dimension of about 1.1 cm.



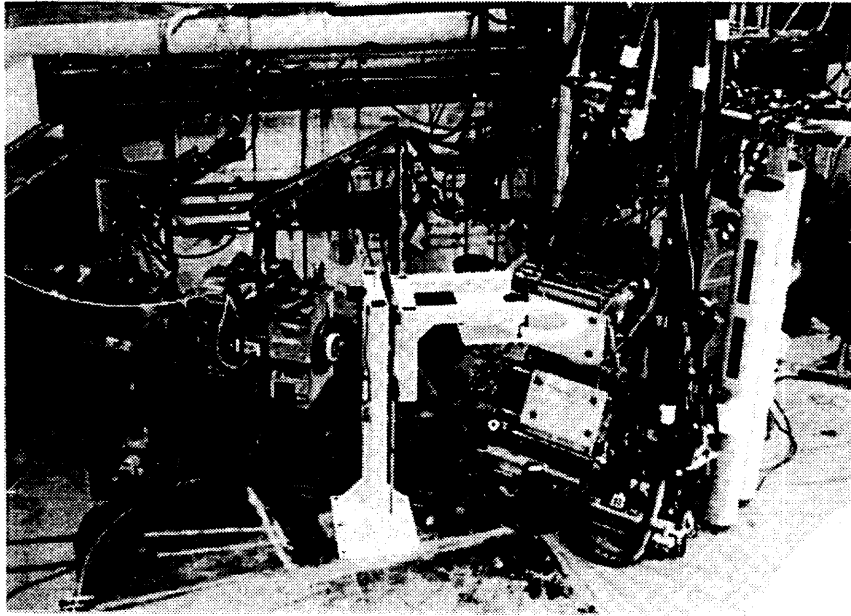


Figure 2.2: Photograph of the East cave at the  $P^3$  channel in the experimental hall A at LAMPF. The pion beam enters the experimental hall from the left. The target stand is in place awaiting installation of the  $^4\text{He}$  target. The  $\pi^0$  spectrometer is shown on the right.

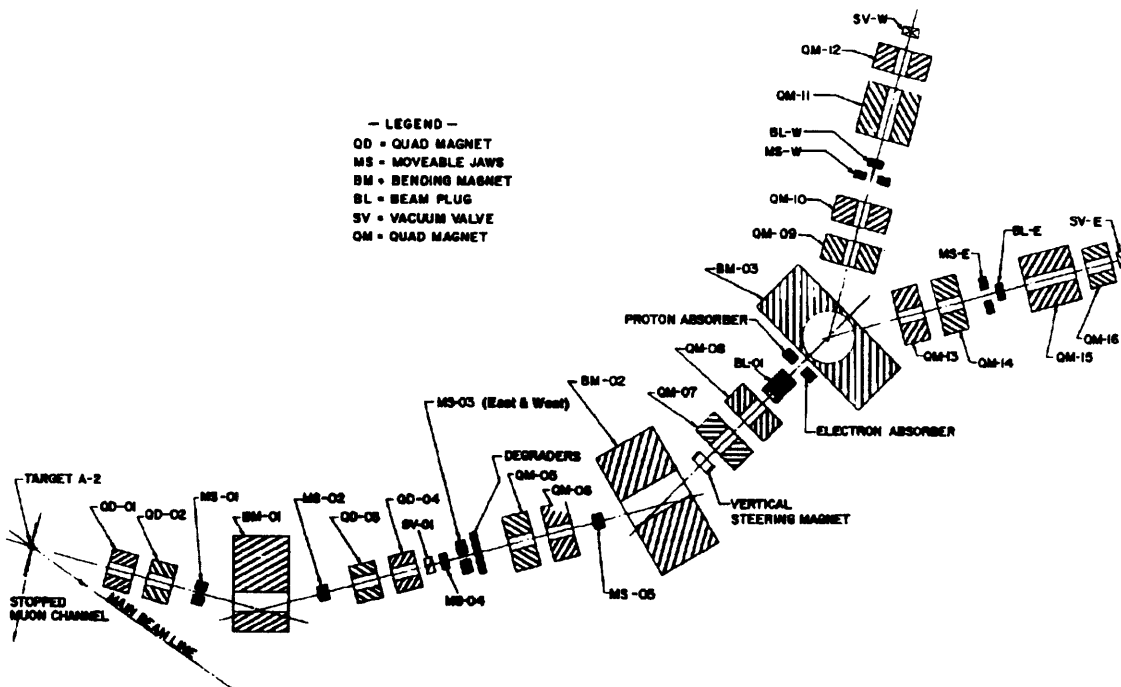


Figure 2.3: Diagram of the beam transport elements between the A-2 carbon production target and the East and West experimental caves of the Pion and Particle Physics ( $P^3$ ) channel at LAMPF. The diagram is from reference 38.

The settings for the beam transport elements were determined through the use of an established LAMPF beam transport program called NEWSHUNT. The aim is to create a mono-energetic beam of charged pions for use in the experimental areas. The  ${}^4\text{He}(\pi^-, \pi^0)\text{X}$  single charge exchange (SCX) reaction was studied with an incident beam energy of  $T_{\pi^-} = 160$  MeV. With the channel settings used during the experiment, the incident  $\pi^-$  beam had a flux of approximately  $1.8 \cdot 10^6 - 2.8 \cdot 10^6$  pions/second.

### 2.1.1 Beam Monitoring

An ionization chamber, placed about one meter upstream of the target just past a lead wall which helped eliminate the muon halo about the pion beam, measured the flux of charged particles incident on the target during a data run. This quantity must be known exactly in order to make an accurate measurement of a cross section. It was also kept in place throughout the experiment to record the relative intensities of the beam in each run. The active element in this device is Argon gas at atmospheric pressure. When a charged particle traverses the chamber, an amount of gas within is ionized. The volume of gas is partitioned with aluminized plates which are either grounded or kept at 600 V. The electric fields between these plates cause the ions and dissociated electrons to form a current which is linearly proportional to the quantities of charged particles in the gas. A digitized current output from the ionization chamber is then an indication of the incident beam flux.

A beam profile monitor consisting of two small multiwire proportional chambers was used to determine the shape and position of the incident beam upon the target. The wire spacings for these wire chambers were 1 mm, and the two chambers combined to give both vertical and horizontal information about the beam. The monitor was designed at LAMPF and includes electronics which time-averaged the amount of charge collected on each wire, a quantity related to the intensity of the incident beam, to provide an output display which was shown on an oscilloscope in the experimental counting house. The

beam profile monitor was left in place throughout the experiment with both wire chambers centered on the beam line. The monitor was attached to an ionization chamber with a hollow aluminum extension that placed it about 15 cm from the cryogenic target assembly (see figure 2.4).

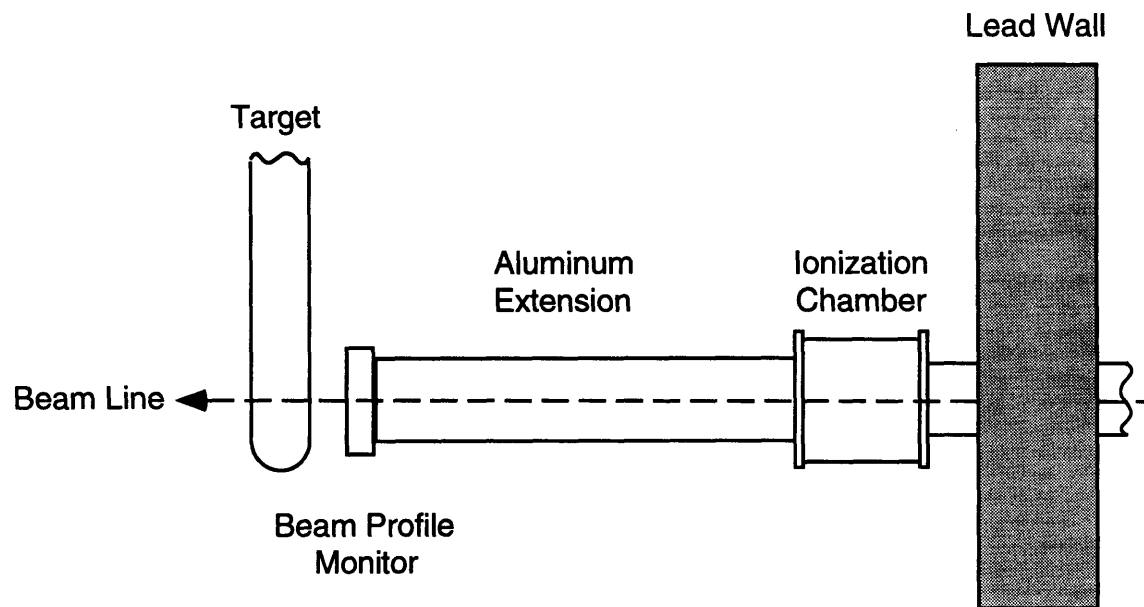


Figure 2.4: Along the beam line, the beam profile monitor was placed close to the cryogenic target. It was attached with a hollow aluminum extension to the ionization chamber.

### 2.1.2 Calibration of the Ionization Chamber: Activations

To determine the absolute flux of pions incident on the target, the ionization chamber was calibrated with a  $^{12}\text{C}$  scintillator activation technique which had been used successfully in many previous experiments at LAMPF. The key nuclear reaction involved is pion-induced neutron knockout in  $^{12}\text{C}$  to produce  $^{11}\text{C}$ , i.e.,  $\pi + ^{12}\text{C} \rightarrow ^{11}\text{C} + \pi + n$ . While the production of  $^{11}\text{C}$  can be induced by any particle in the beam, electrons and muons being the possible contaminants for a 160 MeV negative pion beam, lepton-induced contributions have been estimated to be less than 1% at our beam energies<sup>39</sup>. In other words, the

production of  $^{11}\text{C}$  is a process sensitive to the pion content of the beam. The cross sections for this pion-induced reaction have been accurately measured<sup>39,40</sup>, and  $^{11}\text{C}$  is known to decay through the reaction  $^{11}\text{C} \rightarrow e^+ + \nu_e + ^{11}\text{B}$  with a half-life of 20.3 minutes.

In undertaking the scintillator activation technique, our experiment used a procedure and an arrangement of detectors (figure 2.5) set up and maintained by the nuclear chemistry group at LAMPF. The procedure involves irradiating a thin 1.5 – 3 mm thick scintillator disk (CH) and measuring the  $\beta$ -decay of  $^{11}\text{C}$  created through the  $^{12}\text{C}(\pi^-, \pi^- n)^{11}\text{C}$  reaction. Since the disk is also a scintillator, the emitted  $e^+$  will produce light within the scintillator which can be detected in a photomultiplier tube. The positron may also annihilate with an electron inside the disk or a thin copper plate adjacent to it, a process resulting in two 511 keV  $\gamma$ -rays, one of which is detected with a NaI scintillator and phototube combination. The arrangement of detectors is designed to count the numbers of  $\beta$  particles detected,  $N_\beta$ , 511 keV annihilation  $\gamma$ -rays detected,  $N_\gamma$ , and coincidences between the two,  $N_{\beta+\gamma}$ . The three quantities are related to the true number of  $^{11}\text{C}$  decays,  $N_0$ , through the detector efficiencies,  $\epsilon_\beta$ ,  $\epsilon_\gamma$ , and  $\epsilon_{\text{coinc.}}$ , respectively, in the following equations:

$$N_\beta = N_0 \epsilon_\beta \quad (2-1)$$

$$N_\gamma = N_0 \epsilon_\gamma \quad (2-2)$$

$$N_{\beta+\gamma} = N_0 \epsilon_{\text{coinc.}} \approx N_0 \epsilon_\beta \epsilon_\gamma. \quad (2-3)$$

The number of  $^{11}\text{C}$  decays may then be established using a method<sup>41</sup> that is not dependent on the detector efficiencies in the following expression:

$$N_0 \approx \frac{N_\beta N_\gamma}{N_{\beta+\gamma}}. \quad (2-4)$$

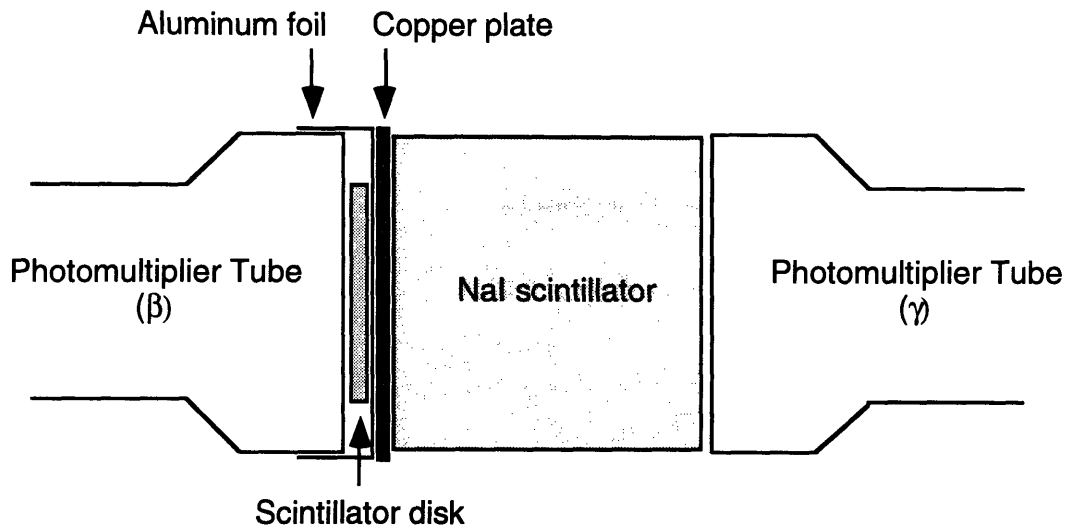


Figure 2.5: Diagram of the scintillator activation detector setup. A photomultiplier tube borders one side of the irradiated CH disk to multiply the photoelectrons from scintillator signals resulting from  $\beta$ -decay. A piece of aluminum foil on the other side serves as a reflector. A copper plate, NaI scintillator, and photomultiplier tube on the other side are used to detect a 511 keV  $\gamma$ -ray resulting from the annihilation of the positron.

$N_{\beta}$ ,  $N_{\gamma}$ , and  $N_{\beta+\gamma}$  were counted for several minutes to establish a decay curve and to determine the amount of  $^{11}\text{C}$  created during the irradiation. By using knowledge of the duration of irradiation, the constant of proportionality between the digitized ionization chamber current and the flux of incident pions can then be deduced.

During the experiment, eleven scintillator disks were used with Carbon thicknesses ranging from  $0.1590 \text{ g/cm}^2$  to  $0.2973 \text{ g/cm}^2$ . For each activation measurement, one disk was selected and placed in the beam for 120 seconds. The irradiated disk was then brought to the nuclear chemistry group detector setup where the number of  $\beta$  particles,  $\gamma$ -rays, and coincidences between the two were recorded over two minute intervals for 14 to 20 minutes total. This procedure was repeated once or twice a day, for a total of 32 independent activation measurements. Individual disks were not used for several days between irradiation periods to allow the created  $^{11}\text{C}$  to decay over many half-lives. The number of counts for each of these quantities was typically in the thousands, with the decay curve established to very high precision. As a result, the error in these measurements is almost entirely due to the 3-5% uncertainties in the  $^{11}\text{C}$  pion-production cross section.

## 2.2 Cryogenic Target

Our target was a cylindrical cryogenic  ${}^4\text{He}$  target originally constructed for LAMPF experiment number 564, which had also proposed to measure pion single charge exchange on  ${}^4\text{He}$ . The collaboration for that experiment, Ashery *et al.*, eventually only measured this reaction on a selection of solid targets (chapter 1), and the cryogenic target was never used. The target volume is a one-piece electroplated nickel cylinder and dome assembly that is 0.005 inches thick with a 4 inch diameter. The helium target was filled every two or three days through a vacuum-insulated transfer line by pressurizing a nearby 500 liter liquid helium dewar. The gas above the target was not pumped in the standard technique to lower the liquid temperature. As a result, the helium was at its boiling temperature at atmospheric pressure of 4.2° K. Given that the density of liquid helium at this temperature is 0.125 g/cm<sup>3</sup>, the thickness of the 4 inch helium target was 1.27 g/cm<sup>2</sup>. The target region is surrounded by a similarly-shaped heat shield that was 0.002 inches thick, 5 inches in diameter, and kept at liquid Nitrogen temperature. Like the target cell, the heat shield was a one-piece electroplated nickel assembly.

Two outer vacuum jackets were used. The first (shown in figure 2.6), used during the first half of the data run, was also an electroplated nickel vessel that was 0.020 inches thick, 6 inches in diameter, and of similar shape to the target cell and heat shield. With this outer shell, the support structure was far above the beam and out of the way of the detector, an advantage that was unfortunately lost with the second of the vacuum jackets. The presence of this material, amounting to 1.22 g/cm<sup>2</sup> of nickel, in the beam path created a substantial problem. The rate of SCX background reactions from the cryogenic target's nickel walls was comparable to the rate of SCX foreground reactions from the helium volume. This adversely affected the time required to take high-quality data and prompted us to replace the outer vacuum jacket in an effort to reduce the amount of material in the beam path.

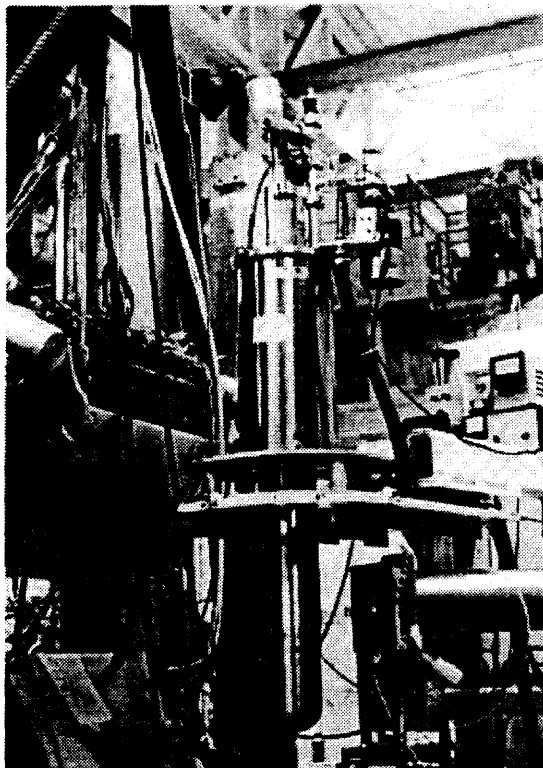


Figure 2.6: Photograph of the cryogenic  ${}^4\text{He}$  target with the first of two vacuum vessels used. The target is in a position several inches lower than where it would be during data taking to facilitate refilling the helium and nitrogen chambers from the top of the target. The two crates of the  $\pi^0$  spectrometer are shown on the left.

The outer vacuum shell was changed midway through the experiment to one 7.5 inches in diameter with mylar windows through which the incident beam could pass. This shell was also deep enough so that a dummy target, formed from two cylinders of nickel foil the same thicknesses as the target cell and nickel heat shield, could be attached to the heat shield beneath the helium volume for background runs. A second set of mylar entrance and exit windows six inches below those for the helium volume allowed background data to be taken with the dummy cell simply by lifting the entire target assembly.

While this change in vacuum shells helped lower the SCX background as planned, it was not without other problems. The support structures had to be modified for the new vacuum shell, and much material was moved closer to the beam and interaction region of the target in a manner that intersected the path between the target and spectrometer.

Photons resulting from  $\pi^0$  decay had an increased probability of being absorbed in this material before detection in the spectrometer crates, effectively decreasing the efficiency of the spectrometer for detecting  $\pi^0$ s. To a lesser extent, this problem was present with the original nickel vacuum shell, especially when the opening angle between the spectrometer crates was large. To take into account of this, the effects of the physical environment and the support structures on the spectrometer acceptance were modeled by a Monte Carlo simulation, as described in chapter 3.

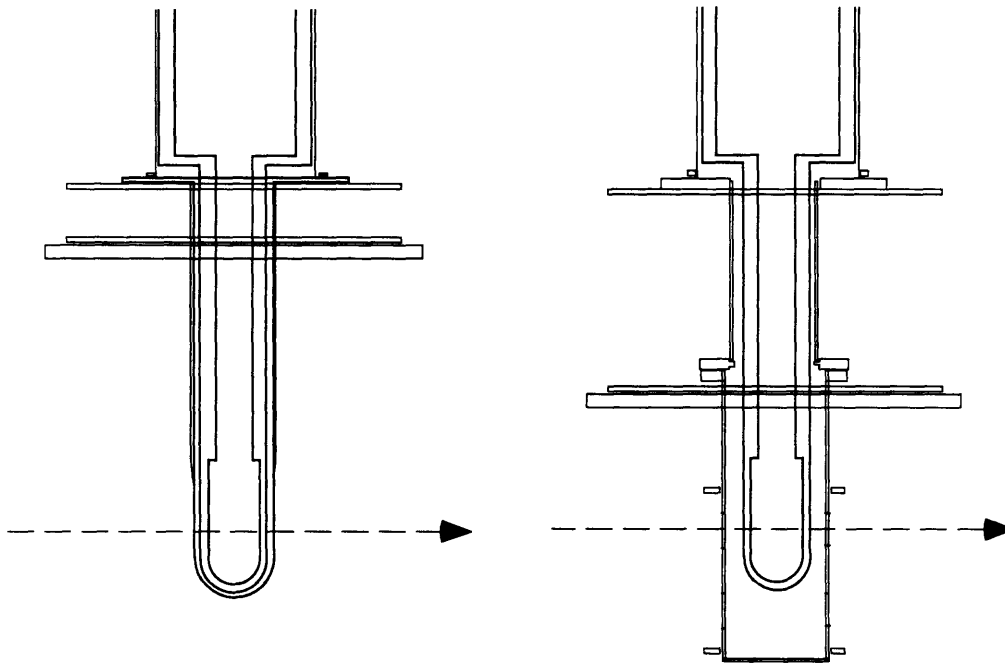


Figure 2.7: Schematics of the cryogenic target with the original nickel vacuum vessel (left) and the modified vacuum vessel (right) featuring mylar windows through which the incident beam passed. The support structures had to be modified also at this time, and much of the material from the supporting plates was moved closer to the beam line.

This problem adversely affected the usefulness of the dummy cell. Even though the background  $\pi^0$  production from the dummy target should be identical to that from the helium cell, the corrections to the detected  $\pi^0$  yields are not the same due to the different environments of each cell; the dummy target having all support structures six inches higher than where they would be for the helium cell. While using the dummy cell to measure the SCX background remained an option, the preferred method of measuring



---

background was to empty the helium volume and measure the  $\pi^0$  contribution from the empty target cell. In this way, the physical environments are the same for both the helium data and the corresponding background data.

## 2.3 The Detector: The LAMPF $\pi^0$ Spectrometer

The LAMPF  $\pi^0$  spectrometer, by the time of our experiment, was a well established detector with over a decade of service. Much documentation on this spectrometer exists elsewhere<sup>42,43,44</sup>, and only a general description of its parts and operation will be presented here as they relate to this measurement.

### 2.3.1 Detection Principle

The lifetime of the  $\pi^0$  is on the order of  $10^{-16}$  seconds, making direct observation of the neutral meson experimentally impossible. Its detection is accomplished by observing products from the  $\pi^0$ 's primary (98.8%) decay channel, the electromagnetic decay to two photons,  $\pi^0 \rightarrow \gamma\gamma$ . A correction to the  $\pi^0$  yield for the presence of the undetected, secondary (1.2%) decay channel  $\pi^0 \rightarrow e^+e^-\gamma$  was made during the calculation of the cross sections.

Photons resulting from  $\pi^0$  decay are emitted back-to-back and with equal energy in the  $\pi^0$  center-of-mass reference frame. When the trajectories of these photons are boosted to the laboratory reference frame, they are no longer back-to-back nor typically of equal energy (figure 2.8). Measurement of their laboratory energies and angles reveals the kinetic energy of the pion. The LAMPF  $\pi^0$  spectrometer (figure 2.9) is designed to detect both photons independently and to measure both the opening angle between the two decay photons and their energies. As seen in figure 2.10, the spectrometer consists of two identical photon detectors.

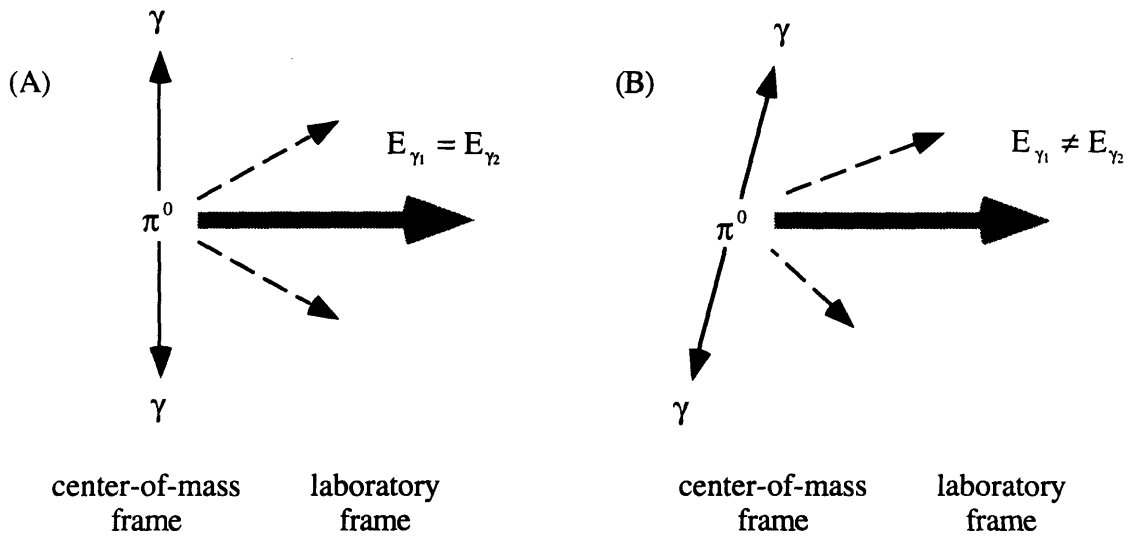


Figure 2.8: In the center-of-mass frame, the photons resulting from  $\pi^0$  decay are emitted back-to-back and with equal energy (solid arrows). Only when the photon trajectories are perpendicular (A) to the direction of the relativistic boost (thick gray arrow) are the two photon energies equal in the laboratory frame. The photon trajectories are distributed isotropically in the center-of-mass frame, however, and are typically not perpendicular (B) to the boost direction. In this case, the photon energies are not equal in the laboratory frame (dashed arrows).

If the opening angle is defined to be  $\eta$  and the quantity  $X$  is calculated as defined below, then the  $\pi^0$  total energy  $W_{\pi^0}$ , i.e., the kinetic plus rest mass energies, may be determined from the following expression:

$$W_{\pi^0}^2 = \gamma^2 m_0^2 = \frac{2m_0^2}{(1 - \cos\eta)(1 - X^2)} \quad (2-5)$$

where

$$X \equiv \frac{E_{\gamma_1} - E_{\gamma_2}}{E_{\gamma_1} + E_{\gamma_2}}. \quad (2-6)$$

While Eq. 2-5 is valid for any two photons detected, the LAMPF  $\pi^0$  spectrometer is designed to measure the opening angle between the photons more precisely than their energies. The negative effects of the moderate energy resolution can be minimized by selecting only those pairs of photons whose energies are nearly equal, i.e., when  $X \approx 0$ ,  $W_{\pi^0}$  is determined by  $\eta$  alone. This is done through establishing a parameter  $X_{\text{cut}}$  and

---

only including those events with  $|X| < X_{\text{cut}}$  in the measured  $\pi^0$  yield.

The events which do not satisfy  $|X| < X_{\text{cut}}$  must still be accounted for, however, even if they are not included and do not contribute to the measured  $\pi^0$  yield. The fraction of events not selected can be calculated since the quantity  $X$  has a distribution understood as resulting from the relativistic boosting of the back-to-back and isotropically distributed photons. By modeling this process in a Monte Carlo simulation, a correction for the fraction of discarded events was incorporated as a change in the effective spectrometer acceptance.

The choice of a small value for  $X_{\text{cut}}$  will increase the statistical uncertainty of any measurement, however, as fewer events will pass this restriction than if  $X_{\text{cut}}$  were made larger. This value must be picked wisely to minimize the statistical uncertainty while not adversely affecting the energy resolution. For this measurement,  $X_{\text{cut}}$  was chosen to be 0.25.

### 2.3.2 Detector Design

The signature for detection of a  $\pi^0$  is the simultaneous detection of photons, a gamma-gamma coincidence, in the two photon detectors which comprise the  $\pi^0$  spectrometer. These detectors, traditionally called the J- and K-crates, are designed to convert a high-energy photon into an electron-positron pair in one of three converter planes, each of which has about a 30% probability of converting the photon. The first element of each plane is a converter made of Pb-doped glass (2.2 cm = .58 radiation length) in which the photon may interact electromagnetically to produce an electron-positron pair. The pair may in turn interact further and create a shower of photons and charged particles. The Pb-glass is an “active” converter in that the energy lost by charged particles passing through will cause Cherenkov light to be emitted. This light is detected by one of five photomultiplier tubes as a measure of the energy deposited in the converter.

The trajectories of charged particles emerging from the back of the converters are tracked by multiwire proportional chambers, whose information is used to determine which of the three planes the photon converted in, as well as the exact location of conversion within the Pb-glass. In each plane, there are three wire chambers designated X, Y, and X' behind each Pb-glass converter. The X and X' chambers have 1 mm wire spacings and record wire hits in the direction determining the opening angle between the two photons. The Y chamber has wires with 2 mm spacings running perpendicular to those in the X and X' chambers and determines the scattering angle position with respect to the incident beam line. As there are three wire chambers behind each of the three converters in each crate, there are nine wire chambers in each arm of the detector.

A thin (3 mm) plastic scintillator is placed directly behind each set of three wire chambers to detect the presence of charged particles as they emerge from the back of the converters and wire chambers. The scintillators have a much faster response time than either the Pb-glass detectors or wire chambers and their signals determine the coincidence timing of the event. These detector elements can be grouped as three conversion planes in each spectrometer arm with each plane consisting of a Pb-glass converter; X, Y, X' wire chambers; and a plastic “timing” scintillator.

Behind the three converter planes, an array of 15 Pb-glass calorimeter blocks absorbs the full shower of particles created. The Cherenkov light output from the active converter and block elements is directly proportional to the incident photon energy. To ensure that an event is not initiated by a charged particle, a 2.5 cm slab of polyethylene was placed in front of each arm to prevent low-energy charged particles from entering the spectrometer, and a “veto” scintillator directly behind it and before the first converter plane was used to disallow any event initiated by charged particles that penetrated the polyethylene.

### 2.3.3 Wire Chambers

The operation of the multiwire proportional chambers is often troublesome, as the PCOS readout system has in the past produced an assortment of problems including non-functioning “cold” wires or “hot” wires which recorded a hit with every event. Information from hot wires must be discarded as they mimic the response of the wire chambers to actual charged particles. Along with cold wires, they contribute to a decrease in wire chamber efficiency as both lead to a loss in detector surface area available to detect a traversing particle. Occasionally, sections of the chambers could present problems since the wire chamber readout electronics are segmented along the length of each wire chamber. This was caused by poor connections between the cards holding the electronics and the chamber, and it was cured by reseating the card within its connector.

While our experiment experienced each of these problems, advance efforts to refurbish the spectrometer’s wire chambers and the PCOS system paid dividends as there were fewer incidents of hot or cold wires than in recent experiments. Most individual chambers had no hot wires, and the others chambers had two or three each. Typically, there would be through a dozen hot wires scattered about all eighteen wire chambers.

The identification of hot wires is important, because the criteria must take into account “warm” wires which fire more often than they should, but not as often as a truly hot wire. For our experiment, warm wires whose number of hits was four times greater than the average number of hits in the chamber were deemed hot and included into a list of hot wires. Truly hot wires which fired continuously had counts which far exceeded this. During data taking, a best-guess table of hot wires was constructed based on information from the previous run. This process is made more accurate in data replay, as a hot wire table could be constructed using information from the run itself.

### 2.3.4 Spectrometer Setup

For our measurement, the spectrometer was set up in the “one-post” configuration, one of its two possible setups (the other being the “two-post” configuration). In this configuration, both photon detectors are attached to a common vertical post. This choice of setup allowed measurement of the SCX reaction at the widest range of scattering angles. It also facilitated the movement of the spectrometer, lifted by pressurized air pads, to the various scattering angles and setup arrangements of our measurement as only one support structure needed to be moved.

The centers of each photon detector define the nominal opening angle and scattering angle of the spectrometer, and the solid angle acceptance is highest for the  $\pi^0$  total energy

$$W_{\pi^0}^2 = \frac{2m_0^2}{(1 - \cos\eta)}, \quad (2-7)$$

i.e., equation (2-5) when  $X=0$ . In addition to the nominal angles, the physical size of each photon detector allowed for a range of photon opening angles and scattering angles to be measured at each spectrometer setup. Typically,  $\pi^0$ s could be detected over a scattering angle range of close to  $30^\circ$ . Similarly, a range of  $\pi^0$  opening angles could be detected, and the corresponding range of  $\pi^0$  kinetic energies was about 45 MeV. The acceptance of the spectrometer was calculated precisely in the Monte Carlo simulation PIANG (described in chapter 3) as a function of  $\pi^0$  energy or scattering angle.

Spectrometer opening angles of  $\eta = 70^\circ$  and  $\eta = 95^\circ$  were used during the experiment to enable measurement of  $\pi^0$  energies from the kinematically allowed maximum down to about 30 MeV. Unlike typical experiments using the  $\pi^0$  spectrometer, the presence of a large cryogenic target meant that the plane of scattering could not be made horizontal with equal angles of inclination and declination for the two crates. If the vertical spectrometer support post were to be positioned at a horizontal distance far enough for the crates to

avoid hitting the target assembly, the bottom crate would strike the floor if the inclination and declination angles were equal. This problem was solved by adopting an inclined scattering plane. The angle of declination  $\eta_K$  for the bottom crate was decreased so it would not to hit the floor, and the angle of inclination  $\eta_J$  for the top crate was increased to make up the difference.

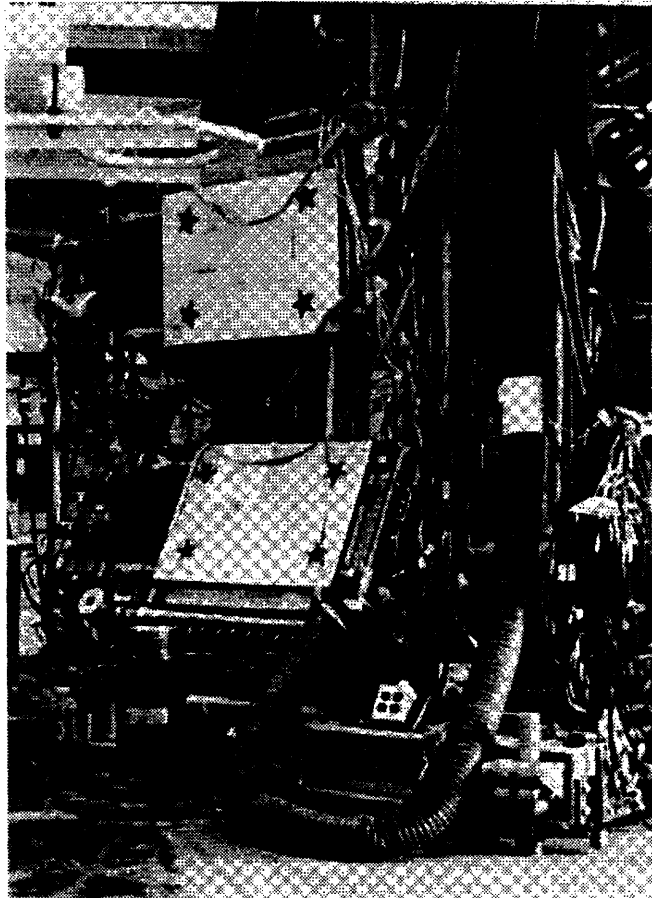


Figure 2.9: Photograph of the LAMPF  $\pi^0$  spectrometer which is comprised of two identical photon detectors attached to a single vertical post. The spectrometer is attached to and is free to rotate about a pivot to various scattering angles. The phototubes attached to the detector elements extend out to the left of the photograph. The large hose provides air conditioning for the wire chamber electronics. Smaller wires provide high voltage to the detector elements or carry signals to the counting house. The empty target stand can be seen at the top of the photograph as it awaits installation of the liquid helium cryogenic target.

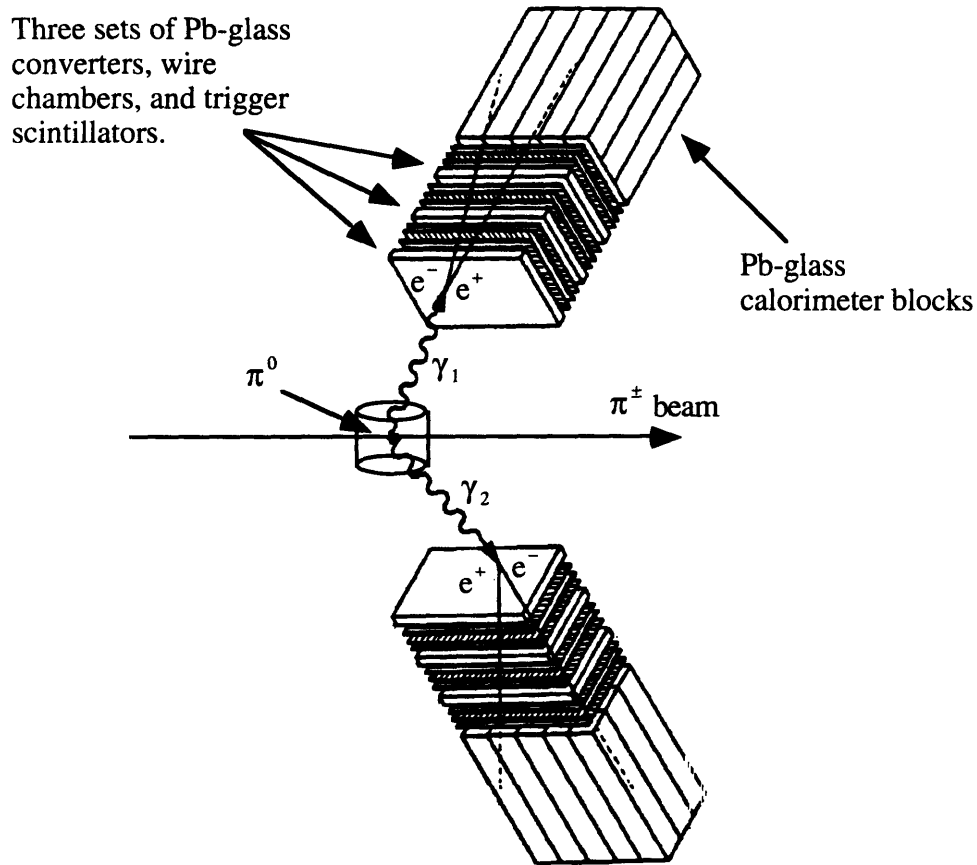


Figure 2.10: Schematic of the LAMPF  $\pi^0$  spectrometer showing the three converter planes and array of Pb-glass blocks. The veto scintillators are not shown.

As a consequence of both crates being attached to a single vertical post, the radial distances,  $\eta_j$  and  $R_K$ , from the target center to the front faces of the crates were not equal for both crates (shown in figure 2.11). This post position was chosen to minimize the distance from the target to the crates, thereby maximizing the solid angle for  $\pi^0$  detection. This different angles of inclination and declination and radii were consistently treated in the data analysis software and Monte Carlo modeling of the spectrometer acceptance (PIANG, as discussed in chapter 3).



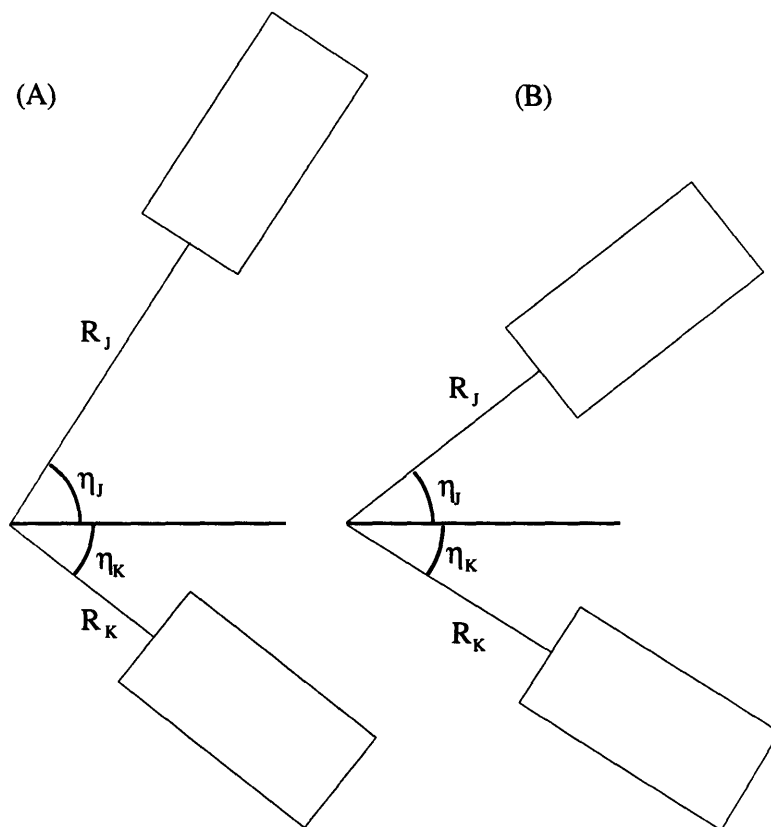


Figure 2.11: The opening angles required for this experiment necessitated unequal angles of inclination and declination, and consequently different radial distances from the target to the detector crates. Two opening angles of (A)  $95^\circ$  and (B)  $70^\circ$  were used to cover a large range of  $\pi^\circ$  energies.

Two different  $\eta = 70^\circ$  setups were used, the first called setup A which was later replaced by setup B when the most backward spectrometer scattering angle  $\theta = 130^\circ$  could not be reached. Setup B has slightly larger radii than setup A, as the vertical spectrometer post was moved away from the target in order to allow for more clearance between it and the spectrometer. Once Setup B was adopted, Setup A was never used again. The particular setup parameters used in Experiment 1177 are listed in table 2.1.

Experiment 1177 Spectrometer Setup Parameters			
	$\eta=70^\circ$ setup A	$\eta=70^\circ$ setup B	$\eta=95^\circ$
$R_j$ (cm)	97.96	115.33	134.44
$R_k$ (cm)	86.86	99.08	74.78
$\eta_j$ (deg)	$38^\circ$	$39^\circ$	$57^\circ$
$\eta_k$ (deg)	$32^\circ$	$31^\circ$	$38^\circ$

Table 2.1: The spectrometer setup parameters during the experimental run. The radial distances are measured from the center of the cylindrical target to the front face of the first Pb-glass converter plane.

## 2.4 Event Trigger and Electronics

The spectrometer makes use of much electronics and a DEC<sup>45</sup> microVAX computer to identify and process each  $\pi^0$  event trigger. This equipment resides in the experimental counting house, adjacent to the experimental cave and shielded from the beam. Signals from the various elements of the  $\pi^0$  spectrometer were first processed using high-speed electronics which is divided roughly into a trigger circuit and an enable circuit.

The trigger circuit determined which events would form a  $\pi^0$  event trigger to indicate the detection of a gamma-gamma coincidence and to initiate computer processing. If each  $\pi^0$  decay photon converts to an electron-positron pair in the Pb-glass converters, the charged particles will be detected as they emerge from the converters and wire chambers in the scintillator for that conversion plane. The first step in detecting a  $\pi^0$  is thus to define and require a valid scintillator event, that is for one or more of the three “timing” scintillators to record a hit, in both the J and K arms and for the veto scintillators not to fire. If this occurs in coincidence with a signal from any of the Pb-glass elements, the event is included as a  $\pi^0$  event. To express this criteria in logic notation, we define a scintillator signal for the two crates to be JS and KS; the signals of the three timing scintillators, S1,

S2, S3; the signal from the veto scintillator  $\overline{SV}$ ; and the combined signal from all of the Pb-glass elements JKG. The logical requirement for a “ $\pi^0$  event” is thus:

$$\pi^0 \text{ event} = JKG \cdot JS \cdot KS \quad (2-8)$$

with

$$\begin{aligned} JKG &= \sum J_{\text{Converters}} + \sum J_{\text{Blocks}} + \sum K_{\text{Converters}} + \sum K_{\text{Blocks}} \\ JS &= \overline{JSV} \cdot (JS1 + JS2 + JS3) \\ KS &= \overline{KS\overline{V}} \cdot (KS1 + KS2 + KS3) \end{aligned} \quad (2-9)$$

where a product represents a logical “and” and a sum a logical “or.” The electronics trigger circuit used based on this logical requirement is shown in figure 2.12.

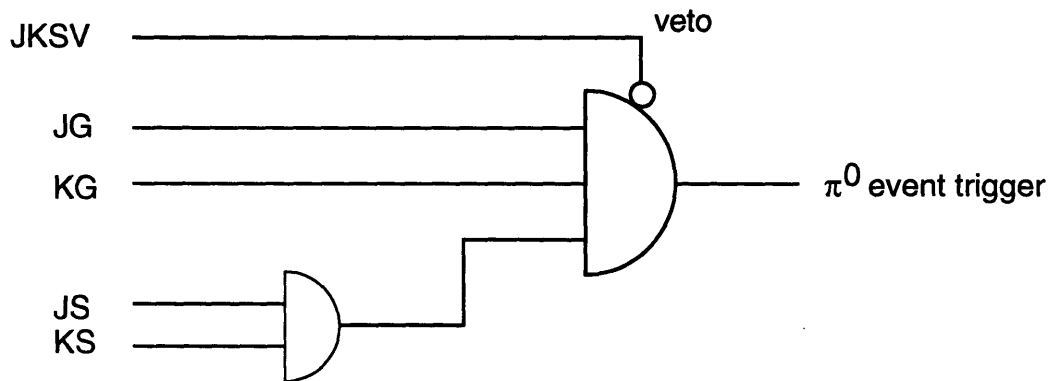


Figure 2.12: Diagram of the  $\pi^0$  event trigger circuit. The symbols are as defined in the text.

Based on three conditions, the enable circuit determined which  $\pi^0$  event triggers would be processed by the computer and recorded to magnetic tape as a “Master Trigger.” The first two simply required that a data-taking run must be in progress and that there be a pion beam in the experimental cave. The third restriction required that the computer must not be busy processing a previous event, and as a result, fewer  $\pi^0$  events were recorded to magnetic tape than the total possible number of such events. The electronics enable circuit is shown in figure 2.13.

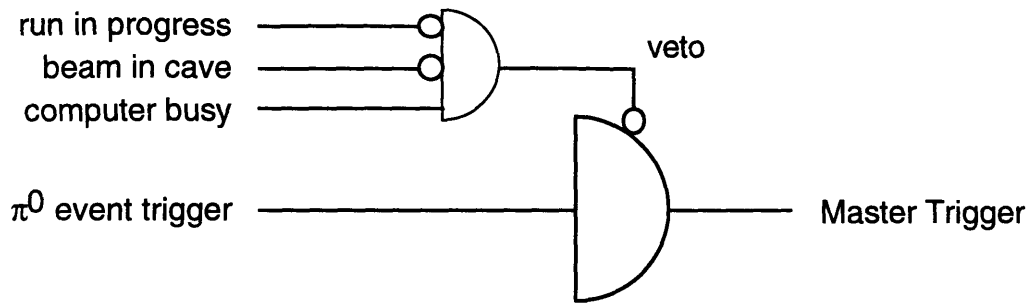


Figure 2.13: Diagram of the  $\pi^0$  event enable circuit.

As many  $\pi^0$  event triggers as possible were recorded to tape, typically 95-99% of all possible triggers, though it occasionally dipped as low as 92%. This fraction, known commonly as the “live time fraction,” was determined by computing the ratio of two scalers, one which incremented with each  $\pi^0$  event and the other which only incremented when the computer was not busy. It was precisely monitored and computed for each run, and the contributions from the triggers not written to tape were taken into account during the calculation of the cross sections. Similarly from those events written to tape, as many as possible, roughly 91% of all possible events, were processed on-line during data acquisition to aid in real-time analysis.

### 2.4.1 Recorded Information and Software

The information recorded to magnetic tape, apart from the title and time of the run, included data of five forms. First, the software parameters were recorded so that spectrometer geometry and calibration parameters would be readily available for future data replay. Those signals for which timing was important were processed with Time to Digital Converters (TDC). Secondly, the analog or linear pulse signals from the photomultiplier tubes, which are proportional to the energy deposited in the associated scintillator, were processed with Analog to Digital Converters (ADC). Scaler information, such as the ionization chamber counts, and counters used for calculating the live time were also recorded to tape. Finally, wire chamber information, which contained the number and position of hits, as well as the “cluster” width of each hit, was recorded to tape.

---

The “Q” package of software originally developed at LAMPF was used during both data acquisition and off-line replay. At the heart of “Q” is the event analyzer, which is software tailored for each experiment to process each event. In the analyzer, the raw information recorded to tape is processed into physical quantities of interest. For instance, TDC and ADC information is converted to time and energy quantities, and wire chamber and geometry parameters combined to determine opening or scattering angles. A test package allows detailed restrictions to be put on each event to determine quantities which are of interest, whether it be the  $\pi^0$  yield or the fraction of random events for the run. “Q” also allows histograms of quantities to be plotted for on-line monitoring, or off-line data manipulation. More detailed information about the general design, capabilities, and operation of “Q” may be found in its documentation and manuals.

### **2.4.2 Coincidence Timing**

The relative timing of the two photon detectors must be adjusted accurately to make a gamma-gamma coincidence detectable. Given the faster response time of the scintillators compared to the Pb-glass elements, their signals were used to determine the timing of each photon detected, the coincidences between the two arms, and subsequently the timing for  $\pi^0$  events. The phototube signals for the scintillators in each arm were adjusted with lengths of cable to arrive simultaneously when the detectors were triggered simultaneously. Then, signals from the Pb-glass converters and blocks in each arm were adjusted relative to the scintillator signals. Finally, to form a  $\pi^0$  event trigger, the signals from the scintillators and glass elements in both arms were adjusted to arrive simultaneously with the leading edge of the scintillator signal initiating the master trigger.

### **2.4.3 Pedestals and Stabilization**

Each of the sixty phototubes attached to the Pb-glass elements (each crate having fifteen

shower counters and fifteen converter elements) was monitored in order to maintain control over their energy calibration. This was accomplished with what are known to users of the  $\pi^0$  spectrometer as the pedestal and stabilization procedures.

Attached to each Pb-glass element is a small scintillator containing radioactive  $^{207}\text{Bi}$ <sup>42,46</sup> whose  $\gamma$ -spectrum is well understood and was recorded for each element during their initial calibration. At that time, each Pb-glass and phototube combination was calibrated with respect to the  $^{207}\text{Bi}$  spectrum by exposing each Pb-glass element to electron beams of known energies, a process which is tedious and was not repeated for this measurement.

During this experiment, the incident pion beam had a duty factor of roughly 6.3%, and the remaining 94% beam-off time was available and utilized to take  $\gamma$ -spectrum data of the radioactive sources during data acquisition. After 200,000 events were recorded, which occurred about once an hour during normal data taking, a comparison of the spectra was made to the saved reference spectrum for each detector element. Both the ADC pedestals and relative gains of the on-line spectra with respect to the saved spectra were calculated and recorded at this point. This procedure provided for more accurate energy calibrations during data taking and replay.

## 2.5 Normalization and Conversion Efficiencies

The detection efficiencies of the spectrometer's elements must be determined before an absolute measure of the SCX cross section can be made. This is done by normalizing the data to the known cross section for SCX from the free proton,  $p(\pi^-, \pi^0)n$ . A conversion efficiency is measured in the process; that is, the fraction of possible  $\pi^0$ 's whose decay photons are detected and correctly identified as resulting from a  $\pi^0$ . This determination requires two steps: the geometrical acceptance of the spectrometer must be calculated in a Monte Carlo simulation, i.e., the solid angle of the spectrometer available to detect the  $\pi^0$  by intersecting the paths of the decay photons, and a measurement of the  $p(\pi^-, \pi^0)n$

reaction must be made. For this, the cryogenic target was raised vertically out of the incident pion beam, and a polyethylene ( $\text{CH}_2$ ) target was placed in the beam line. The carbon background was measured by measuring the contributions from a graphite target. The ratio between this measurement, assuming the detector to be 100% efficient and using the solid angle  $\Delta\Omega$  calculated in Monte Carlo, and the known cross section gives the conversion efficiency.





## Chapter 3: Data Analysis

The experimental procedures in chapter 2 describe the manner in which our experiment was set up and data recorded to magnetic tape. There were 284 runs taken during the experimental run at LAMPF, of which about a fifth were used for setup, diagnostic in nature, or not incorporated into the data for various other reasons. The remaining runs measured one of four quantities (1) the  $\pi^0$  yield from single-charge-exchange on a Helium target, (2) the contribution of background processes to that yield, and the reaction to which our data were normalized, single-charge-exchange from the free proton using (3) polyethylene  $\text{CH}_2$  and (4) graphite  $^{12}\text{C}$  targets. The post-experiment analysis of these data, or data replay, and the calculation of quantities of interest is presented in this chapter.

For the presentation of the results of this experiment, the important quantity is the doubly differential cross section in the laboratory reference frame  $d^2\sigma/d\Omega_{\text{lab}}dE_{\pi}$ , which can be calculated using the following formula:

$$\frac{d^2\sigma}{d\Omega_{\text{lab}}dE_{\pi}} = \frac{N_{\text{det}}}{N_{\text{inc}}\Delta\Omega_{\text{lab}}\Delta E_{\pi}\rho_t f_{\text{live}}\epsilon_{\text{det}}} \quad (3-1)$$

where  $N_{\text{det}}$  is the number of scattered  $\pi^0$ s detected,  $N_{\text{inc}}$  is the number of incident charged pions,  $\Delta\Omega_{\text{lab}}$  is the solid angular acceptance of the spectrometer for the detected  $\pi^0$ s,  $\Delta E_{\pi}$  is the range in pion energy over which the  $\pi^0$ s were detected, and  $\rho_t$  is the effective thickness of the various targets in terms of scattering centers per unit area.  $f_{\text{live}}$  and  $\epsilon_{\text{det}}$  are the “live-time” fraction and detector efficiencies, respectively, of the  $\pi^0$  spectrometer and are corrections to the detected  $\pi^0$  yield. This formula displays the various quantities which must be determined in order to calculate a cross section, and the presentation of the analysis will address each term.

The quantities  $N_{\text{det}}$ ,  $\Delta\Omega_{\text{lab}}$ , and  $\Delta E_{\pi}$  are related in the following ways. For any setup, the

spectrometer subtended almost thirty degrees of scattering angle, and  $\pi^0$ s from each run were grouped into three  $10^\circ$  bins. The calculation of the solid angular acceptance,  $\Delta\Omega_{\text{lab}}$ , was made to reflect this fact. Furthermore, a limit was put on the maximum asymmetry allowed between the energy of the two detected photons, also known as the value  $X = (E_{\gamma_1} - E_{\gamma_2}) / (E_{\gamma_1} + E_{\gamma_2})$ . For each  $\pi^0$ ,  $|X|$  was restricted to be less than a numerical limit XCUT. This value directly affected  $N_{\text{det}}$ , and  $\Delta\Omega_{\text{lab}}$  was adjusted to remain consistent with the more restrictive selection requirements for the  $\pi^0$ . Finally, as the large physical size of the spectrometer allowed for a range of  $\pi^0$  kinetic energies to be measured with one experimental setup, the  $\pi^0$ s were grouped in bins of 5 MeV, the energy resolution given our experimental setup and choice of XCUT.

The corrections to the numbers of  $\pi^0$ s detected  $N_{\text{det}}$  are important as they reflect our understanding of the capabilities and limitations of the experimental setup. Had the spectrometer been 100% efficient in converting all decay photons from  $\pi^0$ s in the solid angular region  $\Delta\Omega_{\text{lab}}$  and detecting them as gamma-gamma event triggers, with a computer able to process all event triggers, the number of  $\pi^0$ s detected would have been  $N_{\text{det}} / (f_{\text{live}} \epsilon_{\text{det}})$ . This detector efficiency can be conveniently factored as the product of a conversion efficiency and wire chamber efficiency  $\epsilon_{\text{det}} = \epsilon_{\text{conv.}} \cdot \epsilon_{\text{wc}}$ . The conversion efficiency is the ability of the spectrometer's Pb-glass elements to detect  $\pi^0$ s and is calculated numerically as the fraction of all possible  $\pi^0$ s whose decay photons were successfully detected as resulting from a  $\pi^0$ . The wire chamber efficiency is the contribution of the wire chambers to the spectrometer's efficiency to detect  $\pi^0$ s. Both of the quantities are calculated separately, as presented below.

First, the number of incident pions will be determined through calibrating the ion chamber. Next, the determination of the  $\pi^0$  yield from processing data taken with the spectrometer will include descriptions of the wire chamber and Pb-glass analyses. The most important step in determining this yield is the selection of the parameter XCUT, as it affects the statistical accuracy and energy resolution of the measurement. The spectrometer's acceptance must also be accounted for, and it was calculated in a Monte Carlo simulation

PIANG, a program developed for this task. Substantial modifications, however, were made to the simulation to account for the photon absorption losses in the cryostat and its support structures. The last step in the analysis is the calculation of the conversion efficiency of the spectrometer, a process which determines the absolute normalization of the data. Finally, a discussion of the systematic errors for this measurement is presented.

### 3.1 Determination of the Incident Pion Flux

The first part of the analysis is to determine the number of charged pions incident upon the target  $N_{inc}$  by using the beam monitoring devices described in Chapter 2. The incident beam flux was measured with an ionization chamber whose digitized current signal was proportional to the beam current passing through. The total digitized charge was recorded to tape with a scaler which incremented during data taking. (Before run 79, the gating of this scaler was set incorrectly, and a slight 1-2% correction was made during data replay as described in Appendix A.) This quantity was known as the ionization chamber counts  $N_{IC}$  and was directly proportional to  $N_{inc}$  as follows:

$$N_{inc} = \alpha_{\pi/IC} \cdot N_{IC}. \quad (3-2)$$

The results from the scintillator activation method determined the scaling factor  $\alpha_{\pi/IC}$ . A total of twenty-one independent activation measurements were used over the course of the experimental period. As can be seen in figure 3.1, the ratios of pions to ionization chamber counts were constant over the course of the experimental run. The errors associated with these measurements are almost entirely due to the 3-5% uncertainties in the cross sections for the  $^{12}\text{C}(\pi^-, \pi^-)^{11}\text{C}$  reaction<sup>39,40</sup>. A weighted fit of a horizontal line to these data provided us with the calibration constant we needed for the ionization chamber,  $\alpha_{\pi/IC} = 1.91 \cdot 10^5$ .

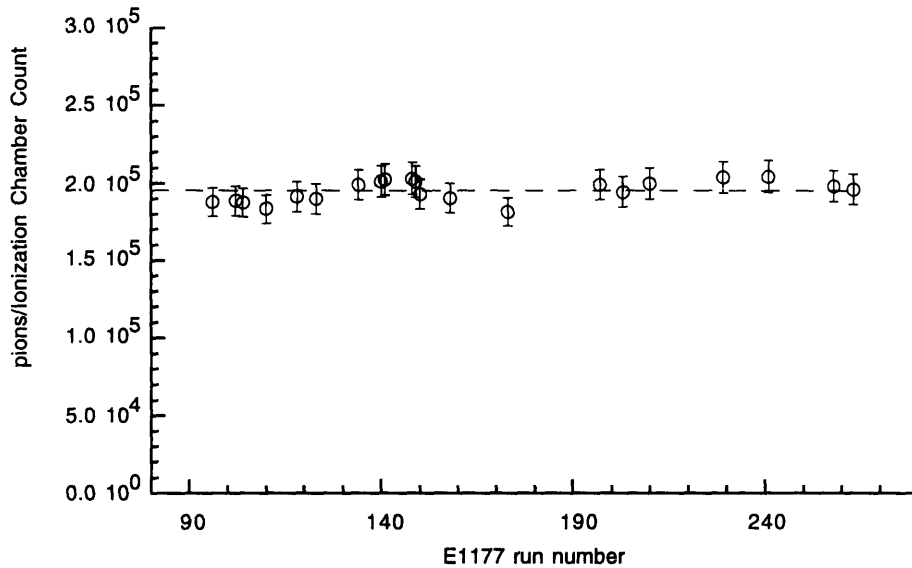


Figure 3.1: Summary of activation data and the scaling factor  $\alpha_{\pi/IC}$ . The Experiment 1177 run numbers are those for the runs immediately after each activation measurement. The dashed horizontal line has been fit to the data to determine  $\alpha_{\pi/IC}$ . The number of pions per ionization chamber count was determined to be  $\alpha_{\pi/IC} = 1.91 \cdot 10^5$ .

Since both the duration of irradiation for the scintillator disk is known and the number of incident charged pions is determined, the analysis of the scintillator activation data also provided us with a measure of the flux of pions incident upon the target. During the experiment, the incident  $\pi^-$  beam had a flux of approximately  $1.8 \cdot 10^6 - 2.8 \cdot 10^6$  pions/second.

### 3.2 Determination of $\pi^0$ Yield

The number of  $\pi^0$ s detected or yield,  $N_{det}$ , is determined through the analysis of the quantities recorded by the components of the spectrometer. As presented in chapter 2, the data acquisition electronics processed and stored data on magnetic tape in one of five forms: (1) ADC values, (2) TDC values, (3) wire chamber information, (4) scalars, and (5) parameters. As the spectrometer is designed to determine the opening angle between the two decay photons and the energy each deposited in the arms of the spectrometer,

---

these five “raw” quantities must be processed and analyzed in order to form the relevant physical quantities. This section presents the analysis of these data and the criteria used in designating whether an event was included in the yield  $N_{\text{det}}$ .

Roughly 94-99%, the “live time” fraction, of gamma-gamma event triggers were recorded to tape during data acquisition. Not all of these events, however, are the result of a  $\pi^0$ , as random coincidences in both arms of the spectrometer added to the total number of event triggers recorded. In addition, not all events determined to be the result of a  $\pi^0$  were included in the yield  $N_{\text{det}}$ . The XCUT test produced the single largest decrease in the numbers of  $\pi^0$ s included in the yield. Additional conditions placed on each  $\pi^0$  during data replay to define the properties of the cross sections, such as a partitioning based on the  $\pi^0$  kinetic energy or scattering angle, also combined to eliminate  $\pi^0$ s from the corresponding yield  $N_{\text{det}}$ .

In order to calculate a reaction cross section, the  $\pi^0$  yield from background processes such as single charge exchange from nuclei in the target cell walls, or even the air along the beam line, must be identified. To correct the Helium data, background runs were measured with similarly constructed dummy targets, and whenever possible, the cryostat itself with its Helium target cell evacuated. This latter provided the preferred measurement of the background, as the absence of liquid Helium in the target cell is the only difference between the foreground and background runs. Any additional differences in setup, such as lifting the cryogenic target as is necessary when using the dummy targets, must be modeled in a Monte Carlo simulation and will add to the systematic uncertainties of the results. After all these factors and restrictions are taken into account, the extracted  $\pi^0$  yield from the Helium target, or from the free protons in the  $\text{CH}_2$  target, is then the designated detected yield  $N_{\text{det}}$  used in calculating a cross section.

### 3.2.1 Pb-glass Analysis

Even though the spectrometer is designed so that the kinetic energy and energy resolution of the  $\pi^0$ s are primarily determined by the opening angle between the two decay photons, the measurement of their energies is important as well. This is not just because the  $X$  value for that event is included in the equation used in calculating of the  $\pi^0$  total energy. An essential step in determining whether or not a detected  $\pi^0$  is to be included into the number  $N_{\text{det}}$  is the determination of whether  $|X|$  is less than an XCUT limit, which was chosen to be 0.25 for this experiment. Since  $|X|$  is computed using the energy that each photon deposits in the arms of the spectrometer, these energies must be measured as accurately as possible despite the roughly 30% energy resolution of the Pb-glass elements.

The ADC values recorded for each phototube signal during a gamma-gamma event are proportional to the energy deposited in each scintillator and Pb-glass element. First, a non-linearity in the low-signal capabilities of the ADC electronics is corrected for using calibration constants for each ADC channel and a technique established by H. Baer *et al.*<sup>47,48</sup>. From each ADC value, a pedestal, or offset, is then subtracted to get a channel difference that is proportional to the energy deposited in that detector element. Finally, a scaling factor for the detector element as determined by the stabilization procedure relates the ADC channel to the energy deposited in that detector. The sum of all the energies deposited in all the detectors is then the energy of the photon.

During the experimental run, pedestal data were taken at the beginning of each run and every half hour afterwards during periods when the gamma-gamma event trigger was disabled. At that time, an "Event 16" was written to tape recording pedestal values. While this made the parameters readily available in replay, it was found that in some cases (and especially with particularly long data runs) pedestal positions shifted by a channel or two over time, with the parameter values recorded up to a half hour earlier not sufficiently accurate. As each ADC channel represents approximately a measurement of 0.5 MeV in deposited energy, a uniform shift of one channel for all sixty phototubes attached to the

---

Pb-glass elements would potentially lead to a measurement of deposited energy incorrect by 30 MeV. As will be shown in the following subsection addressing XCUT, a discrepancy this large is unacceptable as it dramatically affects the fraction of  $\pi^0$ s which survive elimination based on the XCUT test. This scenario did not happen often, fortunately, as shifts tended to be infrequent and random in nature, with pedestal shifts up and down roughly cancelling each other. The potential for problems, however, did motivate finding a procedure for more accurately determining pedestal values. As a check, the raw ADC spectra from all Pb-glass phototubes along with the values for the pedestals and gains were monitored frequently during the run for anomalies.

Pedestal parameters for all sixty Pb-glass elements were determined differently in data replay than during data acquisition, when they are calculated from the energy spectra, taken during the beam-off periods, of the imbedded  $^{207}\text{Bi}$  sources used also for the stabilization of the detector signals. In replay, pedestals were calculated from the data taken during gamma-gamma events themselves, i.e., the data that will go into the calculation of cross sections. Beam-related effects may be more accurately taken into consideration in this manner. Tables of these parameters were established in the process, and they were used instead of those written to tape as "Event 16"s during data acquisition.

To establish pedestal parameters, each data run was replayed to generate histograms of unaltered ADC spectra for each phototube. A typical spectrum is shown in figure 3.2. The peak channel for the pedestal is determined by the channel with the most counts. To designate a pedestal value, a weighted average was taken of the peak and adjacent channels which contain at least one-fourth the number of counts as in the peak channel. Tables of these pedestal centroids are saved for each run in files which were then used for any replay of the run in the future.

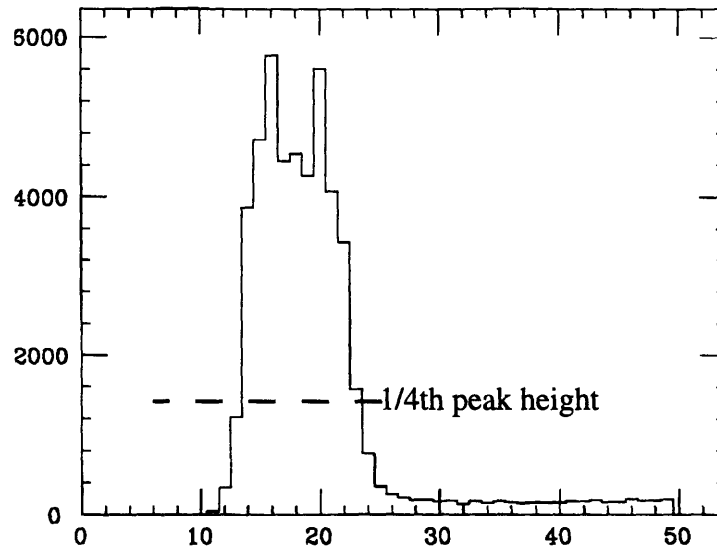


Figure 3.2: The low-channel portion of an ADC spectrum which displays evidence of a pedestal shift during the run (the KC08 converter from run 231). The pedestal centroid is designated as channel 18 from taking a weighted average of adjacent channels with over one-fourth the number of counts in the peak.

After subtracting pedestal offsets, the conversion of ADC information to units of energy requires the scaling of each ADC channel. These scaling constants were determined by the stabilization procedures (described in chapter 2) which determined the phototube gain in units of MeV/channel, monitored any drift in the gains during data acquisition, and recorded the parameters to tape for use during data replay. Unlike the pedestal values, no significant shifts or coherent shifts by groups of detectors were noticed in replay. Since these parameters are multiplicative and not additive as are offsets, any overall discrepancy should cancel to a great extent from the numerator and denominator when calculating the  $X$  value for each event.

### 3.2.2 Time Resolution: Elimination of Random Events

The difference in scintillator times for each  $\pi^0$  event,  $\Delta t = T_{J-\text{scint.}} - T_{K-\text{scint.}}$ , gives an indication of the time resolution of the electronic circuitry used to form the event trigger. By using wire chamber information to determine the distance between the phototube and



the point at which the charged particle passed through the scintillator, a correction was made for the speed of light within the plastic scintillator. A plot of time differences between the corrected scintillator times for both spectrometer arms is shown in figure 3.3 for a typical data run.

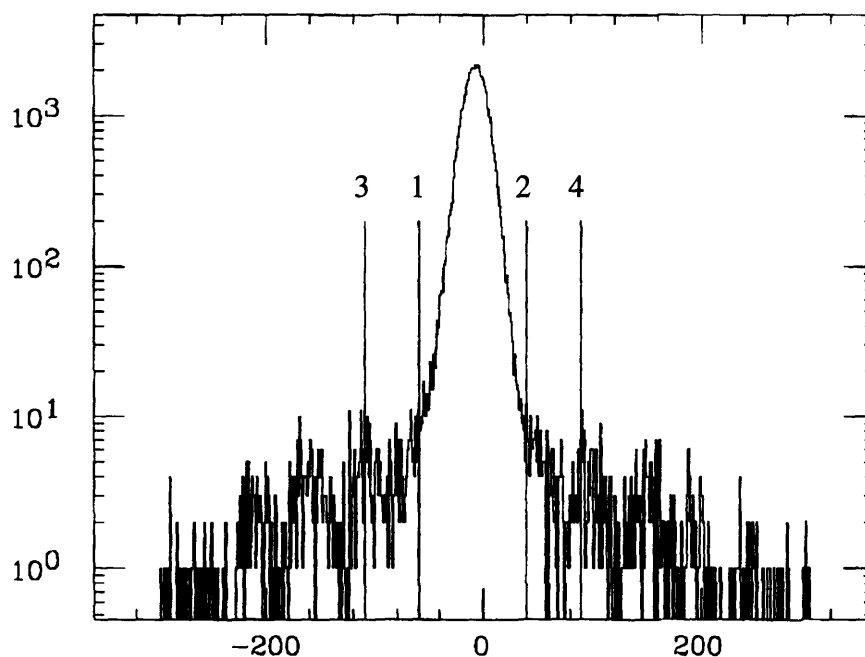


Figure 3.3: Plot of the time differences between scintillator signals from the two arms of the spectrometer. The “zero” for the x-axis is arbitrary and depends on lengths of cable between the detector elements and the electronics. The events between a 10 ns region between lines 1 and 2 are real coincidences. The events in the two 5 ns regions between lines 3 and 1, and lines 2 and 4 were used to estimate the contributions of accidental coincidences.

Events which form a master trigger need to be sorted into either real coincidences or accidental coincidences between the two photon detectors. The relative timing can also provide a measure of the number of random events recorded as gamma-gamma events which must be subtracted from the total  $N_{\text{det}}$  since they are not related to the reaction we are studying. Random events in each arm of the crate should not be correlated in time with respect to each other and thus should produce a flat spectrum.

The lines 1 and 2 in figure 3.3 define a 10 ns gate centered about the timing peak from

which events were designated as real coincidences which were then analyzed to determine how many resulted from  $\pi^0$  decay photons. In other words, only events for which signals from each arm arrived within  $\pm 5$  ns of each other were treated as candidates for good  $\pi^0$  events. The events that fell within lines 3 and 1, or lines 2 and 4, were analyzed in exactly the same manner as the good events, but their yield of  $\pi^0$ s was used to estimate the contributions from random coincidences under the timing peak. The fraction of random events for  $^4\text{He}$  and its associated background runs was typically 0.5%. For  $\text{CH}_2$  and  $^{12}\text{C}$  runs, the fraction was between 0.5% and 1.5%.

### 3.2.3 Wire Chamber Analysis

The information from the wire chambers is used for several purposes. First, it determines whether or not an event is to be discarded based on insufficient wire chamber information. For each spectrometer arm, it is also used to determine in which of the three Pb-glass planes the photon was converted to an  $e^+e^-$  pair and the location at which the pair was formed. Finally, if both arms are found to have detected conversions, the event is designated as a good  $\pi^0$  event. Several restrictions were placed on the wire chambers in determining whether a gamma-gamma event resulted from a detected  $\pi^0$ . The contributions from hot wires, as they are determined below, are always ignored, and the effects of this are taken into account during the calculation of the wire chamber efficiency for that run.

The processing of the wire chamber information is diagrammed in figure 3.4. To eliminate events on the basis of insufficient wire chamber information, the logic was as follows: If in the first plane with at least two of the three wire chambers recording a hit, all three chambers were hit, then the wire chamber information for that arm is valid. The first plane with all three chambers hit is designated as the plane in which the photon converted. If both arms record valid wire chamber information, the spectrometer has detected a  $\pi^0$ .

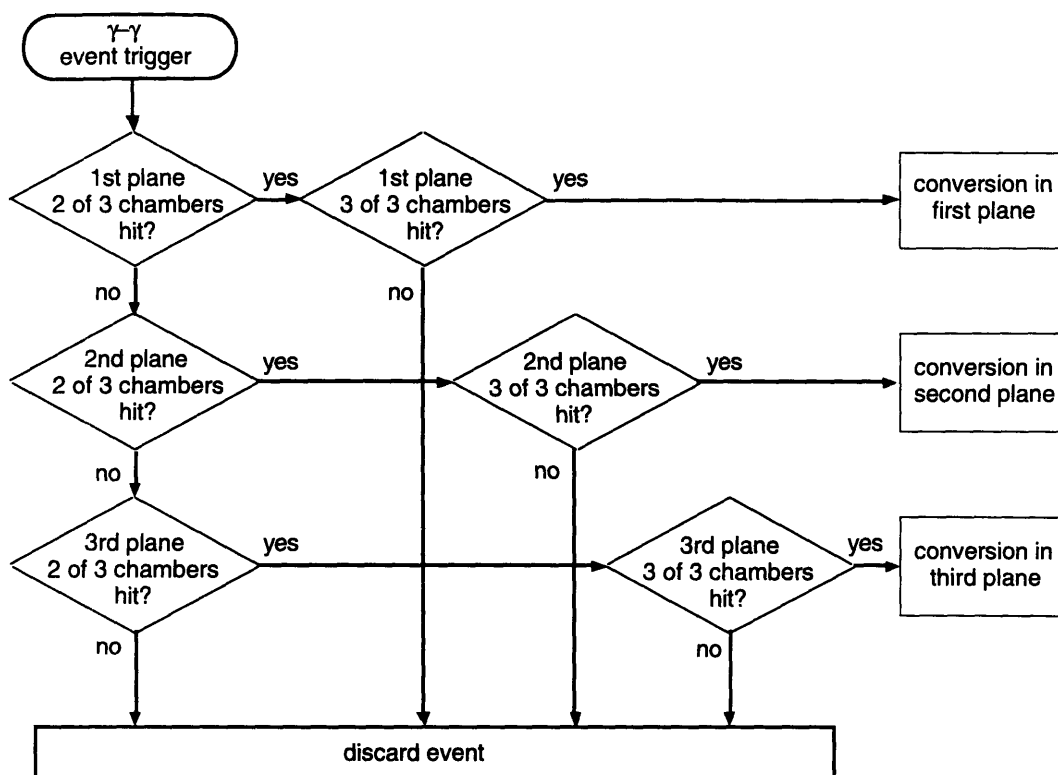


Figure 3.4: Flowchart illustrating the procedure for determining whether or not an event is to be discarded and if not, in which of the three planes the photon was converted to an  $e^+e^-$  pair. If both arms detect successful conversions, the event is a good  $\pi^0$  event.

To determine exactly where in the converter the  $e^+e^-$  pair originated, information from all three wire chambers in that plane is used, as illustrated in figure 3.5. The scattering angle position is taken to be the centroid of hits from the middle Y chamber whose wires span the scattering angle. The X and X' chambers have wires laid perpendicularly to those in the Y chamber to span the opening angle direction, and the line connecting a hit on both chambers can be traced back to the Pb-glass converter to determine the conversion position for that dimension. In the event that either or both of the X and X' chambers have more than one hit, the pair of hits, one from each chamber, with their positions closest together are taken to define this line. In this manner, the slope of the line connecting the hits is minimal compared to a path straight through the spectrometer. As these hits are thought to result from a higher energy electron or positron than those having a greater slope, the traceback using these hits is thought to be more accurate.

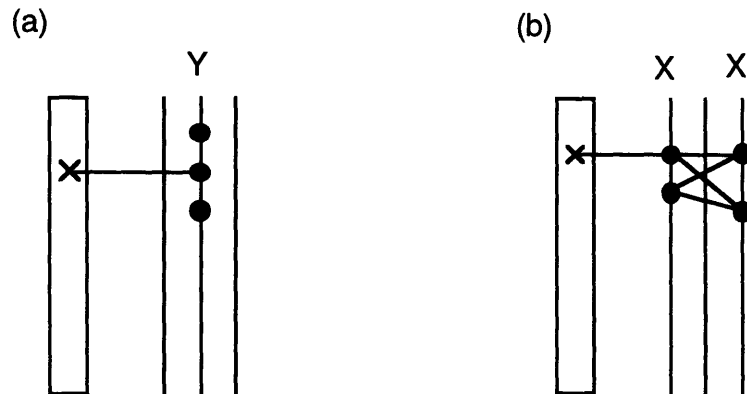


Figure 3.5: In each plane, information from all three wire chambers is used to determine the location in the Pb-glass where the photon converted to an  $e^+e^-$  pair. (a) The centroid of hits (black circles) in the Y chamber determine the scattering angle position of the conversion point (X). (b) The line connecting hits in the X and X' chambers which has the smallest slope with respect to the crate bisector is extended to the Pb-glass to determine the opening angle position of the conversion point.

Additional restrictions on the wire chambers helped determine whether or not this  $\pi^0$  will be included in the total  $N_{\text{det}}$ . First, at most five hits were allowed in each chamber. As 99% of all events typically had under five hits, this was not a major restriction. Secondly, a restriction was placed on the difference in slope between the line of traceback and one straight through the spectrometer. This was to avoid using two hits from unrelated tracks for traceback.

Finally, fiducial regions are designated for each chamber. The regions were determined to ensure that the shower of charged particles detected by the blocks would have at least eight radiation lengths,  $8\chi_0$ , of Pb-glass material in the blocks to be absorbed. Events outside these regions were ignored, as the shower might escape out the sides of the blocks resulting in a measurement of the shower's energy that was too low. Parameters in the Monte Carlo simulation to calculate the solid angle were adjusted accordingly for these fiducials.

### 3.2.4 Hot Wires

As discussed in chapter 2, the multiwire proportional chambers suffered from a problem known as having “hot wires.” During data acquisition, one had to generate a best-guess table based on the wire chamber operation for the previous runs. This table was modified to account for wires which subsequently malfunctioned, or which returned to proper operation. The hits from hot wires were then not included in the analysis of events during the data run. This was a software procedure<sup>49</sup> which did not affect the wire chamber information recorded on tape, i.e., hits on all wire chambers, including hot wires, were recorded.

In data replay, a different type of procedure was used to generate the hot wire tables than during data taking. In data replay, one can use hindsight to determine a more accurate hot wire table. Every data run was replayed once without any wires designated as hot in order to generate an unaltered wire spectrum for each of the eighteen chambers. Then, this spectrum was analyzed to determine which wires, if any, would be included in a hot wire table for that particular run. Wires with over four times as many hits as the average number of hits were designated as hot and placed in a table of hot wires for that run.

### 3.2.5 Wire Chamber Efficiencies

The spectrometer’s eighteen wire chambers were not 100% efficient, and for each data run, a wire chamber efficiency  $\epsilon_{wc}$  was calculated. This number contained the contribution from the individual efficiencies of the spectrometer’s wire chambers to the spectrometer’s efficiency to detect  $\pi^0$ s, i.e., the number of  $\pi^0$ s that would have been identified had the chambers been 100% efficient is  $N_{\pi^0}^{\text{detected}} / \epsilon_{wc}$ . The manner in which the eighteen individual chamber efficiencies are calculated and incorporated into  $\epsilon_{wc}$  for each data run is presented in this subsection.

The eighteen individual chamber efficiencies are calculated for each data run in the experiment using information from each  $\pi^0$  event. First, the wires which have previously been identified as “hot” and which have been recorded in a hot wire table for that run are ignored as they mimic a hit from a real particle and decrease the efficiency of the chamber. The method used for the twelve wire chambers in the second and third conversion planes in each arm was slightly different from that used for the six chambers in the first conversion planes in each arm. Both methods are described below.

For the second and third conversion planes, signals from the “timing” scintillator  $S_{\text{before}}$  immediately before the group of three chambers X, Y, X', and the scintillator  $S_{\text{after}}$  immediately after the chambers are required to be present to ensure that a charged particle traversed all three chambers. (Using the second conversion plane as an example,  $S_{\text{after}}$  is the scintillator from the second conversion plane, and  $S_{\text{before}}$  is the scintillator from the first conversion plane.) In addition to requiring that these two scintillators  $S_{\text{before}}$ ,  $S_{\text{after}}$  fire, the other two wire chambers are required to fire as a restriction on which events are to be included when calculating the efficiency for the third chamber in that group.

The efficiencies for individual wire chambers are then calculated as the ratio of the number of events in which  $S_{\text{before}}$ ,  $S_{\text{after}}$ , and all three wire chambers in that plane fired divided by the number of events in which  $S_{\text{before}}$ ,  $S_{\text{after}}$ , and at least the other two wire chambers fired. For example, the efficiency for an X chamber is calculated as follows:

$$\epsilon_X = \frac{S_{\text{before}} + S_{\text{after}} + WC_X + WC_Y + WC_{X'}}{S_{\text{before}} + S_{\text{after}} + WC_Y + WC_{X'}} \quad (3-3)$$

For the wire chambers from the first conversion planes in each arm, a slightly different criterion was used. The only scintillator in front of the chambers is the veto scintillator, but events including a signal from the veto were not recorded to tape as they were initiated by a charged particle. To calculate the individual efficiencies for wire chambers in the first conversion plane, a signal from the Pb-glass converter immediately before the chambers was required instead. The efficiencies for individual chambers from the first

conversion plane are then calculated as the ratio of the number of times  $C_{\text{before}}$ ,  $S_{\text{after}}$ , and all three wire chambers in that plane fired divided by the number of times  $C_{\text{before}}$ ,  $S_{\text{after}}$ , and at least the other two wire chambers fired. In this case, the efficiency for the X chamber would be calculated as follows:

$$\epsilon_X = \frac{C_{\text{before}} + S_{\text{after}} + WC_X + WC_Y + WC_{X'}}{C_{\text{before}} + S_{\text{after}} + WC_Y + WC_{X'}} \quad (3-4)$$

The individual chamber efficiencies for all eighteen chambers were typically around 95%-99%. As mentioned in section 3.2.3 and shown in figure 3.4, a valid  $\pi^0$  event requires that the first group of X,Y,X' chambers to have at least two chambers fire must have three chambers fire. Among the valid events, the first conversion plane which has all three wire chambers fire is designated the plane of conversion. We then define efficiencies for each of the three planes  $\epsilon_1$ ,  $\epsilon_2$ ,  $\epsilon_3$  due to the three wire chambers in that plane by the product of the three individual chamber efficiencies, i.e., the efficiency for the first plane is  $\epsilon_1 = \epsilon_{1X} \cdot \epsilon_{1Y} \cdot \epsilon_{1X'}$ . These conversion plane efficiencies varied between 93%-99% depending on the individual chamber efficiencies for that run.

An efficiency for each arm of the spectrometer  $\epsilon_{J\text{-arm}}$ ,  $\epsilon_{K\text{-arm}}$  can be calculated using these values of conversion plane efficiency, but it is not calculated as the product of  $\epsilon_1$ ,  $\epsilon_2$ ,  $\epsilon_3$  since that would imply that all three sets of wire chambers were required to fire. Rather, it must involve the information of how many  $\pi^0$ s, as opposed to  $\gamma-\gamma$  event triggers, were included in the  $\pi^0$  yield. If  $N_1^{\pi^0}$  is the number of times a  $\pi^0$ , which has passed all restrictions including the XCUT test, resulted from a photon converting in the first conversion plane, the number of  $\pi^0$ s the plane would have detected had the wire chambers in that plane been 100% efficient, is  $N_1^{\pi^0} / \epsilon_1$ . There are three conversion planes in each arm, and the efficiencies of each arm due to these quantities as combined in formula (3-5) which weights each conversion plane efficiencies by the plane's contribution to the total  $\pi^0$  yield. The efficiencies for each arm typically varied between 94% - 97% as calculated by:

$$\epsilon_{J\text{-arm}} = \frac{N_1^{\pi^0} + N_2^{\pi^0} + N_3^{\pi^0}}{N_1^{\pi^0}/\epsilon_1 + N_2^{\pi^0}/\epsilon_2 + N_3^{\pi^0}/\epsilon_3}. \quad (3-5)$$

Finally, the total wire chamber efficiency is defined as  $\epsilon_{wc} = \epsilon_{J\text{-arm}} \cdot \epsilon_{K\text{-arm}}$ , since the determination of a  $\pi^0$  involves a coincidence between both arms of the spectrometer. This value varies between 88% and 95%. Typical values for the efficiencies of the individual wire chambers, the conversion planes, each spectrometer arm, and the total wire chamber efficiencies are given in table 3.1.

	J-Crate	K-Crate
<b>Individual Chamber Efficiencies</b>		
$\epsilon_{1X}$	98.9	99.5
$\epsilon_{1Y}$	98.7	99.9
$\epsilon_{1X'}$	98.0	99.9
$\epsilon_{2X}$	98.9	99.1
$\epsilon_{2Y}$	99.0	99.6
$\epsilon_{2X'}$	97.0	97.1
$\epsilon_{3X}$	98.3	98.7
$\epsilon_{3Y}$	99.5	99.3
$\epsilon_{3X'}$	96.1	95.5
<b>Conversion Plane Efficiencies</b>		
$\epsilon_1$	95.7	99.3
$\epsilon_2$	95.0	95.8
$\epsilon_3$	94.0	93.6
	$\epsilon_{J\text{-arm}} = 95.1$	$\epsilon_{K\text{-arm}} = 96.9$
<b>Total Wire Chamber Efficiency</b>	$\epsilon_{wc} = 92.1$	

Table 3.1 Typical values for the efficiencies (in percent) of the individual wire chambers, the conversion planes, each arm of the spectrometer, and the total wire chamber efficiency.

### 3.3 XCUT

The XCUT test, the limit on  $X = (E_{\gamma_1} - E_{\gamma_2}) / (E_{\gamma_1} + E_{\gamma_2})$  such that  $|X| \leq \text{XCUT}$ , is the single largest eliminator of  $\pi^0$ s from the yield  $N_{\text{det}}$ , used in calculating the cross section.



Roughly a third of all event triggers eliminated by the test package fail XCUT. The factors which affect this important test thus need to be studied carefully. The shifts in pedestal values above, and problems in determining the spectrometer's conversion efficiency described below, put even greater emphasis on studying the effects of this test on the results. In an effort to address these problems, a large part of the discussion below will focus on the expected X-distributions of  $\pi^0$ 's of different energies since the conversion efficiencies were determined over a range of quasifree energies. Inaccurate measurements of the photon energies may have led to a change in the shape of these distributions which, in turn, affects the fraction of events passing or failing XCUT. The  $\pi^0$  yield is then affected, making the determination of the conversion efficiencies difficult.

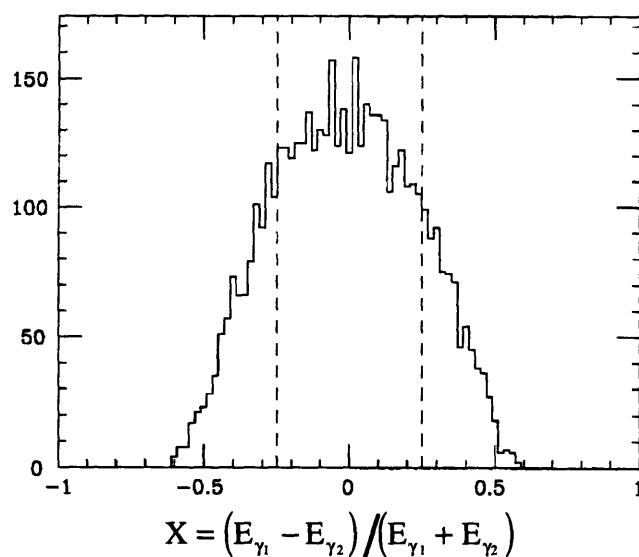


Figure 3.6: The X distribution for  $\pi^0$ 's of 96 MeV, close to the nominal kinetic energy of 100 MeV for the spectrometer opening angle of  $\eta = 70^\circ$ . The distribution is peaked at  $X=0$  and falls off rapidly on both sides. The dashed lines are at the limit  $XCUT=0.25$ ;  $\pi^0$ 's outside the limit are excluded from the yield.

In its center of mass frame, the  $\pi^0$  decays isotropically to two back-to-back photons of equal energies. Boosting these photons to the laboratory frame decreases the opening angle between the two photons and causes the energies in general to be unequal. For any spectrometer setup, the nominal opening angle defines a nominal  $\pi^0$  total energy

$$W_{\pi^0}^2 = \gamma^2 m_0^2 = \frac{2m_0^2}{(1 - \cos\eta)(1 - X^2)} \quad (3-6)$$

by setting  $X=0$ . The  $X$  distribution of  $\pi^0$ s of this nominal energy is peaked at zero and varies between  $-\beta$  and  $+\beta$  ( $\beta = \frac{v}{c}$ ). For illustration, the  $X$  distribution generated in a Monte Carlo simulation for  $\pi^0$ s of 96 MeV, close to the nominal kinetic energy of 100 MeV for the  $\eta = 70^\circ$  opening angle, detected by the spectrometer is shown in figure 3.6.

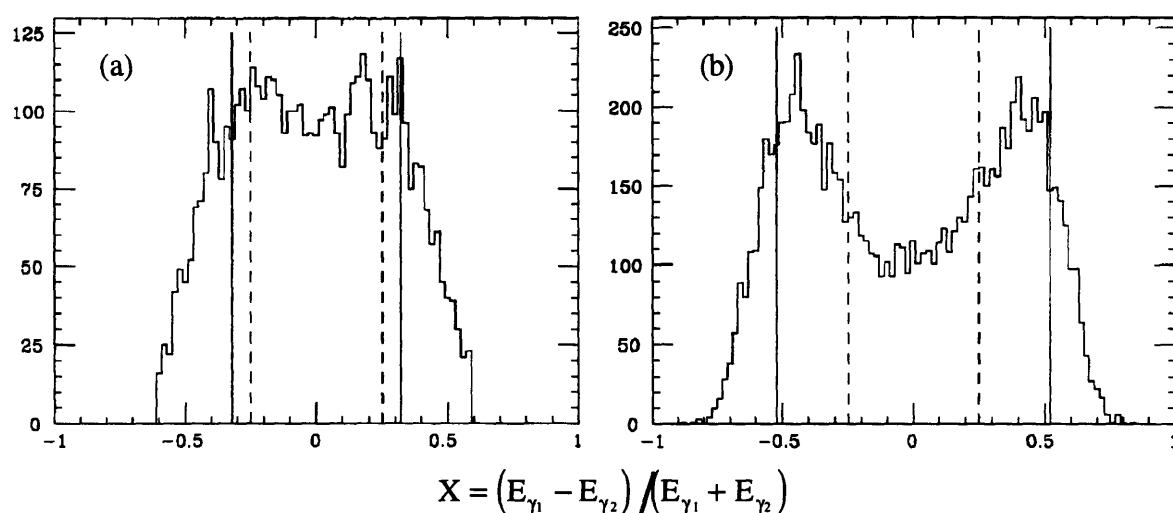


Figure 3.7: The  $X$  distributions for  $\pi^0$ s of (a) 113 MeV and (b) 140 MeV. Note that the shapes are dramatically different from the distribution at 96 MeV (figure 3.6). The dashed lines are at the limit  $XCUT=0.25$ , and the solid lines are the preferred  $X$  values for each energy with the opening angle  $\eta = 70^\circ$ . For higher energies, a larger fraction of the  $X$  distribution fails the  $XCUT$  test, and a higher fraction of  $\pi^0$ s are excluded from the yield.

The shape of the  $X$  distribution changes dramatically when measuring  $\pi^0$  energies different from the nominal energy. For instance, the distribution for 113 MeV  $\pi^0$ s is considerably wider, and two peaks have begun to appear at 140 MeV (figures 3.7a and 3.7b). The explanation for these changes is that the  $X$ -distribution is affected by the strongly peaked acceptance of the spectrometer. For any  $\pi^0$  energy, the central spectrometer opening angle  $\eta = 70^\circ$  defines a value

$$X^2 = 1 - \frac{2m_0^2}{(1 - \cos \eta)W_{\pi^0}^2} \quad (3-7)$$

which is obtained by rearranging equation 3-6. The corresponding positive and negative values  $\pm X$  can be thought of as “preferred” values of  $X$  due to the peaked acceptance of the spectrometer. The preferred  $X$  values are 0.32 and 0.52 for 113 MeV and 140 MeV, respectively. These values are close to edges of the 113 MeV distribution and peaks of the 140 MeV distribution. They do not fall exactly on the peaks at 140 MeV due to the size of the spectrometer.

The effects of an  $X$  distribution whose width is changing on the  $\pi^0$  yield are considerable since the value for  $XCUT$  is fixed in the analysis. When the distribution is broadest, a larger fraction of  $\pi^0$ s will fail the  $XCUT$  test since more of the distribution is outside  $XCUT=0.25$ . At any particular energy, the distribution is also a strongly varying function of  $X$ , and an inaccurate measurement of the energies deposited in the crates may make it narrower or broader. Consequently, a larger or smaller fraction of events will pass the  $XCUT$  test if this occurs. This places a premium on the quantities which affect the calculation of  $X$ , the accurate calibration of the Pb-glass and the measurement of the deposited energies in each spectrometer crate.

When measuring a range of  $\pi^0$  energies with the  $\pi^0$  spectrometer, as in our experiment, the  $X$ -distribution is typically not so structured or double-peaked as it is for 140 MeV in figure 3.7b. Averaged over a range of energies, it is generally flat over a large range of  $X$  values before dropping off quickly. When the doubly differential cross section has a strong peak or energy dependence, however, the shape of the  $X$  distribution is strongly affected to resemble the distribution for  $\pi^0$ s of the peak energy. This is the case for our normalization measurements of SCX from the free proton using a  $CH_2$  target. The SCX peak varies in energy at different scattering angles, while the spectrometer opening angle is fixed at  $\eta = 70^\circ$ . The  $\pi^0$  energies 96 MeV, 113 MeV, and 140 MeV, whose  $X$  distributions are shown in the figures 3.6 and 3.7, correspond to the SCX peak energies at  $\theta = 105^\circ$ ,  $80^\circ$ , and  $50^\circ$ , respectively. These are three of the four angles at which the

spectrometer conversion efficiencies were measured in this experiment.

It might be thought that increasing XCUT from 0.25 to a larger value would, at some cost in energy resolution, move the XCUT test to a region of the distribution less sensitive to the test as well as providing additional statistical accuracy. While this may be possible at higher incident beam energies<sup>30</sup>, it has limited returns at our beam energy of 160 MeV where the detected X distribution is limited due to the limited physical size of the two spectrometer crates. When the energy sharing between the two photons becomes more highly asymmetric, the opening angle between the photons increases as well. At some point, the opening angle will be larger than physically possible to detect with the spectrometer. A limit for XCUT is defined therefore by the largest opening angle detectable by the spectrometer. For the incident beam energy of 160 MeV, this limit is 0.74, as shown in figure 3.8. Scattered  $\pi^0$ s, however, have lower energies, and their limits decrease, especially at the low-energy end of the spectrometer's acceptance.

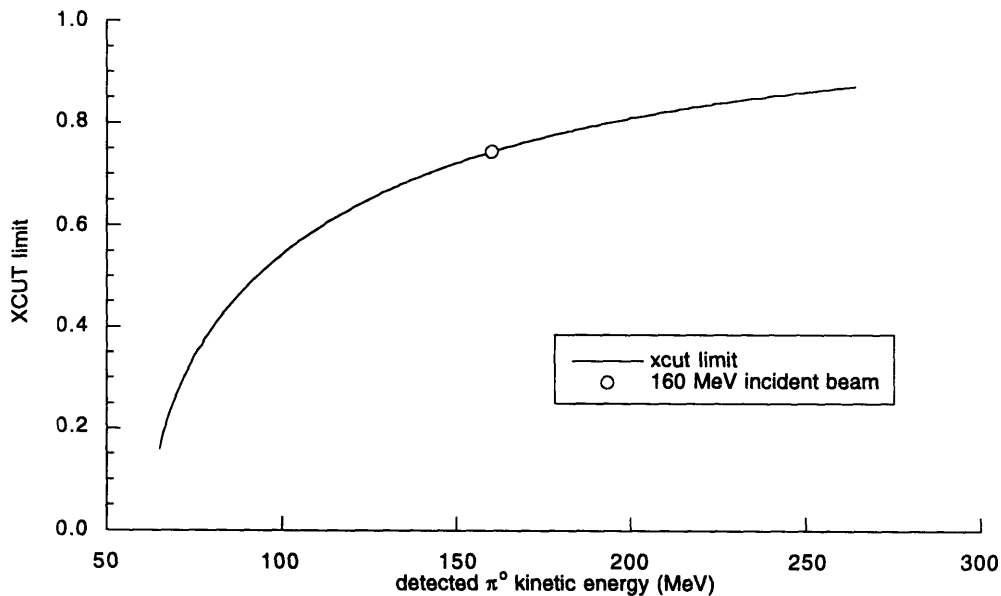


Figure 3.8: Increasing the value of XCUT beyond the XCUT limit will not help gather more statistics because the opening angle of the  $\pi^0$  would be greater than the maximum opening angle of the spectrometer. For the incident beam energy in this experiment, this limit is 0.74. The limits for scattered  $\pi^0$ s, which have lower energies, have an even lower XCUT limit. The above is calculated with opening angle limits determined from the  $\eta = 70^\circ$  setup A spectrometer geometry.

To be less sensitive to the absolute width of the X distribution, the value of XCUT must not be chosen so as to be placed near the steep edges of the X distribution. This is a near impossible task, as XCUT is fixed, but the width (and shape) of the distribution changes with increasing  $\pi^0$  energy. At the low energy end of the spectrometer's acceptance, XCUT=0.25 is already close to the XCUT limit. Increasing XCUT would only cut along the edge of the distribution at higher energies. Furthermore, an increase of XCUT would also not substantially increase the numbers of  $\pi^0$ s detected or the statistical accuracy of our measurement, especially at low energies. Given these considerations, XCUT was chosen to be 0.25 and not a larger value.

### 3.4 Calculating the Acceptance of the Spectrometer

The acceptance of the spectrometer is defined to be that solid angle  $\Delta\Omega$  available for detecting a scattered particle, a necessary quantity in the determination of a reaction cross section. For the  $\pi^0$  spectrometer, the acceptance is dependent on several quantities, including the kinetic energy and scattering angle of the  $\pi^0$ . A Monte Carlo program called PIANG<sup>51</sup>, initially written at the time of commissioning of the spectrometer and developed by following experimenters to incorporate refinements, calculates this quantity given the setup parameters of the experiment. An unmodified version of PIANG was used to calculate the acceptance for the CH<sub>2</sub> and <sup>12</sup>C targets whose slab target geometry was already defined in the program. For the Helium data and background data, the program had to be modified substantially, as presented below. Details about PIANG can be found elsewhere<sup>51,43,44</sup>. A description of its results will be presented here as they relate to this experiment.

The spectrometer acceptance is greatest for detecting a  $\pi^0$  whose kinetic energy when X=0 corresponds to an opening angle equal that of the spectrometer's nominal opening angle  $\eta$ . From there, the acceptance falls off as the energies reach the limits of the spectrometer's capabilities. The minimum kinetic energy  $T_{\min}$  which can be measured

before the acceptance becomes zero is determined by

$$T_{\min} = m_{\pi^0} \left( \sqrt{\frac{2}{1 - \cos \eta_{\max}}} - 1 \right) \quad (3-8)$$

where  $\eta_{\max}$  is the largest opening angle between the fiducial regions of both arms, a quantity which is measured diagonally from the corners of the regions. In this case, the decay photon energies are equal in the laboratory, i.e.,  $E_{\gamma_1} = E_{\gamma_2}$  and  $X = 0$ . The maximum energy detectable  $T_{\max}$  not only involves the minimum angle between the fiducial regions  $\eta_{\min}$  but also involves the XCUT value set in replay for detecting  $\pi^0$ 's as follows:

$$T_{\max} = m_{\pi^0} \left( \sqrt{\frac{2}{(1 - \cos \eta_{\min})(1 - \text{XCUT}^2)}} - 1 \right) \quad (3-9)$$

$T_{\max}$  increases with increasing XCUT.

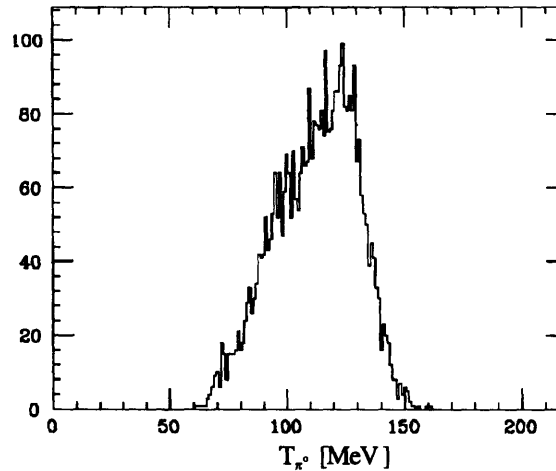


Figure 3.9: A typical kinetic energy spectrum for a data run, in this case Helium SCX. The influence of the triangularly shaped acceptance is clear.

The spectrometer's acceptance as a function of kinetic energy is triangularly shaped and peaked at the energy corresponding to the nominal opening angle when  $X=0$ . The energy spectrum of the data is affected by this shape (illustrated in figure 3.9). Similarly, the

acceptance as a function of scattering angle is also triangularly shaped and peaked about the spectrometer's central scattering angle. The range of the angular acceptance is determined by the angular range of the fiducial regions designated for both arms.

The laboratory scattering angle of the  $\pi^0$ ,  $\theta_{\pi^0}$ , is calculated by:

$$\cos\theta_{\pi^0} = \frac{E_1 \cos\theta_1 + E_2 \cos\theta_2}{\sqrt{E_1^2 + E_2^2 + 2E_1E_2 \cos\eta}}, \quad (3-10)$$

where  $\theta_i$  is the laboratory angle between the  $i$ th photon and the beam direction. To be consistent with the scattering angle binning of the  $\pi^0$  yield detected in the spectrometer, the acceptance is also calculated for three  $10^\circ$  bins. This does not require, however, that each photon be detected in the middle bins of both crates for a  $\pi^0$  to be from the middle  $10^\circ$  bin. One photon may be detected in the smaller scattering angle side bin of one crate, and the other photon in the larger scattering angle side bin of the other crate so that the reconstructed  $\pi^0$  scattering angle is in the center bin.

On the other hand,  $\pi^0$ s whose scattering angle is computed to be from the side bins most likely resulted from photons being detected in those bins. As a result, the acceptance of the center bin is typically twice as great as those for the side bins, which are about equal (figure 3.10).

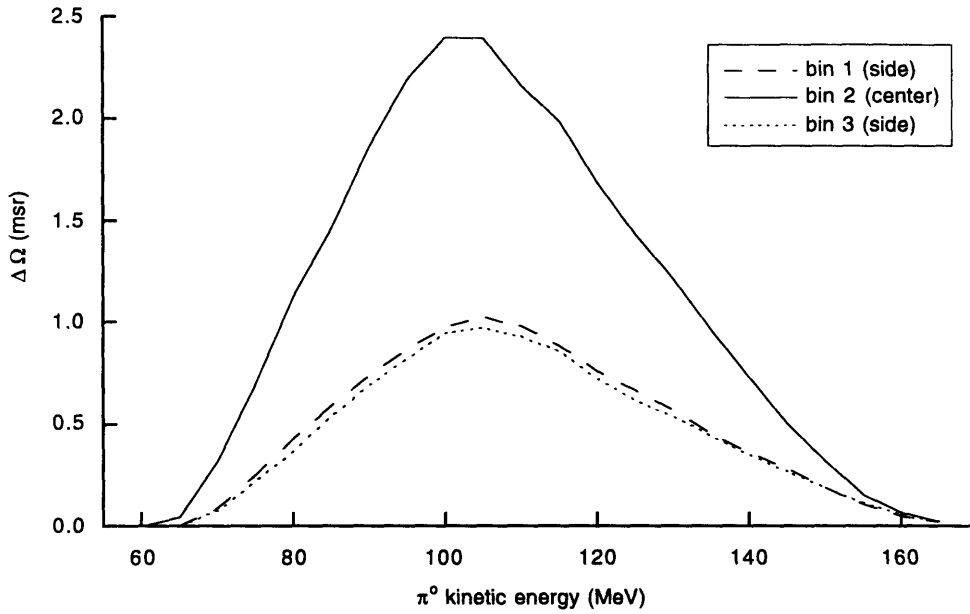


Figure 3.10: The acceptance for detecting  $\pi^0$ s for the spectrometer is binned in three  $10^\circ$  bins, with bin 1 being most forward in angle. The acceptance of the middle bin, centered at the spectrometer's nominal scattering angle, is roughly twice as great as that for either of the side bins. These curves were calculated for a slab target and no material between the target and the spectrometer crates for an opening angle of  $\eta = 70^\circ$ , setup B and for an XCUT = 25%.

Since the middle bin is centered at the spectrometer's nominal scattering angle, that angle is also the mean scattering angle for the bin as well. The widths of the acceptances as a function of angle for  $\pi^0$ s of different kinetic energies differ, however, and must be taken into account. The bins to either side of the center bin must be weighted by the individual acceptances for the range of  $\pi^0$  energies detectable. As a result, the mean scattering angles are shifted from the center of the side bins towards the spectrometer central angle typically by  $\Delta\theta_{\text{side}} = 1^\circ - 2^\circ$ . The mean scattering angles for the side bins of  $\eta = 95^\circ$  and  $\eta = 70^\circ$  setups at the same nominal spectrometer angle differed slightly by  $\Delta\theta_{\text{side}}(\eta = 95^\circ, \eta = 70^\circ) = 0.4^\circ - 0.7^\circ$  due to the differences in radial distances between the targets and crates. As this difference is quite small compared to the  $10^\circ$  width of the bin, the data from corresponding bins are presented together in the following chapter.

Both the shape and the magnitude of the  $\pi^0$  yield are altered when the effects of the



---

acceptance are included in the calculation of the cross section, and this effect amounts to one of the more significant corrections to the data. In addition to the geometrical probability for detecting photons from  $\pi^0$  decay, all additional conditions such as the XCUT limit and designation of fiducial regions are included in the calculation of  $\Delta\Omega$ .

### 3.4.1 Photon Attenuation Losses

Since the detection of a  $\pi^0$  requires the detection of the two photons resulting from its decay, any material which may absorb photons on their way to the spectrometer must be taken into account. A major contributor to this process is the material from the bulky cryogenic target and its support structures, and the correction to the acceptance due to these objects is detailed below. Other materials in which photons could be absorbed include the Helium, Carbon, and  $\text{CH}_2$  targets themselves or the air between the target and the spectrometer crates. The effects of absorption in solid targets such as  $\text{CH}_2$  and  $^{12}\text{C}$  have been estimated to be less than 1%<sup>2</sup>, and the effect for the liquid Helium target is smaller due to its smaller absorption cross section and lesser target density. As the contributions from other areas to the total error of the cross sections are much greater, the effects from absorption of photons within the target have been ignored in this analysis.

Photons may also be absorbed in the air between the target and the spectrometer. There is, however, a convenient mechanism to account for this effect. The probability for absorption is related to the distances between the target and the spectrometer crates, and to a very good approximation, this probability is equal for all spectrometer setups used during the experiment. The effects of photon absorption in the air can then be considered to be accounted for in the determination of the spectrometer conversion efficiency.

PIANG needed to be modified substantially to reflect the physical setup of our experiment. Due to the cryostat assembly and its support stand, the paths between the target cell and the  $\pi^0$  spectrometer crates were blocked by nickel, aluminum, and/or iron. As the thickness

of the obstructing material ranged from several mils to a couple of inches depending on the particular path, the geometrical acceptance was attenuated by a few percent to sixty percent. This effect was accounted for by modifying PIANG to correct the acceptance function as if there were an additional loss of detection efficiency.

The modifications made are based on modifications made<sup>53,54</sup> for the “Virginia” <sup>3,4</sup>He cryogenic target when it was previously used with the  $\pi^0$  spectrometer. First, all objects between the target cell and the spectrometer were geometrically categorized as either cylinders, rings, domes, or walls. Their dimensions, laboratory coordinates, and composition were then incorporated into PIANG. Each photon created in the Monte Carlo simulation was individually tracked to see whether its path intersected any object. If so, PIANG calculated the total thicknesses of nickel, aluminum, or iron traversed before detection.

To save computer time, one simplification<sup>54</sup> was made which does not compromise the accuracy of the Monte Carlo simulation. Rather than absorbing photons or allowing them to pass unimpeded as is the physical process, each photon was given a fractional value based on its probability for transmission. When calculating the acceptance function based on the number of successfully detected photons for any given spectrometer setup, these transmission probabilities weighted the probability for detection. This method should produce results identical to those of any calculation employing a more realistic model of photon absorption. Whereas the individual destinies of photons may differ, their probabilities for transmission are equal so long as the thicknesses and types of materials traversed remain constant. In the limit of many photon events, the sum of these transmission probabilities for every photon should equal the sum of only those which avoid absorption. In addition, the Monte Carlo simulation was always run long enough to make statistical uncertainties negligible.

The probability that a photon survives through a distance,  $d$ , of material is given by  $e^{-\mu\rho d}$  where  $\mu$  is the photo-absorption coefficient and  $\rho$  the density of that material. Given the similarity in numbers of protons and neutrons in nickel and iron, the photo-absorption

coefficient for nickel was assumed to be identical to that for iron. The small energy dependences of these coefficients were taken into account by fitting the literature values<sup>55</sup> with a linear energy dependence for iron and nickel, and a quadratic form for aluminum as follows:

$$\mu_{\text{Fe}}(E_\gamma) = 0.033 + 7 \times 10^{-5} E_\gamma \quad (3-11)$$

$$\mu_{\text{Al}}(E_\gamma) = 0.0206 + 5.989 \times 10^{-5} E_\gamma - 0.123 \times 10^{-6} E_\gamma^2 \quad (3-12)$$

where  $E_\gamma$  is the photon energy in MeV, and the coefficient is in units of  $\text{cm}^2 / \text{gm}$ .

The results of the modifications to PIANG are shown in figure 3.11. The solid angles for the spectrometer in both the  $\eta = 70^\circ$  and  $\eta = 95^\circ$  setups have been displayed for both configurations of the cryogenic target, with the nickel vacuum vessel and with the modified vessel featuring mylar windows. The solid angles are also displayed without the effects of photon attenuation. At  $\eta = 70^\circ$ , the solid angle of the cryostat with the nickel vacuum vessel is only attenuated by about 10%, as the path of the  $\pi^0$  decay photons avoids all bulky target support structures. This is not the case with the vacuum vessel featuring mylar windows, where the support structures were closer to the beam and greatly affected the solid angle at  $\eta = 70^\circ$ .

At  $\eta = 95^\circ$ , the magnitudes of the attenuation between the nickel and mylar vessels is reversed. With the larger opening angle, the support structures for the target configured with the nickel vessel blocked the upper spectrometer crate, decreasing the solid angle dramatically. The solid angle is not blocked as heavily, however, with the vessel with mylar windows, as there was an gap between two support plate which allowed photons to pass unobstructed. This fortuitous gain in solid angle, however, proved difficult to model in PIANG and affected the selection of the data set as discussed in chapter 4.

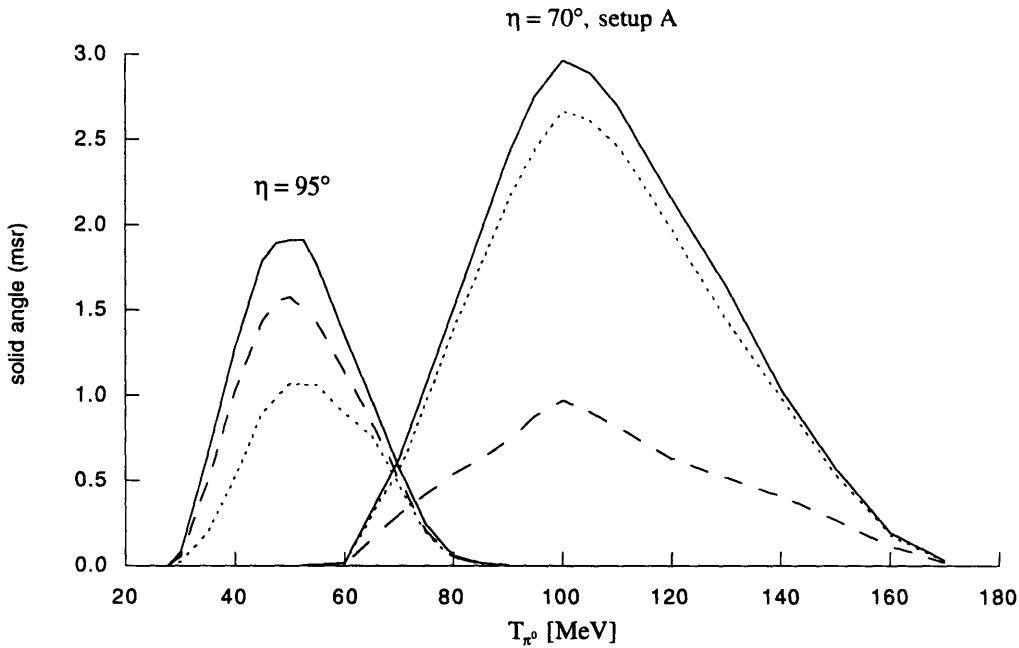


Figure 3.11: Solid angles of the spectrometer at both the  $\eta = 70^\circ$  (setup A) and  $\eta = 95^\circ$  setups. The solid angles without the presence of a cryogenic target is shown as the solid lines. Photon attenuation in the cryogenic target material decreases the solid angle in both target configurations, with the nickel vacuum vessel (dotted line) and the modified vacuum vessel featuring mylar windows (dashed line).

### 3.5 Conversion Efficiencies

The second part of the detector efficiency, apart from the wire chamber efficiency, is the conversion efficiency  $\epsilon_{\text{conv}}$ . As designed, each Pb-glass converter is about 30% efficient in converting a photon to an  $e^+e^-$  pair which can be detected by the scintillators and the other elements of the spectrometer. This value is described by the empirical formula<sup>56,57</sup> for the conversion efficiency  $\epsilon_{\text{cp}}$  of a photon of energy  $E_\gamma$  in MeV,

$$\epsilon_{\text{cp}} = 0.28 + 0.1 \cdot \log_{10} \left( \frac{E_\gamma}{100 \text{ MeV}} \right). \quad (3-13)$$

The theoretical limit for the conversion efficiency for the three converter planes in both arms based on these design specifications is just over 40% as described by

$$\epsilon_{\text{conv.}} = \left[ 1 - (1 - \epsilon_{\text{cp}})^3 \right]^2. \quad (3-14)$$

The value of the conversion efficiency of the spectrometer was determined through measuring single charge exchange from the free proton,  $p(\pi^-, \pi^0)n$ , a process with a well-known cross section.

A  $\text{CH}_2$  target was used to provide the free proton targets, and the background contributions from the Carbon were measured using a separate  $^{12}\text{C}$  target. The conversion efficiency was measured with an opening angle of  $\eta = 70^\circ$  at four of the five scattering angles used to measure SCX from Helium,  $50^\circ$ ,  $80^\circ$ ,  $105^\circ$ , and  $130^\circ$ . At  $80^\circ$  and  $105^\circ$ , measurements were made with the spectrometer in both setup A and setup B. Only setup A was measured at  $50^\circ$ , and only setup B was measured at  $130^\circ$ . In total, six pairs of  $\text{CH}_2$  and Carbon data were taken to determine the conversion efficiency of the spectrometer. As the data at each scattering angle are grouped into three angular bins, eighteen data points were used to determine the conversion efficiency.

Since the normalization measurements were only made with the incident beam energy of 160 MeV, a measurement with  $\eta = 70^\circ$  at the fifth angle  $30^\circ$  could not be made because the SCX peak is at the upper energy limit of the spectrometer's acceptance for detecting  $\pi^0$ s. Similarly, measurements could not be made at any of the scattering angles for the  $\eta = 95^\circ$  setup because the acceptance covers energies lower than the SCX peak. If the incident beam energy had been lowered, these additional measurements would have been possible.

The first step in analyzing the  $\text{CH}_2$  and Carbon data is to determine a doubly differential cross section for each target using equation (3-1) assuming the conversion efficiency  $\epsilon_{\text{conv.}} = 100\%$ . Apart from this one important difference, the same procedures were used as with the Helium data and their background measurements. Because the  $\pi^- p \rightarrow \pi^0 n$  reaction is a two-body reaction, the  $\pi^0$  kinetic energy is uniquely determined by its

scattering angle, and an integral over the spread in  $\pi^0$  energies must be made before a comparison can be made with the known singly differential cross section. The yield from the proton is calculated as the difference of the two yields as follows:

$$\left(\frac{d\sigma}{d\Omega}\right)_{\text{exp}}^{\text{H}} = \frac{1}{2} \left[ \left(\frac{d\sigma}{d\Omega}\right)_{\text{exp}}^{\text{CH}_2} - \left(\frac{d\sigma}{d\Omega}\right)_{\text{exp}}^{^{12}\text{C}} \right] \quad (3-15)$$

where the  $\frac{1}{2}$  accounts for the two free protons in  $\text{CH}_2$  (see figure 3.12).

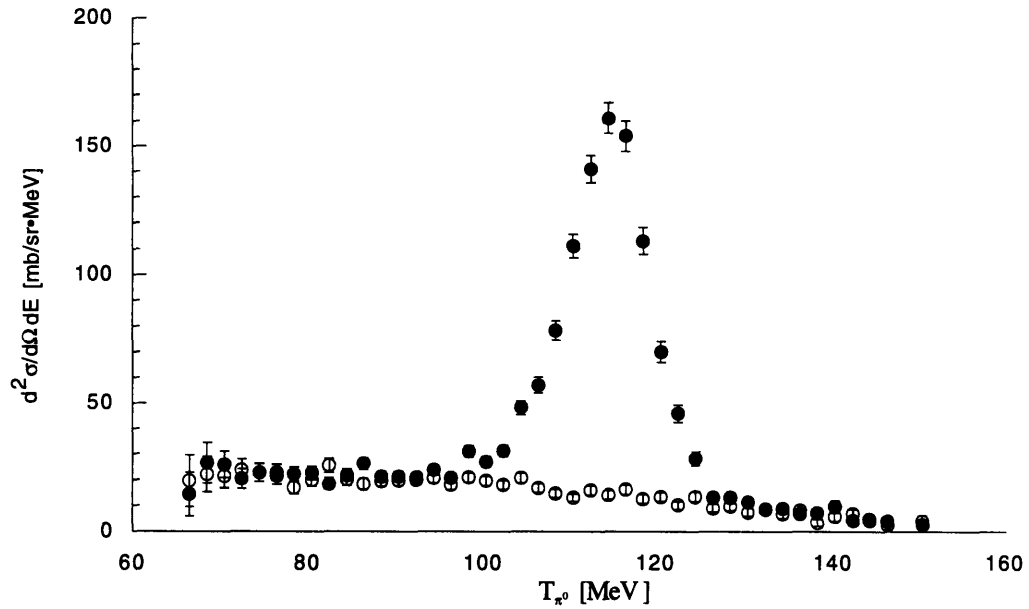


Figure 3.12: The  $\pi^0$  energy spectra from  $\text{CH}_2$  (closed circles) and  $^{12}\text{C}$  (open circles) targets at  $80^\circ$ . The peak is integrated and compared with the known cross section for  $\pi^- p \rightarrow \pi^0 n$  to determine the spectrometer conversion efficiency.

The ratio of the experimental cross section from the proton to the known  $\pi^- p \rightarrow \pi^0 n$  cross section,

$$\epsilon_{\text{conv.}} = \frac{\left(\frac{d\sigma}{d\Omega}\right)_{\text{exp}}^{\text{H}}}{\left(\frac{d\sigma}{d\Omega}\right)_{\text{SAID}}^{\text{H}}}, \quad (3-16)$$

is taken to be equal to the conversion efficiency. Differential cross sections for this reaction were obtained by using the program SAID<sup>88</sup> which calculates pion-nucleon cross sections by fitting phase shifts for each partial wave to experimental data. The values used in our calculation were based on solution SM90<sup>89</sup> from this analysis.

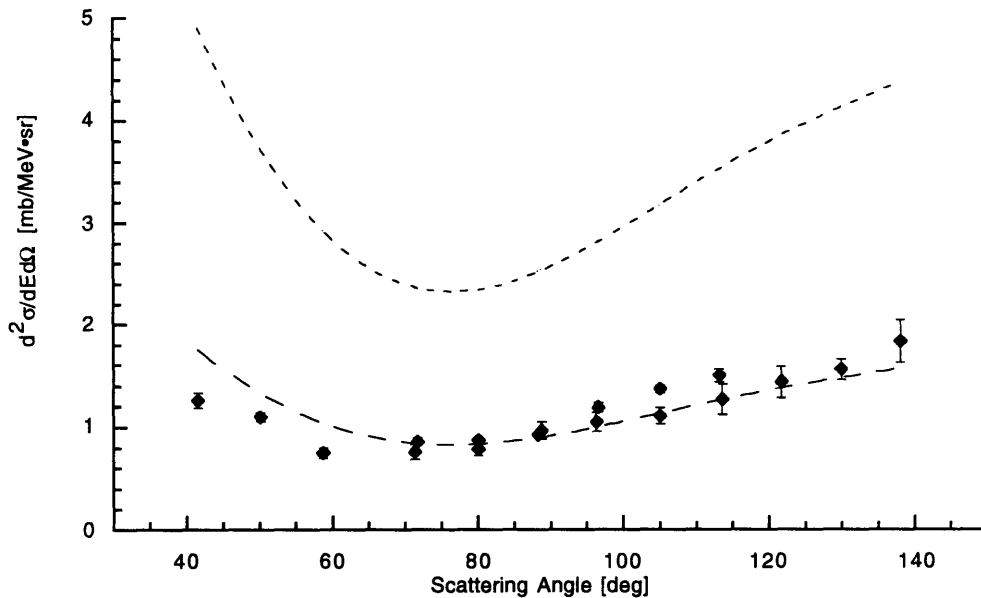


Figure 3.13: The proton yields from the normalization measurements (solid diamonds) are shown with the differential cross section for SCX from the free proton (upper dashed curve) as calculated by SAID. The free proton results are fit to the data (lower dashed curve) to yield a ratio 0.355, the conversion efficiency for the experiment.

The proton yields for our normalization measurements and the differential cross section for SCX from the free proton as calculated by SAID are displayed in figure 3.13. The SAID results were fit to the data to determine the ratio, i.e., the conversion efficiency, which was found to be  $\epsilon_{\text{conv.}} = 0.355$ . The ratios between the proton yields and SAID results are shown as a function of quasifree  $\pi^0$  energy in figure 3.14. These ratios are the

conversion efficiencies for the six pairs of runs or eighteen data points used to determine this value.

A large amount of time was spent during the analysis process on the determination of the value of the conversion efficiency. First,  $\epsilon_{\text{conv}}$  should be nearly flat or slowly increasing as a function of energy, as determined by equations 3-13 and 3-14. This disagrees with the trend of our measurements, shown to decrease slowly with increasing energy in figure 3.14. At the lower energies, the ratio is also somewhat high, compared with previous experiments involving the spectrometer and the theoretical maximum. Finally, the disagreement between measurements made with setup A and setup B at 96 MeV is a cause for concern.

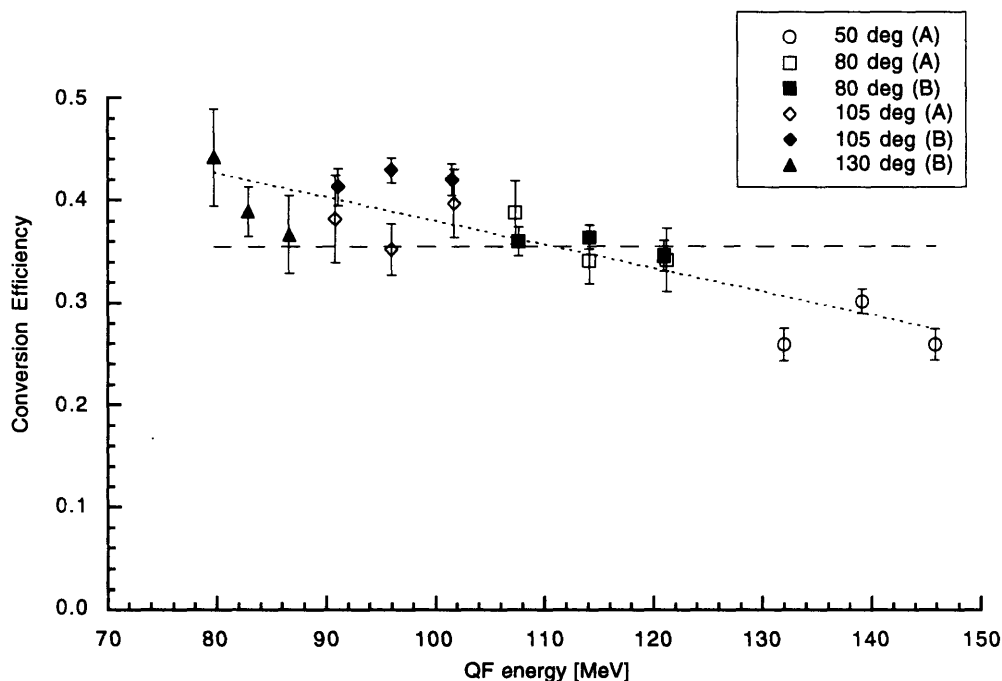


Figure 3.14: The ratio between the proton yields and the SAID results for the eighteen data points used to determine the conversion efficiency of 0.355 (dashed horizontal line). The data were taken with  $\eta = 70^\circ$  at four spectrometer angles whose plotting symbols are shown in the legend. The measurements using setup A are displayed with clear plotting symbols, and those using setup B are displayed using solid plotting symbols. The data were analyzed with  $\text{XCUT}=0.25$ . A linear fit was also made to the data (dotted line) and the equation was found to be  $y = 0.612 - 2.31 \times 10^{-3} \cdot x$ , where  $y$  is the conversion efficiency and  $x$  is the  $\pi^0$  energy in MeV.



---

These problems with the conversion efficiencies are believed to be related primarily to uncertainties in the phototube energy calibration and their effects upon the XCUT test. The quasifree energies of the free proton SCX reaction varied over a range in energies in these measurements. As shown in section 3.3, the X-distributions of  $\pi^0$ s of varying energies change dramatically over the acceptance of the spectrometer in its  $\eta = 70^\circ$  configuration. Inaccuracies in the energy measurements may change these distributions, with XCUT changing the measured  $\pi^0$  yield, which directly affects the conversion efficiencies. In addition, having the quasifree peak swept across the entire energy range of the spectrometer acceptance introduces the question of the accuracy with which the acceptance can be calculated, particularly at the wings away from the peak.

For comparison, the conversion efficiencies calculated with the identical analysis but with XCUT=0.5 is shown in figure 3.15. A horizontal line fitted to the data determined the conversion efficiency to be 0.347, nearly the same value as with XCUT=0.25. There is somewhat better agreement between the data sets at 96 MeV, but there has developed an inconsistency between data taken with setup A and setup B at 114 MeV. In addition, the decreasing energy dependence of the conversion efficiency still exists. The highest energy data measured at  $50^\circ$  are slightly closer to the average but are still in poor agreement given their higher statistics gained by increasing XCUT. Given these considerations, XCUT was chosen to remain at 0.25 for the calculation of the conversion efficiencies and the analysis of the  $^4\text{He}$  data.

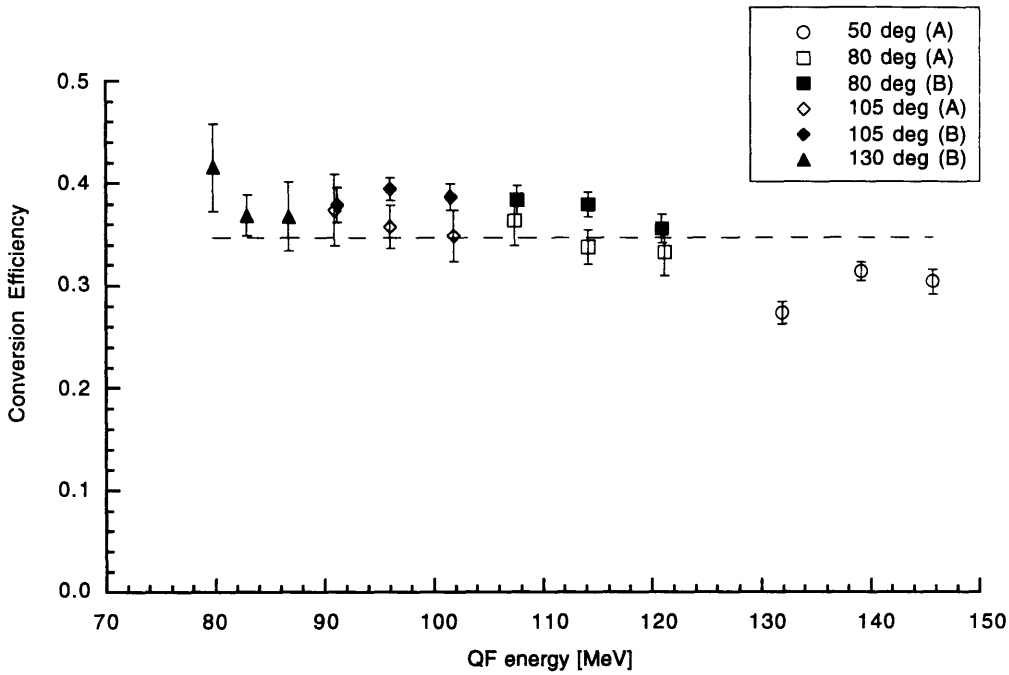


Figure 3.15: Conversion efficiencies calculated as above, but with XCUT=0.50. The dashed line is a horizontal fit to the data determining the conversion efficiency to be 0.347.

In the end, the conversion efficiency was taken to be  $\epsilon_{\text{conv.}} = 0.355$  for all spectrometer setups (both opening angles and all five scattering angles). As can be seen in the following chapter, the good agreement between the magnitudes of the  $\eta = 70^\circ$  and  $\eta = 95^\circ$  doubly-differential cross section at  $T_{\pi^0} = 70 - 75$  MeV supports this decision. For completeness, the SCX data taken with  $\eta = 70^\circ$  were also analyzed with an energy-dependent conversion efficiency determined by fitting a decreasing linear dependence to the conversion efficiency data shown in figure 3.14. The equation of the line was found to be

$$y = 0.612 - 2.31 \times 10^{-3} \cdot x, \quad (3-17)$$

where  $y$  is the conversion efficiency and  $x$  is the  $\pi^0$  energy. These data are plotted along with those analyzed with the constant  $\epsilon_{\text{conv.}} = 0.355$  in the following chapter.

---

Other experiments<sup>52,37</sup> have chosen to evaluate the conversion efficiency with both the numerator and the denominator averaged across the angular acceptance of the spectrometer weighted by the known differential cross section. This procedure reduces any error due to the combination of the large physical size of the spectrometer, the changing differential cross section across the scattering angular acceptance, and the strong energy dependence of the spectrometer's acceptance. In those experiments, however, the data were averaged over a single  $24^\circ$  bin, much larger than the  $10^\circ$  bins chosen for this experiment. To make certain the problems in determining the conversion efficiencies in this measurement are not the result of the choice of bin size, the conversion efficiencies for the center  $10^\circ$  bin were compared with those calculated from its subdivision into four  $2.5^\circ$  bins, and the results were consistent for both bin sizes. As other errors included in this measurement outweigh any gain possible from this refinement, the method of evaluating the conversion efficiency as in other experiments (by averaging the angular acceptance) was not used in this analysis.

### 3.6 Determination of Systematic Errors

There are two main sources of systematic errors in this measurement. The calibration of the ionization chamber derived from the activation procedures is accurate to the precision of the  $^{12}\text{C}(\pi^-, \pi^-)^{11}\text{C}$  cross section which is known to 3-5%<sup>39,40</sup>. The conversion efficiency for our measurement is not thought to be known better than 20%; since the calculation of the conversion efficiency involves use of the Monte Carlo simulation PIANG, the uncertainties associated with those results are considered to be included in this value. The uncertainty in the Monte Carlo results has been previously reported as 20%<sup>51</sup>. Other systematic uncertainties such as those arising from the determination of the target thicknesses, live time, statistical fluctuations in the Monte Carlo results, and calculation of the wire chamber efficiencies are estimated at 1% each. The accuracy of the SAID results is also claimed to be about 1%<sup>38,39</sup>.



## Chapter 4: Experimental Results

The results of the experiment to measure inclusive SCX on  ${}^4\text{He}$  are presented in this chapter. The  $\pi^0$  spectra will be shown as doubly-differential cross sections in the laboratory frame,  $d^2\sigma/dE_{\pi^0}d\Omega_{\text{lab}}$ . These spectra have been integrated over outgoing  $\pi^0$  energy to yield the singly-differential cross section,  $d\sigma/d\Omega_{\text{lab}}$ , also known as the angular distribution. Finally, the total cross section,  $\sigma$ , has been obtained by integrating the angular distribution over the entire  $4\pi$  steradian solid angle. The angular distribution for the  $p(\pi^-, \pi^0)n$  reaction has been fit at backward scattering angles to the  ${}^4\text{He}(\pi^-, \pi^0)X$  data to determine  $N_{\text{eff}}$ , a measure of the effective number of nucleons involved in the reaction. Finally, the effects of Pauli blocking have been determined through comparison with the free proton SCX cross section normalized by  $N_{\text{eff}}$ .

### 4.1 Presentation of the Data

The use of two different vacuum vessels for the cryostat divided the data set into two parts midway through the experiment and requires comment. Also, the use of dummy replicas for the target cell in addition to the evacuated “dry” cell provided two measures of the background processes for each of the setups. Several “different” measurements of the  ${}^4\text{He}(\pi^-, \pi^0)X$  reaction are then possible through pairing different combinations of vacuum vessels and background target cells. While each measurement should yield exactly the same cross sections as that of a different combination, the systematic errors involved, most notably due to the accuracy with which the experimental setup could be modeled in PIANG, are clearly not equal. A choice has been made to present a subset of the data which minimized these uncertainties.

The selection of the presented data set was made for the five nominal spectrometer scattering angles and for the two opening angles employed. The combinations of vacuum vessels and background cells used are summarized in table 4.1.

Opening angle: $\eta = 70^\circ$				
$\theta = 30^\circ$	$\theta = 50^\circ$	$\theta = 80^\circ$	$\theta = 105^\circ$	$\theta = 130^\circ$
<b>nickel-dummy (A)</b>	<b>nickel-dummy (A)</b> mylar-dry (B) mylar-dummy (B)	<b>nickel-dummy (A)</b> mylar-dry (B) mylar-dummy (B)	<b>nickel-dummy (A)</b>	<b>nickel-dummy (B)</b> mylar-dry (B)
Opening angle: $\eta = 95^\circ$				
$\theta = 30^\circ$	$\theta = 50^\circ$	$\theta = 80^\circ$	$\theta = 105^\circ$	$\theta = 130^\circ$
<b>mylar-dry</b> mylar-dummy	<b>mylar-dry</b> mylar-dummy	<b>nickel-dry</b> nickel-dummy mylar-dummy	<b>nickel-dummy</b>	<b>nickel-dry</b> nickel-dummy

Table 4.1: Summary of the combinations of vacuum vessels and background target cells used during the experiment. For the helium foreground measurement, “nickel” refers to the cryostat having the electroplated nickel vessel used during the first half of the experiment, and “mylar” refers to the vessel which replaced it featuring mylar windows for the charged pion beam. For the measurement of background processes, “dummy” refers to the use of a replica of the target cell rather than an evacuated cell, which is labelled “dry.” For the  $\eta = 70^\circ$  measurements, the spectrometer configurations of setup A and setup B are also indicated. The presented data come from the combination which is boldfaced. An explanation for this selection is in the body of the text.

At all scattering angles, the high-energy part of the spectra, as measured with the smaller opening angle  $\eta = 70^\circ$ , is presented from a pairing of foreground measurements taken with the nickel vacuum vessel and background processes measured with its associated dummy target cell. The support structures for the nickel vessel are several feet above the interaction region in this setup and do not block the path between it and the spectrometer crates. The PIANG correction for the small amount of material in the cell walls is correspondingly small, and the systematic uncertainties are minimized by selecting this pairing. This would not be the case with data taken with the mylar vacuum vessel.

For the larger  $\eta = 95^\circ$  opening angle, the preference is also to present data taken with the nickel vacuum vessel, though with this setup the upper crate is partially blocked by the

support structures. The simplicity of the nickel vessel design, compared with the complexity of the mylar vessel, meant that modeling its geometry could be done more accurately, and uncertainties related to this accuracy are lessened. At  $\theta = 80^\circ$  and  $130^\circ$ , the foreground data taken with the nickel vessel are paired with background runs taken when the cell was dry, rather than with the dummy target, to eliminate any uncertainties associated with modeling two different setups. Similarly, at  $\theta = 30^\circ$  and  $50^\circ$ , where there were no data taken with the nickel vessel, data taken with the mylar vessel are paired with background runs taken when the cell was dry.

## 4.2 Doubly-Differential Cross Sections

The spectrometer was set up at five nominal scattering angles,  $\theta_s = 30^\circ, 50^\circ, 80^\circ, 105^\circ,$  and  $130^\circ$ . At each setup, the  $\pi^0$  data were binned in three  $10^\circ$  bins,  $\theta_1 = \theta_s - 10^\circ \pm 5^\circ$ ,  $\theta_2 = \theta_s \pm 5^\circ$ , and  $\theta_3 = \theta_s + 10^\circ \pm 5^\circ$ , so that the scattering angle for the center bin is equal to the nominal angle for the spectrometer, i.e.,  $\theta_2^{\text{nom.}} = \theta_s$ . The scattering angles for the two side bins are computed by averaging the scattering angles weighted by the angular acceptances of the bins, as calculated by PIANG, over the energy range of that bin. These angles are shifted towards the center bin where the acceptance is greatest, rather than being exactly  $10^\circ$  apart, and were typically  $\theta_1^{\text{nom.}} = \theta_s - 8^\circ$  and  $\theta_3^{\text{nom.}} = \theta_s + 8^\circ$ . The three doubly-differential cross sections from each bin are presented for each nominal scattering angle in figures 4.1 to 4.5.

Each spectrum is composed of data taken with two opening angle settings of the spectrometer. The high-energy part of the spectrum for  $T_{\pi^0} = 70 - 160$  MeV was measured with  $\eta = 70^\circ$ . The low energy part of the spectrum for  $T_{\pi^0} = 35 - 75$  MeV was measured with  $\eta = 95^\circ$ . Due to the overlap of the acceptances for both opening angles, data exist from both setups at 70 MeV and 75 MeV. They were in good agreement for all scattering angles. This indicated that the conversion efficiency of the spectrometer is largely independent of spectrometer opening angle, and it supports the decision to use a common value for the

conversion efficiency for the entire data set. Both data at 70 MeV and 75 MeV are presented in figures 4.1 to 4.5.

As discussed in Chapter 3, the data were analyzed with a conversion efficiency of 0.355, independent of  $\pi^0$  energy. The data taken with  $\eta = 70^\circ$  were also calculated with an energy dependent conversion efficiency of the form

$$y = 0.612 - 2.31 \times 10^{-3} \cdot x, \quad (4-1)$$

where  $y$  is the conversion efficiency and  $x$  is the  $\pi^0$  energy, and those results are shown as well. At the highest energies, where the energy dependent conversion efficiency is much lower than 0.355, the individual data points do not increase by more than one standard deviation. At energies below 100 MeV, where the energy dependent conversion efficiency is higher than 0.355, the data points decrease noticeably since the cross section is larger, though they still do not change by more than one standard deviation. The data at 70 MeV and 75 MeV also do not agree as well as with the constant conversion efficiency.

The data are presented in 5 MeV bins from 35 MeV to about 160 MeV, the upper limit for the energy acceptance of the  $\pi^0$  spectrometer in the  $\eta = 70^\circ$  setup. The acceptance thus extends beyond the kinematic limit for the SCX reaction on  $^4\text{He}$ . Higher energy  $\pi^0$ s can be created, however, through SCX in heavier nuclei, such as in the air or target cell walls, and contributed to a measurement of higher energy  $\pi^0$  yields in both the Helium foreground and (dummy or dry) background runs. In the measurement of the Helium SCX cross sections, the net yield above the limit was consistent with zero, an indication that the background subtraction was done correctly.

The shapes of the cross sections are similar to those from heavier nuclei (see chapter 1) in that they feature a large quasifree peak, indicative of scattering from a single bound nucleon. For comparison, the energy corresponding to free  $\pi\text{N}$  kinematics is indicated by an arrow in figures 4.1 to 4.5. At forward scattering angles, the positions of the peaks are



at energies lower than for free  $\pi N$  kinematics due to the strong suppression of the cross section by Pauli blocking. This effect vanishes at backward scattering angles, where the positions of the peaks are in better agreement with the free  $\pi N$  kinematics. Finally, the spectra display a long low-energy tail, the region in which we would search for indications of multiple-scattering effects in this reaction. An analysis of the quasifree peaks is presented in chapter 5 as is a discussion of the tail of the spectra in the comparison of the data with those for inelastic scattering and with theoretical calculations.

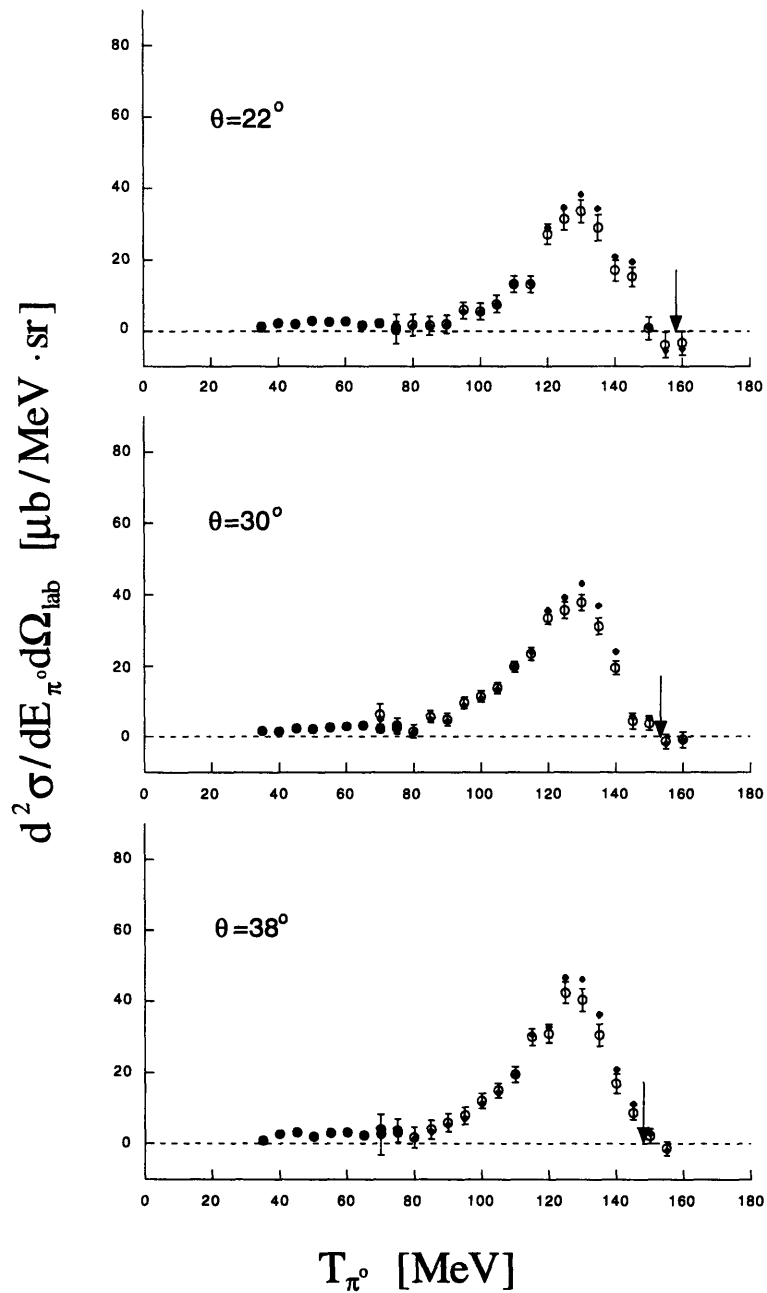


Figure 4.1: Doubly-differential cross sections for the reaction  ${}^4\text{He}(\pi^-, \pi^0)\text{X}$  at an incident energy of 160 MeV. The lower energy data (solid circles) were taken with  $\eta = 95^\circ$ , and the higher energy data were taken with  $\eta = 70^\circ$  in setup A. The solid diamonds are the  $\eta = 70^\circ$  data determined using the energy dependent conversion efficiency (the error bars are similar to those for the corresponding data and have been omitted for clarity). The data were taken at the nominal spectrometer scattering angle of  $30^\circ$ . The arrow indicates the energy corresponding to free  $\pi\text{N}$  kinematics. Bars on the points indicate the uncertainty from statistical fluctuations only.

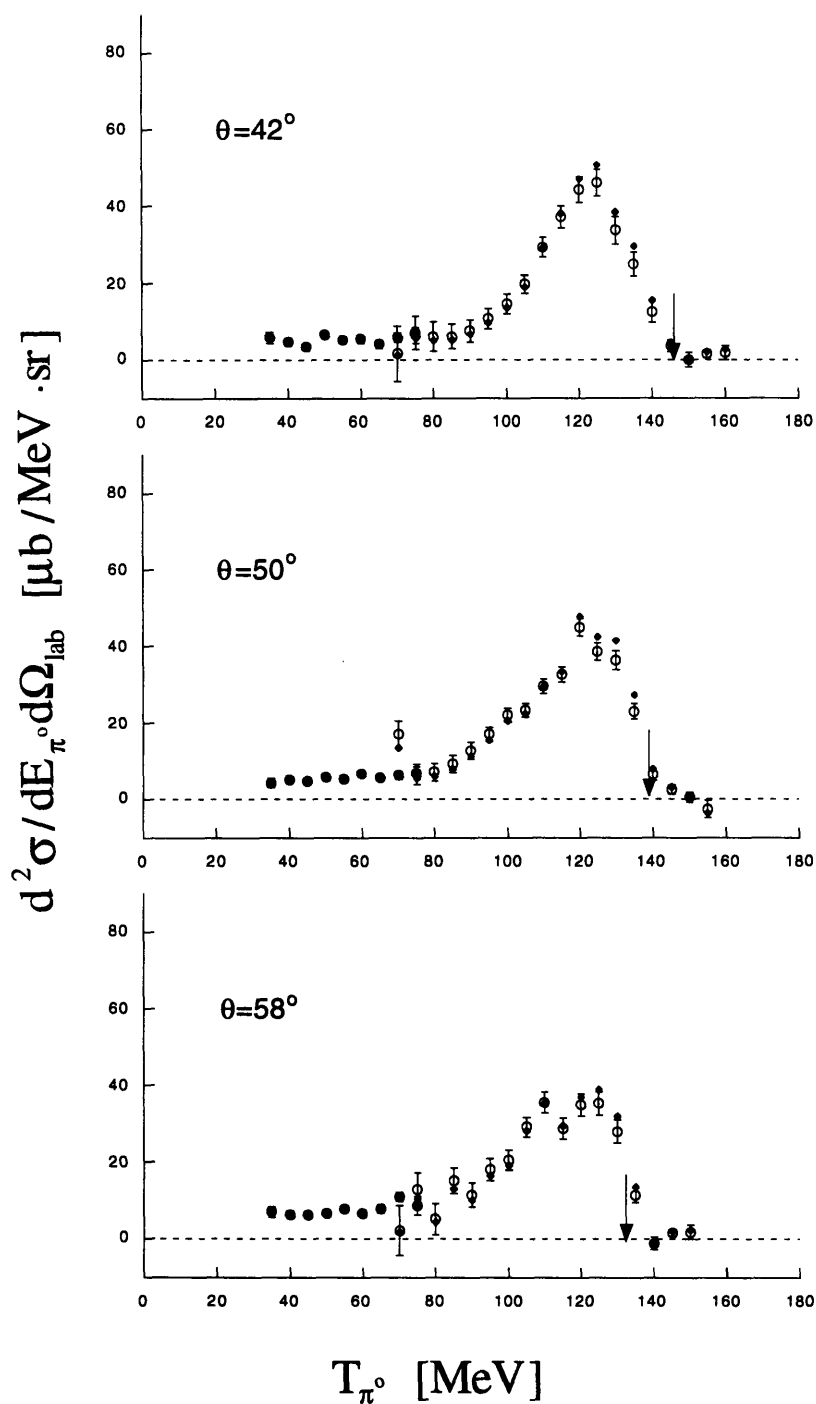


Figure 4.2: Doubly-differential cross sections for the reaction  ${}^4\text{He}(\pi^-, \pi^0)\text{X}$  at an incident energy of 160 MeV. The data above were taken at the nominal spectrometer scattering angle of  $50^\circ$ . For the  $\eta = 70^\circ$  measurement, the spectrometer configuration was setup A. The plotting symbols, arrows, and uncertainty bars are as in figure 4.1.

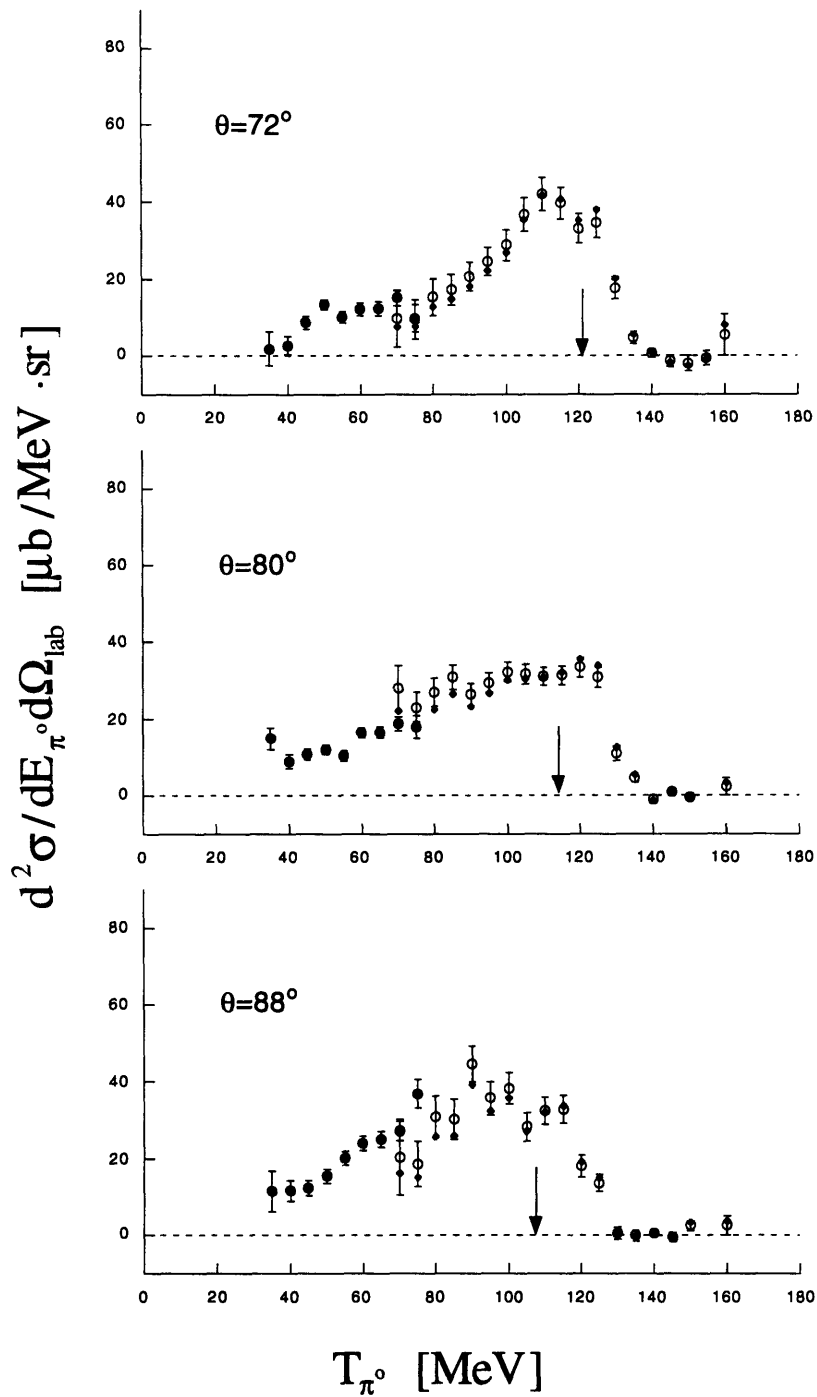


Figure 4.3: Doubly-differential cross sections for the reaction  ${}^4\text{He}(\pi^-, \pi^0)\text{X}$  at an incident energy of 160 MeV. The data above were taken at the nominal spectrometer scattering angle of  $80^\circ$ . For the  $\eta = 70^\circ$  measurement, the spectrometer configuration was setup A. The plotting symbols, arrows, and uncertainty bars are as in figure .

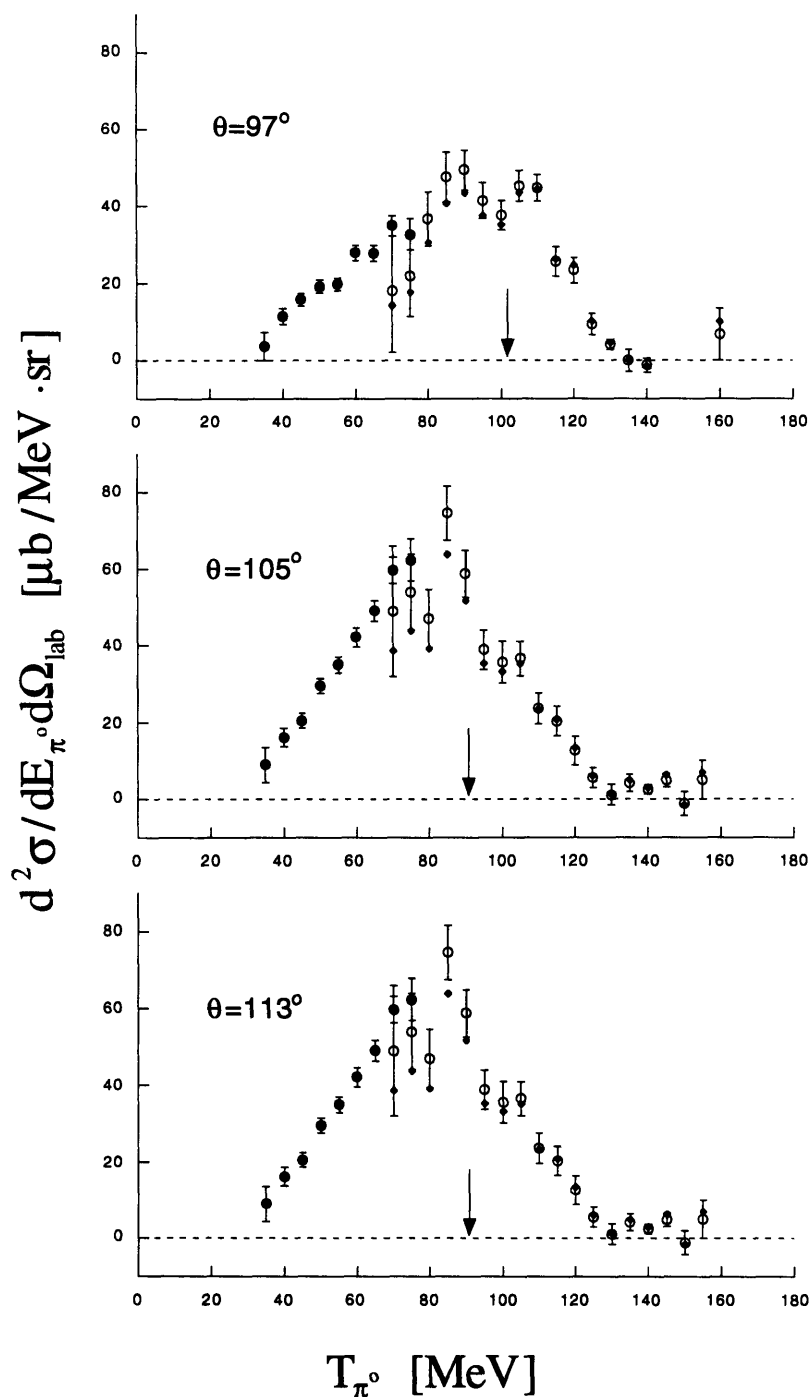


Figure 4.4: Doubly-differential cross sections for the reaction  ${}^4\text{He}(\pi^-, \pi^0)\text{X}$  at an incident energy of 160 MeV. The data above were taken at the nominal spectrometer scattering angle of  $105^\circ$ . For the  $\eta = 70^\circ$  measurement, the spectrometer configuration was setup A. The plotting symbols, arrows, and uncertainty bars are as in figure 4.1.

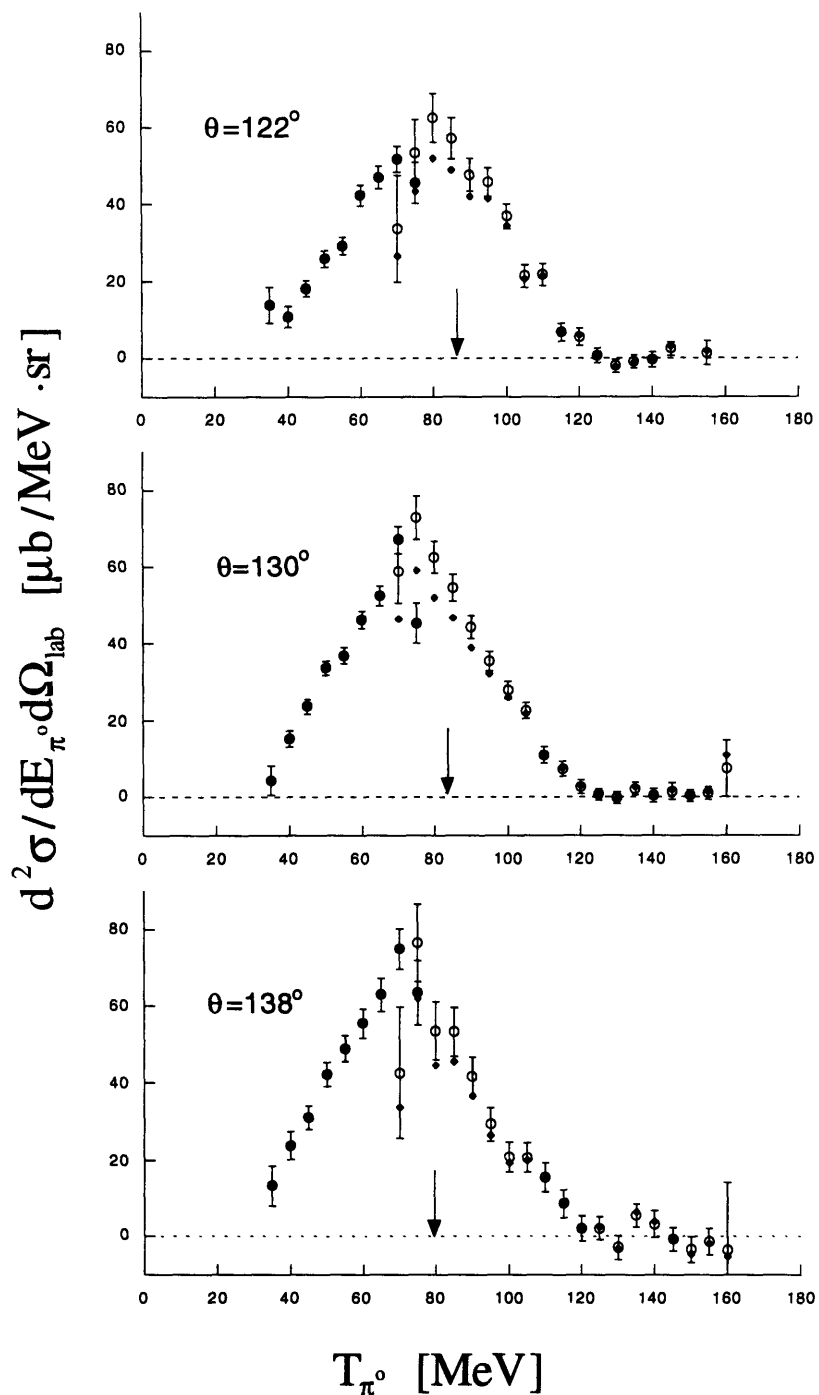


Figure 4.5: Doubly-differential cross sections for the reaction  ${}^4\text{He}(\pi^-, \pi^0)\text{X}$  at an incident energy of 160 MeV. The data above were taken at the nominal spectrometer scattering angle of  $130^\circ$ . For the  $\eta = 70^\circ$  measurement, the spectrometer configuration was setup B. The plotting symbols, arrows, and uncertainty bars are as in figure 4.1.

### 4.3 Singly-Differential Cross Sections

The doubly-differential cross sections were integrated over the outgoing  $\pi^0$  energy to determine the differential cross section,  $d\sigma/d\Omega_{\text{lab}}$ . Since the doubly-differential cross sections do not extend below 35 MeV, the integral over lower energies was performed with a linear extrapolation to zero at  $T_{\pi^0} = 0$  MeV. The shape of the differential cross section is similar to those in heavier nuclei (see chapter 1) in two respects. At backward angles, the shape and magnitude of the cross section are similar to that for SCX from the free proton. Secondly, this trend does not hold at forward angles, where the cross section is suppressed and shows the effects of Pauli blocking.

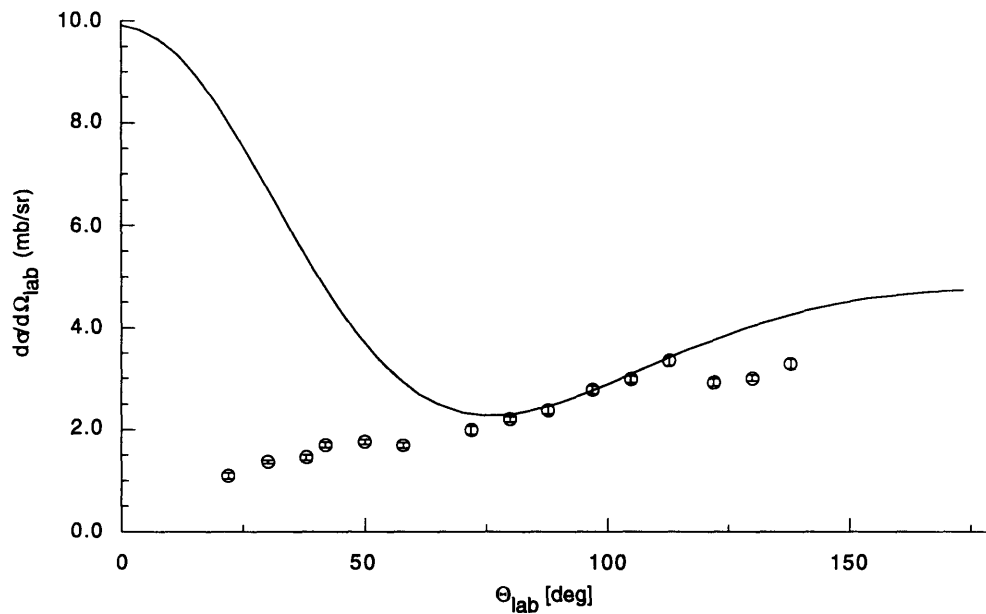


Figure 4.6: Differential cross section for the reaction  ${}^4\text{He}(\pi^-, \pi^0)\text{X}$  at an incident energy of 160 MeV. Each data point is the result of integrating the doubly-differential cross sections in figures 4.1 to 4.5 over the outgoing  $\pi^0$  energies. The solid curve is a phase shift parameterization of the angular distribution for the  $p(\pi^-, \pi^0)n$  reaction.

There is a discontinuity in the angular distribution, outside statistics, between the data taken with the spectrometer at  $105^\circ$  and those taken at  $130^\circ$ . This inconsistency is most likely related to the difficulties in determining the conversion efficiencies and spectrometer acceptance when configured in setup A and setup B as described in chapter 3.

#### 4.4 Total Cross Section

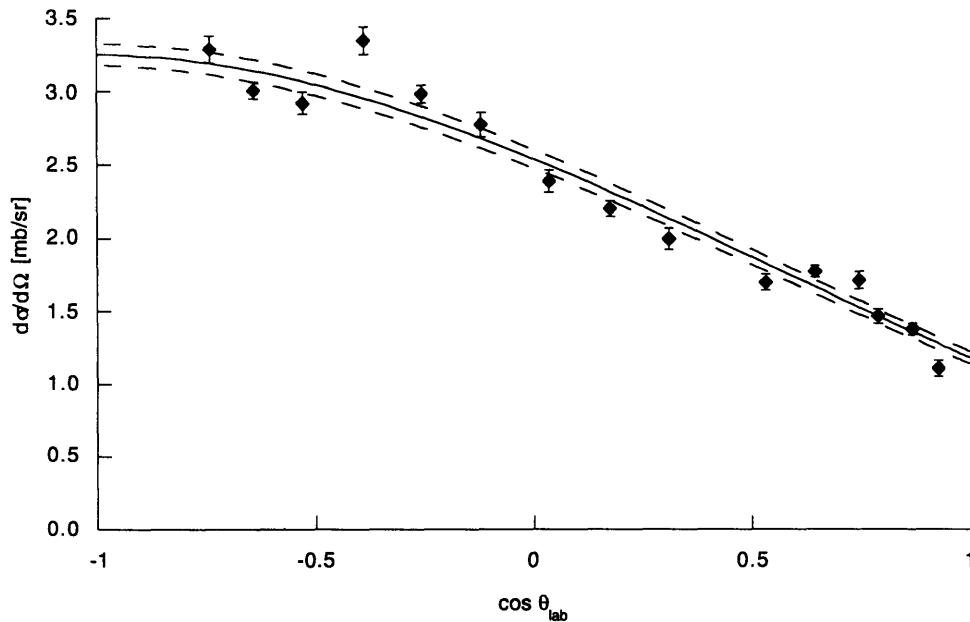


Figure 4.7: Differential cross section for the reaction  ${}^4\text{He}(\pi^-, \pi^0)\text{X}$  plotted as a function of  $\cos \theta_{\text{lab}}$  for 160 MeV incident pions. The solid line is a Legendre polynomial fit to the cross section. The dashed lines are fits to the data plus and minus the uncertainties and create a “corridor of uncertainty” which was used to calculate the uncertainty in the total cross section.

The angular distribution determined above was further integrated over angle to obtain the total cross section,  $\sigma = 30.5 \pm 0.8(\text{stat}) \pm 6.1(\text{syst})$  mb. This was done by fitting a sum of Legendre polynomials to the data. To estimate the statistical error in this calculation, a fit was also made to the data plus and minus the statistical uncertainties for the differential cross section (see figure 4.7). This created a “corridor of uncertainty.” The systematic uncertainties dominate in the determination of the total cross section, as they were taken to be 20%, as discussed in chapter 3.



## Chapter 5: Discussion of SCX Results

In this chapter, the results from this measurement of SCX on  ${}^4\text{He}$  will be discussed as follows. A measure of the effective number of nucleons,  $N_{\text{eff}}$ , and Pauli blocking will be determined. The doubly-differential cross sections feature at all angles a prominent quasifree peak and a low-energy tail. These peaks have been fitted and their positions and widths will be presented as a function of angle. In addition, the positions of the SCX quasi-free peak will be compared with those in quasifree inelastic scattering to determine if there is a shift similar to that observed in  ${}^{16}\text{O}$ . The tails of the spectra are also compared with inelastic scattering data on  ${}^4\text{He}$  to see if there are indications in the low-energy  $\pi^0$  yield of enhanced multiple scattering in the SCX reaction. Theoretical calculations for SCX in  ${}^4\text{He}$  have been performed employing the plane wave impulse approximation (PWIA) and distorted wave impulse approximation (DWIA), and their results will be compared with the data.

### 5.1 Effective Number of Nucleons: $N_{\text{eff}}$

At backward scattering angles, the differential cross section is not affected by Pauli blocking which occurs at forward angles and thus may provide a measure of the effective number of nucleons involved in the reactions. The angular distribution for the  $p(\pi^-, \pi^0)n$  reaction was fitted to the data at large laboratory angles, i.e., angles larger than and including  $\theta_{\text{lab}} = 80^\circ$ . The scaling factor resulting from this fit was found to be  $N_{\text{eff}} = 0.86 \pm 0.17(\text{sys.})$ . While there are two protons available for the incident  $\pi^-$  to exchange charge with,  $N_{\text{eff}} < 2$  is an indication of competing processes such as pion absorption or inelastic scattering. This value for  $N_{\text{eff}}$  is in agreement with the values obtained by Kinney<sup>13</sup> of  $N_{\text{eff}} = 0.88 \pm 0.03$  in the  ${}^4\text{He}(\pi^-, \pi^-)X$  reaction for 180 MeV incident beam and  $N_{\text{eff}} = 0.82 \pm 0.04$  and  $N_{\text{eff}} = 0.95 \pm 0.03$  in the reactions  ${}^4\text{He}(\pi^+, \pi^+)X$  at 150 MeV and 180 MeV, respectively. This is also similar to the agreement of  $N_{\text{eff}}$  observed<sup>31</sup> between SCX and inelastic scattering in heavier nuclei.

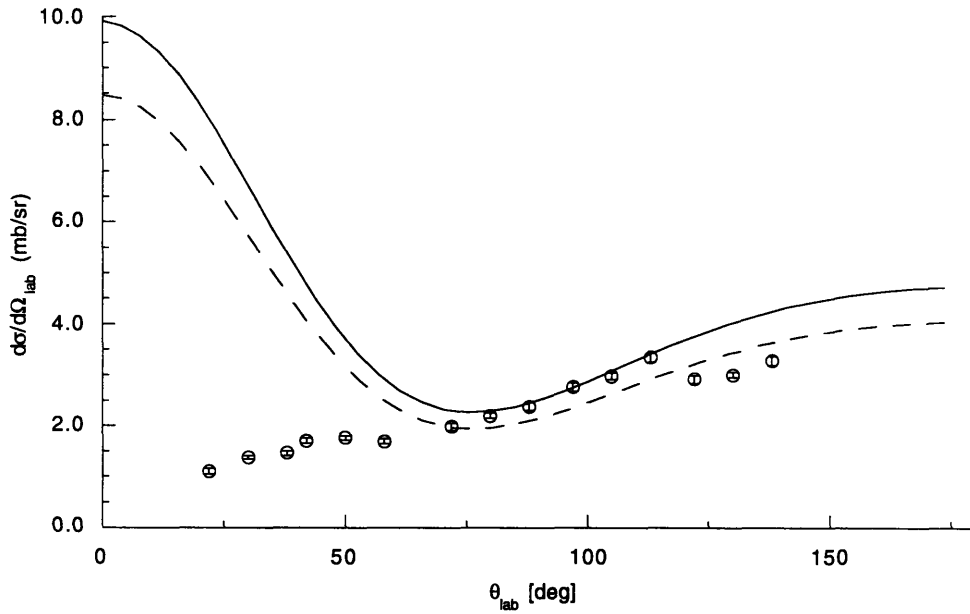


Figure 5.1: Differential cross section for the reaction  ${}^4\text{He}(\pi^-, \pi^0)\text{X}$  at an incident energy of 160 MeV. The solid curve is a phase shift parameterization of the angular distribution for the  $p(\pi^-, \pi^0)n$  reaction, and the dashed curve is a fit of the free proton distribution to the data at backward angles. The scaling factor between the solid and dashed curves is  $N_{\text{eff}} = 0.86$ . The errors bars displayed are purely statistical.

### 5.1.1 Pauli Blocking

The effects of Pauli blocking were estimated by taking the ratio of the total SCX cross section with the normalized free proton total SCX cross section using the following equation:

$$B = \frac{\sigma_{\text{SCX}}}{N_{\text{eff}} \cdot \sigma(\pi^- p \rightarrow \pi^0 n)} \quad (5-1)$$

With the free proton cross section taken to be  $\sigma(\pi^- p \rightarrow \pi^0 n) = 47 \pm 0.5$  mb, we observe a value of  $B = 0.75 \pm 0.15$ . This is in good agreement with the value of  $B = 0.83 \pm 0.13$  observed by Ashery *et al.*<sup>31</sup> for SCX on a range of heavier nuclei at the same incident energy of  $T_{\pi^-} = 160$  MeV. There is a geometric explanation for this agreement, however, which may limit the interpretation of this quantity. To determine the total cross section,

the angular distribution must be integrated over  $4\pi$  steradians where the differential of solid angle is  $d\Omega = d\phi \sin\theta d\theta$ . Since the contributions of the integrand are suppressed at forward and backward angles where  $\sin\theta$  is small, the effects of Pauli blocking are thus suppressed in the calculation of the total cross section.

## 5.2 SCX Quasifree Peaks

The prominent quasifree peaks in the doubly-differential cross section have been fitted to determine the widths and positions of the peak. The function used to determine this fit is a skewed gaussian of the following form:

$$f = \frac{c_2}{c_3\sqrt{2\pi}} \left[ 1 + c_4 \left( z - \frac{z^3}{3} \right) \right] \exp\left( -\frac{z^2}{2} \right) \quad (5-3)$$

where

$$z = \frac{E - E_{qf} - \epsilon}{c_3}, \quad (5-4)$$

$E$  is the outgoing  $\pi^0$  energy, and  $E_{qf}$  is the outgoing pion energy for free proton SCX. The coefficients  $c_2$ ,  $c_3$ , and  $c_4$  represent the area, width, and skew, respectively, of the quasifree peak.

The shift between the energy of the  $\pi^0$  in free proton SCX and the center of the quasifree peak is given by the quantity  $\epsilon$ . As this analysis is only intended to examine the quasifree peak and not the low-energy tail of the distribution, where multiple-scattering effects are expected, data were fitted down to 1/3 of the peak magnitude. The fits to the data are displayed in figure 5.2. The values for  $\epsilon$  and the widths of the quasifree peak are given in table 5.1.

At all angles,  $\epsilon$  is negative, and its magnitude is largest at the most forward angles. This is due to Pauli blocking in  ${}^4\text{He}$  SCX which is not present in charge-exchange from a free

nucleon. Pauli blocking also accounts for the narrow widths at forward angles by cutting off the upper energy side of the quasifree peak. The increase of  $\epsilon$  with increasing scattering angles has been predicted by  $\Delta$ -hole calculations<sup>3</sup>. An increase in width at angles normal to the incident beam, as opposed to forward and backward scattering angles, has been seen in inelastic scattering in  $^3\text{He}$  at 180 MeV<sup>28</sup>. At intermediate to large angles, the width in  $^4\text{He}$  is about 10 MeV greater than in  $^3\text{He}$  due to the larger binding energy, smaller size and correspondingly larger Fermi momentum in  $^4\text{He}$ .

$\theta_{\text{lab}}$ [degrees]	$\epsilon$ [MeV]			Width [MeV]		
22	-30.6	$\pm$	4.0	12.1	$\pm$	1.0
30	-31.8	$\pm$	1.4	13.8	$\pm$	1.0
38	-26.8	$\pm$	2.2	13.7	$\pm$	1.5
42	-26.4	$\pm$	4.5	12.9	$\pm$	2.6
50	-24.2	$\pm$	1.0	15.4	$\pm$	0.8
58	-23.0	$\pm$	2.6	18.0	$\pm$	1.9
72	-15.6	$\pm$	2.0	16.6	$\pm$	1.4
80	-27.1	$\pm$	1.8	30.3	$\pm$	1.3
88	-26.5	$\pm$	5.0	31.2	$\pm$	3.5
97	-19.5	$\pm$	3.1	28.7	$\pm$	2.4
105	-18.0	$\pm$	5.6	26.8	$\pm$	3.5
113	-21.7	$\pm$	0.6	32.4	$\pm$	0.7
122	-18.1	$\pm$	0.6	26.4	$\pm$	0.6
130	-10.4	$\pm$	1.5	21.2	$\pm$	0.9
138	-7.7	$\pm$	1.8	20.8	$\pm$	0.9

Table 5.1: Positions and widths of SCX quasifree peaks determined by fitting skewed gaussian distributions to the data.  $\epsilon$  is the difference between the energy of the centroid of the quasifree peak and the outgoing pion energy for free proton SCX.

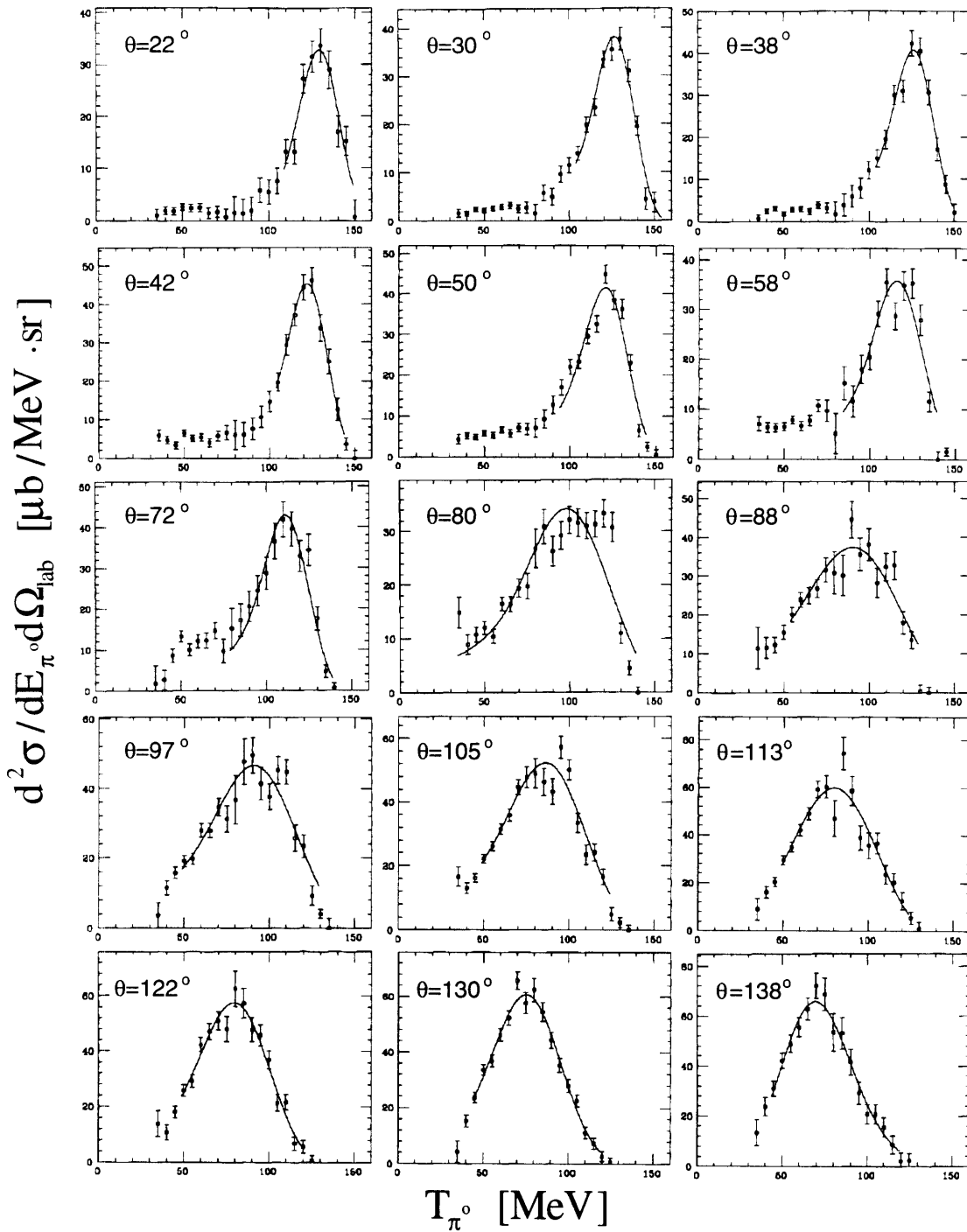


Figure 5.2: Fits used to determine the centroid and width of the SCX quasifree peak.

### 5.3 Comparison with inelastic scattering data

A comparison of the doubly-differential cross sections from SCX and inelastic scattering reactions in  ${}^4\text{He}$  is presented in this section. Although data do not exist for the  ${}^4\text{He}(\pi^+, \pi^+)X$  reaction at 160 MeV, Kinney *et al.*<sup>13</sup> have measured  ${}^4\text{He}(\pi^+, \pi^+)X$  at  $50^\circ$  and  $130^\circ$  for 150 MeV and 180 MeV incident pions. Equivalent 160 MeV spectra were constructed by interpolating between the higher and lower-energy data as described below.

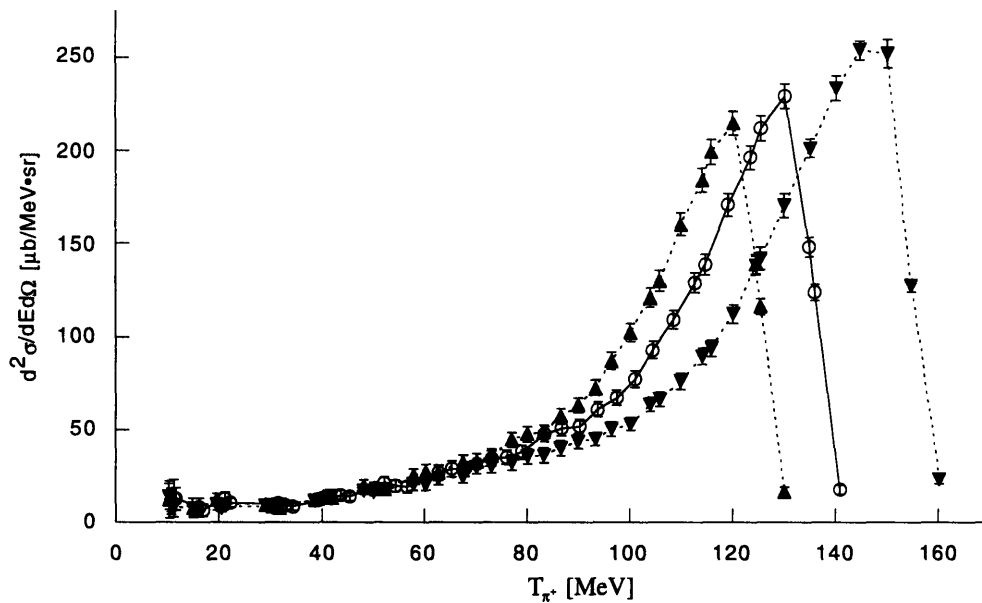


Figure 5.3: The doubly-differential cross section at  $50^\circ$  for the  ${}^4\text{He}(\pi^+, \pi^+)X$  reaction at 160 MeV incident pion energy (open circles) has been constructed through linear interpolation between the spectra at 150 MeV and 180 MeV (up triangles and down triangles, respectively). The magnitude and energy scale of the 150 MeV spectra have been scaled between the magnitudes and positions of the quasifree peaks at 150 MeV and 180 MeV. The solid and dotted lines connect the data points.

To produce a 160 MeV spectrum at  $50^\circ$ , the magnitude and energy scale of the 150 MeV spectra were scaled by factors determined by linearly interpolating the magnitudes and peak positions between it and the 180 MeV spectra (see figure 5.3). At  $130^\circ$ , the magnitudes of both the 150 MeV and 180 MeV inelastic scattering cross sections agree fairly well, and only the energy scale of the 150 MeV cross section was adjusted to create the 160 MeV cross section. The scaling factor was determined by linearly interpolating between

the FWHM positions of the quasifree peaks in both spectra (see figure 5.4).

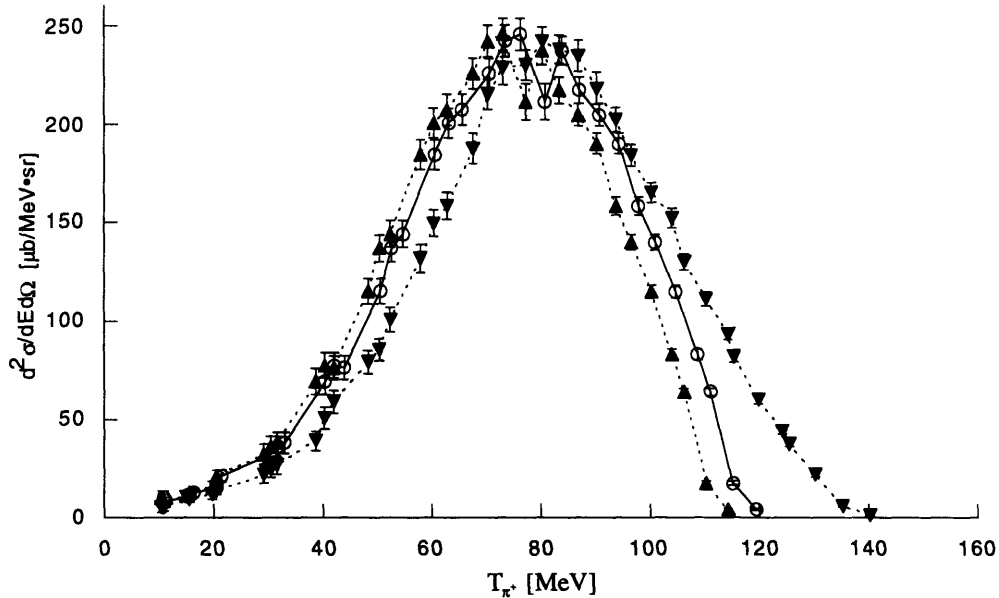


Figure 5.4: The doubly-different cross section at  $130^\circ$  for the  ${}^4\text{He}(\pi^+, \pi^+)X$  reaction at 160 MeV incident pion energy (open circles) has been constructed through linear interpolation between the spectra at 150 MeV and 180 MeV (solid up triangles and solid down triangles, respectively). The energy scale of the 150 MeV spectra has been scaled between the centroids of the quasifree peaks evaluated at half-maximum for the 150 MeV and 180 MeV cross sections.

To compare the constructed inelastic scattering cross sections at 160 MeV with the SCX data, the magnitudes of the inelastic scattering cross sections have been scaled by the ratio of the differential cross sections, i.e., the areas under the doubly-differential cross sections. The normalized inelastic scattering and SCX cross sections (figures 5.5 and 5.6) show a striking resemblance in shapes, positions, and widths of the quasifree peaks at both  $50^\circ$  and  $130^\circ$ . One must conclude that the dominant processes involved in SCX and inelastic scattering in  ${}^4\text{He}$ , in particular, the relative weighting of multiple and single scattering at all outgoing pion energies, are very similar.

The SCX quasifree peak is shifted slightly to lower energies compared to inelastic scattering in both figures by a few MeV. Such a shift is expected from the 3.3 MeV Q-value of SCX

( $Q = 3.3 \text{ MeV} = m_{\pi^-} + m_p - m_{\pi^0} - m_n$ ) on the proton. The much larger shift to lower energies of the peak observed<sup>32</sup> in the charge-exchange reaction in  $^{16}\text{O}$  with respect to the inelastic scattering reaction is not seen in  $^4\text{He}$ .

The ratio of the inelastic scattering and SCX differential cross sections, 4.5 for the  $50^\circ$  cross sections and 4.3 for the  $130^\circ$  cross sections can also be compared with predications based on simple isospin arguments. As presented in chapter 1, the ratios for the free nucleon reaction cross sections are as follows:

$$\left. \begin{array}{l} \sigma(\pi^- n \rightarrow \pi^- n) : \sigma(\pi^- p \rightarrow \pi^0 n) : \sigma(\pi^- p \rightarrow \pi^- p) \\ \sigma(\pi^+ p \rightarrow \pi^+ p) : \sigma(\pi^+ n \rightarrow \pi^0 p) : \sigma(\pi^+ n \rightarrow \pi^+ n) \end{array} \right\} = 9 : 2 : 1 \quad (5-5)$$

When considering scattering from a nucleus in a single-step interaction, the contributions from both protons and neutrons must be added, taking into account the numbers of each nucleon. SCX in  $^4\text{He}$ , when initiated by a  $\pi^-$ , is thus described by

$$\sigma_{\text{SCX}} = 2 \cdot \sigma(\pi^- p \rightarrow \pi^0 n). \quad (5-6)$$

The multiplicative factor “2” makes no adjustment for the possible effects of nucleon “shadowing,” which would lower the effective number of protons available for the reaction. On the other hand, inelastic scattering in  $^4\text{He}$  may proceed through scattering from either type of nucleon and is described by

$$\sigma_{\text{NCX}} = 2 \cdot \sigma(\pi^- p \rightarrow \pi^- p) + 2 \cdot \sigma(\pi^- n \rightarrow \pi^- n). \quad (5-7)$$

As written, the scattering from each nucleon is assumed to be incoherent. The ratio predicted by isospin formalism for inelastic scattering and SCX in  $^4\text{He}$  is thus calculated as

$$\sigma_{\text{NCX}} : \sigma_{\text{SCX}} \quad (5-8)$$



$$\left[2 \cdot \sigma(\pi^- p \rightarrow \pi^- p) + 2 \cdot \sigma(\pi^- n \rightarrow \pi^- n)\right] : 2 \cdot \sigma(\pi^- p \rightarrow \pi^0 n) \quad (5-9)$$

$$[2 \cdot 1 + 2 \cdot 9] : 2 \cdot 2 \quad (5-10)$$

$$5 : 1. \quad (5-11)$$

The 4.5:1 and 4.3:1 ratios calculated from the data should be considered in good agreement, considering the systematic errors in both measurements (20% for SCX, 3.6% for inelastic scattering at 180 MeV, and 6.1% for inelastic scattering at 150 MeV). The above formalism assumes that all protons and neutrons contribute incoherently to the cross section and that the reaction to be the result of only single scattering which is clearly dominant in the peak but a poor assumption for the low-energy tail. Finally, given that the inelastic scattering spectra were constructed using simple linear interpolation, the agreement between the predicted and measured ratios is viewed as a confirmation that the total isospin  $T = \frac{3}{2}$  is a good quantum number for these data.

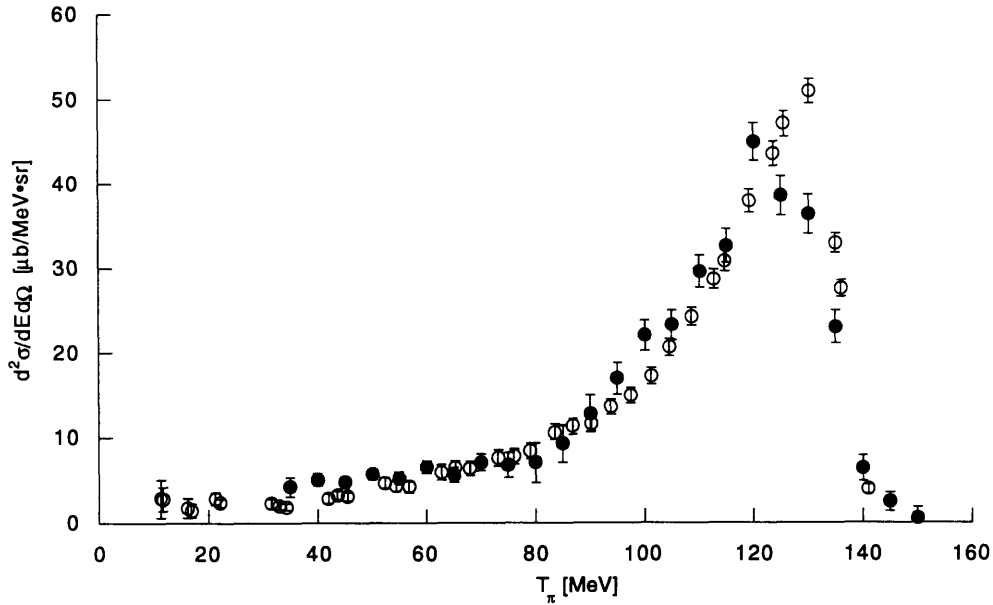


Figure 5.5: Comparison at  $50^\circ$  of the  ${}^4\text{He}(\pi^-, \pi^0)\text{X}$  (solid circles) doubly-differential cross section and the constructed  ${}^4\text{He}(\pi^+, \pi^+)\text{X}$  (open circles) cross section at 160 MeV. The magnitude of the inelastic scattering spectrum has been reduced by a scaling factor of 4.5, the ratio of the differential cross sections.

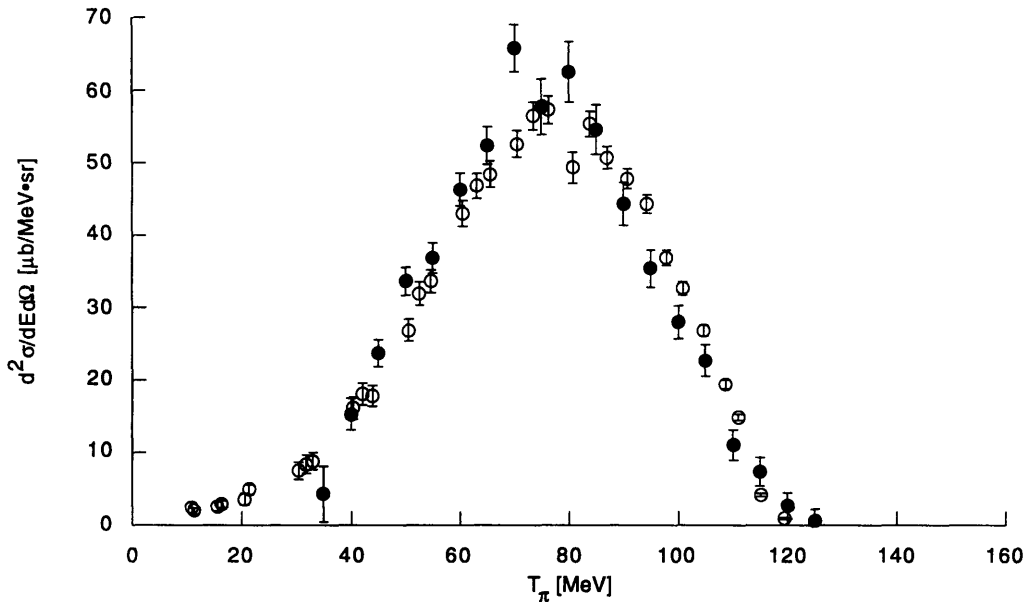


Figure 5.6: Comparison at  $130^\circ$  of the  ${}^4\text{He}(\pi^-, \pi^0)\text{X}$  (solid circles) doubly-differential cross section and the constructed  ${}^4\text{He}(\pi^+, \pi^+)\text{X}$  (open circles) cross section at 160 MeV. The magnitude of the inelastic scattering spectrum has been reduced by a scaling factor of 4.3, the ratio of the differential cross sections.

As mentioned before, the low-energy part of the doubly-differential cross sections is where effects due to the multiple scattering of pions may be important, and it will be examined more closely for indications of double scattering. The simple isospin arguments which were used to predict single-interaction scattering ratios from pion-nucleon and pion-nucleus scattering can further be extended to predict double-scattering ratios. As with the single-interaction calculations in chapter 1, the contributions from the  $T = \frac{1}{2}$  channel are ignored in the  $\Delta$ -resonance region. The scattering cross section for DCX, calculated as two sequential SCX reactions, must involve both protons and can be expressed by

$$\begin{aligned}\sigma_2(\pi^-, \pi^+) &= 2 \cdot 1 \cdot \left| \langle \pi^- p | H_{\text{int}} | \pi^0 n \rangle \right|^2 \left| \langle \pi^0 p | H_{\text{int}} | \pi^+ n \rangle \right|^2 \\ &= \frac{8}{81} \left| A_{3/2} \right|^2\end{aligned}\quad (5-12)$$

The “2 · 1” reflects the fact that the first interaction,  $\pi^- p \rightarrow \pi^0 n$ , may occur on either of the two protons in  ${}^4\text{He}$ , leaving only one proton available for the second interaction,  $\pi^0 p \rightarrow \pi^+ n$ . The cross section for inelastic scattering is similarly calculated, but it includes contributions from different double-interaction processes which are added incoherently as

$$\begin{aligned}\sigma_2(\pi^+, \pi^+) &= 2 \cdot 1 \cdot \left| \langle \pi^+ p | H_{\text{int}} | \pi^+ p \rangle \right|^2 \left| \langle \pi^+ p | H_{\text{int}} | \pi^+ p \rangle \right|^2 + 2 \cdot 1 \cdot \left| \langle \pi^+ n | H_{\text{int}} | \pi^+ n \rangle \right|^2 \left| \langle \pi^+ n | H_{\text{int}} | \pi^+ n \rangle \right|^2 \\ &\quad + 2 \cdot 2 \cdot \left| \langle \pi^+ n | H_{\text{int}} | \pi^+ n \rangle \right|^2 \left| \langle \pi^+ p | H_{\text{int}} | \pi^+ p \rangle \right|^2 + 2 \cdot 2 \cdot \left| \langle \pi^+ p | H_{\text{int}} | \pi^+ p \rangle \right|^2 \left| \langle \pi^+ n | H_{\text{int}} | \pi^+ n \rangle \right|^2 \\ &\quad + 2 \cdot 2 \cdot \left| \langle \pi^+ n | H_{\text{int}} | \pi^0 p \rangle \right|^2 \left| \langle \pi^0 p | H_{\text{int}} | \pi^+ n \rangle \right|^2 \\ &= \frac{252}{81} \left| A_{3/2} \right|^2\end{aligned}\quad (5-13)$$

The cross section for SCX requires the single-interaction amplitude for  $\pi^0 - N$  elastic scattering, which is given as follows:

$$\left| \langle \pi^0 p | H_{\text{int}} | \pi^0 p \rangle \right|^2 = \left| \langle \pi^0 n | H_{\text{int}} | \pi^0 n \rangle \right|^2 = \frac{4}{9} \left| A_{3/2} \right|^2. \quad (5-14)$$

Using this information, the magnitude of the SCX cross section is then calculated similar to those for DCX and inelastic scattering as follows:

$$\begin{aligned}\sigma_2(\pi^-, \pi^0) &= 2 \cdot 2 \cdot \left| \langle \pi^- n | H_{int} | \pi^- n \rangle \right|^2 \left| \langle \pi^- p | H_{int} | \pi^0 n \rangle \right|^2 + 2 \cdot 2 \cdot \left| \langle \pi^- p | H_{int} | \pi^0 n \rangle \right|^2 \left| \langle \pi^0 n | H_{int} | \pi^0 n \rangle \right|^2 \\ &+ 2 \cdot 1 \cdot \left| \langle \pi^- p | H_{int} | \pi^- p \rangle \right|^2 \left| \langle \pi^- p | H_{int} | \pi^0 n \rangle \right|^2 + 2 \cdot 1 \cdot \left| \langle \pi^- p | H_{int} | \pi^0 n \rangle \right|^2 \left| \langle \pi^0 p | H_{int} | \pi^0 p \rangle \right|^2 \quad (5-15) \\ &= \frac{124}{81} |A_{\frac{3}{2}}|^2\end{aligned}$$

The predicted ratio for double-interaction scattering is thus  $\frac{63}{2} : \frac{31}{2} : 1$  or 31.5 : 15.5 : 1, as calculated by

$$\sigma_{\pi^+, \pi^+} : \sigma_{\pi^-, \pi^0} : \sigma_{\pi^-, \pi^+} = \frac{252}{81} : \frac{124}{81} : \frac{8}{81} = 31.5 : 15.5 : 1. \quad (5-16)$$

It should be noted that the ratio for  $\sigma_{\text{NCX}} : \sigma_{\text{SCX}} : \sigma_{\text{DCX}}$  has been quoted elsewhere<sup>16,31</sup> (for heavier nuclei ranging from  $^{12}\text{C}$  to Pb) as 26 : 9 : 1, a value based upon two assumptions, one of which does not hold for our reaction. First, the numbers of neutrons and protons are taken to be equal. This is true for  $^4\text{He}$ , but it cannot be applied to heavy nuclei which are neutron-rich. Secondly, the numbers of neutrons and protons available for the second scattering are taken to be the same as for the original, undisturbed nucleus. These two assumptions which lead to the ratio 26 : 9 : 1 should be valid for medium nuclei, where  $N \sim Z$ , and the ratios

$$\frac{N-1}{N} \approx \frac{Z-1}{Z} \approx 1. \quad (5-17)$$

To examine whether the low-energy tails from inelastic scattering, SCX, and DCX doubly-differential cross sections at  $50^\circ$  follow the 31.5 : 15.5 : 1 ratios predicted by these isospin arguments, all three have been plotted together scaled by 1,  $\frac{31}{2}$ , and  $\frac{63}{2}$  respectively (figure 5.7). The  $^4\text{He}(\pi^-, \pi^0)\text{X}$  SCX data are from this experiment, and the  $^4\text{He}(\pi^+, \pi^+)\text{X}$  inelastic scattering data are those constructed as described above. DCX data on  $^4\text{He}$  exist at 150 MeV and at 180 MeV<sup>13</sup>, but the high-energy part of the 180 MeV spectrum is quite

different from that in the 150 MeV data making any interpolation difficult. The low-energy parts of the 150 MeV and 180 MeV DCX spectra are both featureless and similar in shape and magnitude, and in figure 5.7, the tail of the 150 MeV data is presented multiplied by the  $\frac{63}{2}$  isospin scaling factor.

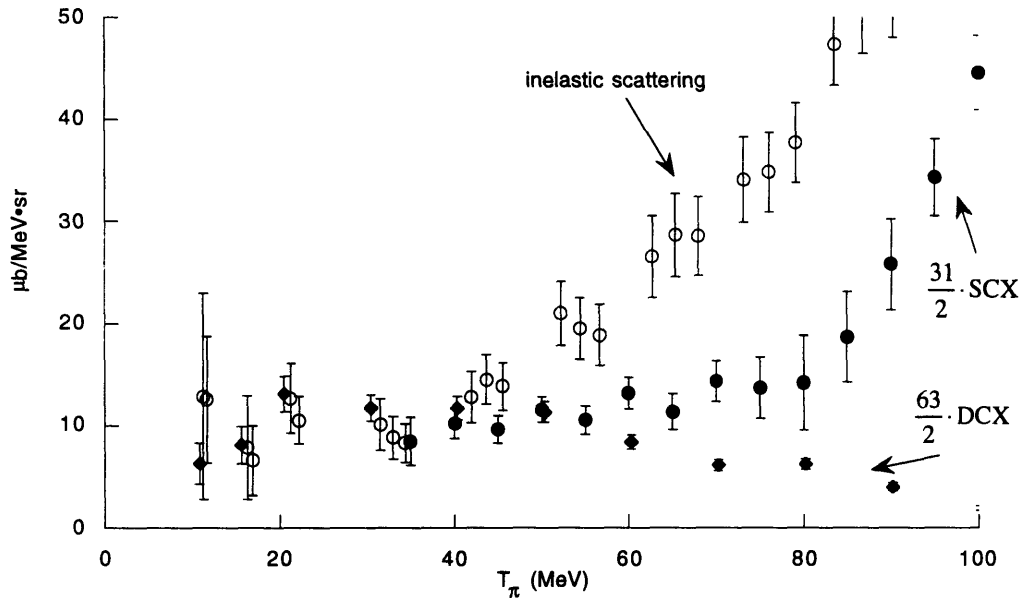


Figure 5.7: The low-energy portions of the doubly-differential cross sections at  $50^\circ$  from the inelastic scattering ( $\pi^+, \pi^+$ ) reaction, the SCX ( $\pi^-, \pi^0$ ) reaction, and the DCX ( $\pi^+, \pi^-$ ) reaction in  ${}^4\text{He}$ . They are scaled by the ratios predicted for double-scattering using the isospin arguments presented.

The scaled SCX and DCX spectra agree quite well with each other from about 55 MeV on down. The inelastic scattering spectra agree with the scaled SCX and DCX spectra from about 45 MeV on down. This is consistent with double-scattering being the dominant reaction mechanism at these lower energies. Furthermore, the agreement between SCX and inelastic scattering is inconsistent with the prediction that SCX should exhibit more double scattering because of less competition with absorption.

## 5.4 Impulse Approximation Calculations

Calculations based on the impulse approximation<sup>60,61</sup> have been performed of the  ${}^4\text{He}(\pi^-, \pi^0)\text{X}$  reaction cross section. In this model, the basic assumption is that the scattering proceeds through the quasifree interaction of the pion with only one nucleon which is knocked out of the nucleus. The remaining nucleons are spectators and act to conserve charge, momentum, and energy in the reaction, in addition to providing the initial and final state potentials. As such, multiple-scattering effects are not included explicitly in the calculation, and a comparison with the data may thus reveal multiple-scattering effects in the physical process. The following subsections outline the formalism behind the calculations, the initial energy (IEP) and final energy (FEP) prescriptions, and the plane wave (PWIA) and distorted wave (DWIA) impulse approximations for both energy prescriptions. Finally, the results of the calculations will be compared with the data.

The code THREEDEE of Chant<sup>62</sup>, as modified by Khandaker<sup>63,64</sup> for the Hydrogen and Helium isotopes, has been used. The program calculates the doubly-differential cross section for the  ${}^4\text{He}(\pi^-, \pi^0\text{n}){}^3\text{H}$  reaction, assuming the reaction proceeds through the quasifree  $p(\pi^-, \pi^0)\text{n}$  process. The results have been integrated over the outgoing neutron phase space to obtain the inclusive  $(\pi^-, \pi^0)$  cross sections.

### 5.4.1 Impulse Approximation Formalism

The cross section for the  $A(\pi, \pi')B$  reaction is described by

$$\frac{d\sigma}{d\Omega}(A \rightarrow B) = \frac{2\pi}{\hbar v} |\langle \phi_{\vec{k}'}; B | T | \phi_{\vec{k}}; A \rangle|^2 \rho_f(\vec{k}'; B), \quad (5-18)$$

where

T is the transition operator for the reaction

A and B are the initial and final states of the nucleus,  
 $\vec{k}$  and  $\vec{k}'$  are the momenta of the incident and outgoing pions,  
 $v$  is the relative velocity of the incident pion and the target nucleus,  
 $\phi_{\vec{k}}$  and  $\phi_{\vec{k}'}$  are the incident and final pion wave functions, taken to be plane waves for the PWIA calculations, and  
 $\rho_f(\vec{k}'; B)$  is the energy density of final states.

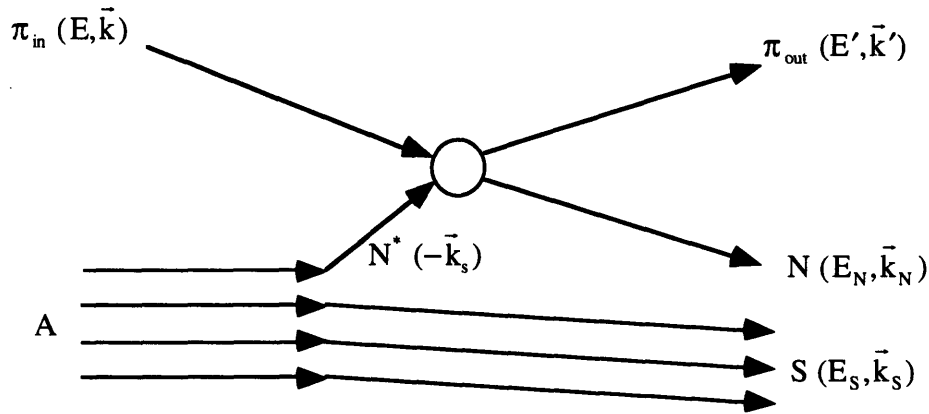


Figure 5.8: Diagram of the quasifree scattering mechanism for the  $A(\pi, \pi'N)S$  reaction showing the variables used in the calculation for the incident and outgoing pions, the knocked out nucleon  $N$ , the target nucleus  $A$ , and the recoil nucleus  $S$ .

The impulse approximation for pion-nucleus scattering is made by using the free pion-nucleon transition matrix  $t_{free}$  rather than the in-medium transition matrix  $t_i$ . The assumption that the reaction involves only single scattering from one nucleon further simplifies the total transition matrix. This matrix is commonly written in a multiple-scattering series known as the Watson Series<sup>66</sup>,

$$T = \sum_{i=1}^A t_i + \sum_{i=1}^A t_i G_0 \sum_{j \neq i}^A t_j + \sum_{i=1}^A t_i G_0 \sum_{j \neq i}^A t_j G_0 \sum_{k \neq j}^A t_k + \dots \quad (5-19)$$

where  $G_0$  is the in-medium propagator. The form of the impulse approximation transition matrix only includes the first term of the series,

$$T = \sum_{i=1}^A t_{\text{free}} . \quad (5-20)$$

The impulse approximation is based on two assumptions. First, the difference between the in-medium and free transition matrices must be small for the approximation to be applicable. For this measurement, the incident pion energy of 160 MeV far exceeds the proton separation energy  $S_p = 19.8$  MeV in  ${}^4\text{He}$ , and thus the calculation should be valid. Secondly, by taking only the first term of the Watson series, multiple-scattering effects are discarded entirely.

The inclusive doubly-differential cross section for scattering from a single nucleon was determined by integrating over the solid angle of the undetected nucleon,

$$\frac{d^2\sigma}{d\Omega_\pi dE'_\pi}(\pi_{\text{in}}, \pi_{\text{out}}) = \int d\Omega_N \frac{d^3\sigma}{d\Omega_\pi d\Omega_N dE'_\pi}, \quad (5-21)$$

using a Gauss-Legendre quadrature technique. The inclusive doubly-differential cross section in nuclei must take into account the populations of target nucleons available to scatter from. For SCX reactions in  ${}^4\text{He}$  initiated by a  $\pi^-$ , the number of protons ( $Z=2$ ) multiplies the proton cross section.

$$\frac{d^2\sigma}{d\Omega_\pi dE'_\pi} = 2 \cdot \frac{d^2\sigma_{\text{proton}}}{d\Omega_\pi dE'_\pi}(\pi^-, \pi^0) \quad (5-22)$$

#### 5.4.2 Distorted Wave Impulse Approximation (DWIA)

DWIA calculations which modeled the physical process were performed and compared to the data. These calculations employed the factorized DWIA formalism by Chant and Roos<sup>66</sup>. To perform the calculation, the  ${}^4\text{He}(\pi^-, \pi^0)n$  reaction is broken into three separate parts as follows:



1. The interaction between the incident  $\pi^-$  and the  ${}^4\text{He}$  nucleus.
2. The interaction between the outgoing  $\pi^0$  and the recoil  ${}^3\text{H}$  nucleus
3. The final state interaction (FSI) between the outgoing neutron and the  ${}^3\text{H}$  nucleus.

First, the single-nucleon bound-state wave function in the ground state was specified using a parameterization of the nucleon-trinucleon overlap function in  ${}^4\text{He}$  by Greben<sup>67</sup>. THREEDEE, as modified by Khandaker<sup>64,68</sup> for  $\pi-{}^4\text{He}$  reactions, obtained the pion distorted waves for both the incident and outgoing pions from a modified Klein-Gordon equation<sup>68</sup> with a Kisslinger-type optical potential. The parameters for the optical potential were chosen to reproduce measured elastic-scattering angular distributions. For inclusion of nucleon FSI, distorted waves for the knocked out neutron were generated using a Woods-Saxon potential in a Schrödinger equation. The parameters for this potential were obtained through analysis of  $p-{}^3\text{He}$  forward-angle elastic-scattering data.

The factorized DWIA expression for the  $A(\pi, \pi'N)S$  triply-differential three-body cross section, as expressed in the  $\pi$ -nucleus laboratory frame, is

$$\frac{d^3\sigma}{d\Omega_\pi d\Omega_N dE'_\pi} = \frac{2\pi}{\hbar v_\pi} \omega_s C^2 S_{ij} |\langle \bar{t} \rangle|^2 \sum_\lambda |T_{SA}^{\alpha\lambda}|^2. \quad (5-23)$$

where

- $v_\pi$  is the relative velocity of the incoming pion and the target nucleus,
- $\omega_s$  is the energy density of the final states,
- $C = \langle t_N v_N T_S N_S | T_A N_A \rangle$  is the isospin Clebsch-Gordan coupling coefficient ( $N_A$  is the projection of  $T_A$ ),
- $S_{ij}$  is the single-nucleon spectroscopic factor arising from the overlap of initial and final nuclear states.

### 5.4.3 Initial Energy and Final Energy Prescriptions

The cross section calculated in equation (5-23) is properly a half-off-the-energy shell cross section since the struck nucleon is bound and the pion is free. The half-off-the-energy shell two-body t-matrix  $\langle \bar{t} \rangle^2$ , however, is not known, and it is common to approximate it with the on-shell amplitude. The question arises as to the energy at which the relative energies of the pion and struck nucleon in the  $\pi N$  center of mass system should be evaluated. There are two common prescriptions for this energy, and both were used in this calculation.

In the final energy prescription (FEP), the two-body total relativistic energy,  $E_{c.m.}$ , is chosen so that the momenta of the outgoing  $\pi^0$  and neutron in the  $\pi^- + p \rightarrow \pi^0 + n$  center-of-mass frame are equal to the corresponding values in the  $\pi^0 + n$  rest frame in the  $\pi^- + p \rightarrow \pi^0 + n + {}^3\text{H}$  reaction. Since the  $\pi^0$  and neutron are both on shell, this reduces to  $E_{c.m.} = E_{\pi^0 + n}$ , i.e., the total energy of the  $\pi^0$  and neutron in their rest frame.

In the initial energy prescription (IEP),  $E_{c.m.}$  is chosen so that the incident  $\pi^-$  has a momentum equal to the momentum of the  $\pi^-$  in the  $\pi^0 + n$  rest frame while the proton has equal and opposite momentum. Since the mass (the mass difference between  ${}^4\text{He}$  and  ${}^3\text{H}$ ) of the “virtual” particle is not equal to the mass of the proton, the corresponding energy, of the form  $E_{c.m.} = E_{\pi^-} + \sqrt{P_{\pi^-}^2 + M_p^2}$ , is not equal to  $E_{\pi^0 + n}$ , and the initial energy will be higher than the final energy by roughly the proton separation energy in  ${}^4\text{He}$  of 19.4 MeV.

### 5.4.4 Plane Wave Impulse Approximation (PWIA)

PWIA calculations were performed to assess the importance of distortions. The results correspond to the classical straight-line trajectory model of scattering. Distortions of the incident and scattered pion, as well as the knocked-out nucleon, are ignored, and the

---

wavefunctions of the pions are expressed as plane waves:

$$\Psi_{\mathbf{k}}(\vec{\mathbf{r}}) = \frac{1}{(2\pi)^{3/2}} e^{i\vec{\mathbf{k}} \cdot \vec{\mathbf{r}}}. \quad (5-24)$$

where  $\vec{\mathbf{r}}$  and  $\vec{\mathbf{k}}$  are the relative position and momentum of the particle respectively. In the PWIA, the matrix element simplifies to the Fourier transform of the single nucleon bound state wave function.

## 5.5 Comparison of the Data with the Calculation

The results of the PWIA and DWIA calculations, in both the IEP and FEP, are presented in figure 5.9. At all scattering angles, and particularly at forward angles, the PWIA calculations overestimate the cross sections. This is not surprising, as factors such as absorption and final-state interactions, which are known to be important in pion scattering, are not included in the plane wave approximation. Absorption removes pions, thereby lowering the cross section, and final-state interactions redistribute them to lower energies and larger angles.

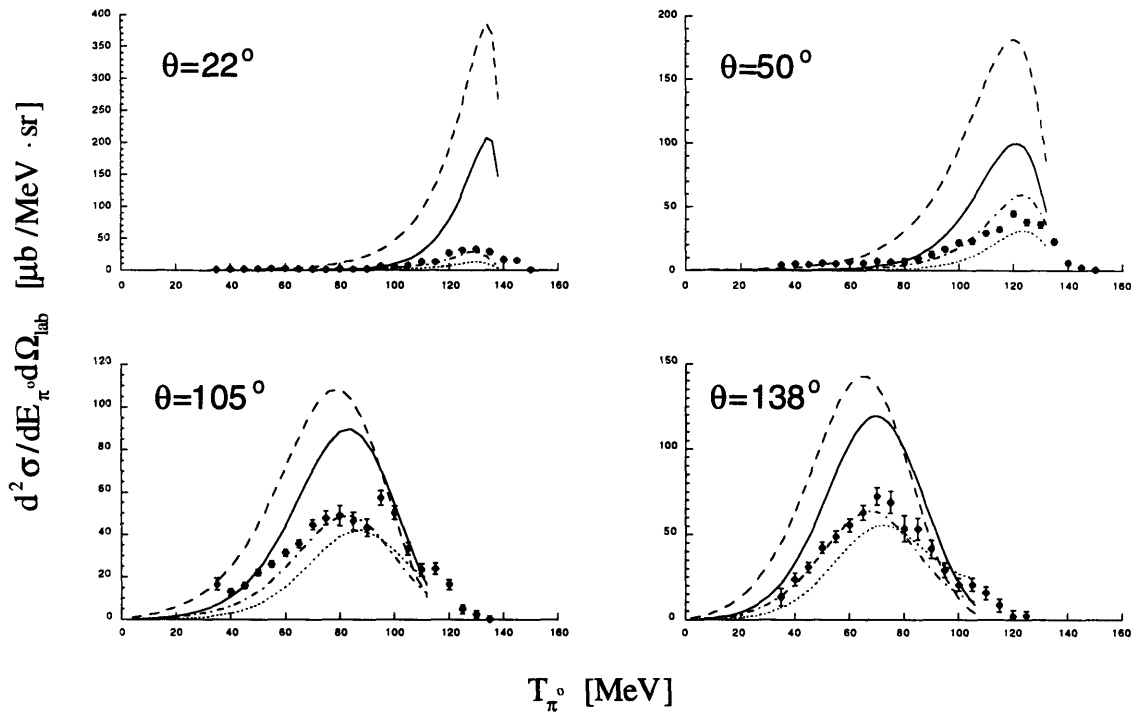


Figure 5.9: Results of the PWIA calculation using the initial (dot-dash) and final (solid) energy prescriptions and of the DWIA calculation using the initial (dot) and final (dashed) prescriptions for the  ${}^4\text{He}(\pi^-, \pi^0)\text{X}$  reaction at an incident energy of 160 MeV and four scattering angles. The energy scales are the same for all plots, but the cross section axes are not.

The results of the DWIA calculations, in both the IEP and FEP, are compared with the data in figures 5.10 to 5.17. The results, which include absorption and final-state interaction effects, are in good agreement with the data in the region of the peak, with the IEP being in better agreement than the FEP. At energies lower than the quasifree peak, however, both the IEP and FEP disagree with the data, as shown by plotting the comparison on a logarithmic scale in figure 5.16. This is indication that processes other than single-scattering, such as final state interactions and multiple scattering, are contributing to the low-energy cross section.

Above the region of the peak, the DWIA calculations also disagree by being lower than the data. This may be considered surprising even though the corrections to the data due to

---

PIANG are greatest here, and the calculations do not extend to the highest energies in some cases due to the non-availability of the t-matrix. The enhancement of the cross section is possible indication of SCX to an excited state of  ${}^4\text{H}$ , such as isobaric analogs of the T=1 states in  ${}^4\text{He}$  which lie at 25-30 MeV<sup>6,70</sup>. The excess cross section at around  $80^\circ - 100^\circ$  might indicate the excitation of T=1 giant dipole states.

The IEP results, for the DWIA, have a peak height greater than the FEP results. This reflects the importance of the  $\Delta$ , as incorporated phenomenologically through the t-matrix. The IEP is evaluated at a higher energy than the FEP, and it is thus closer to the excitation energy of the  $\Delta$ . Similar calculations of the SCX reaction in  ${}^3\text{He}$  by Dowell<sup>37</sup> at 245 MeV display a reversed trend with the FEP being higher than the IEP presumably because the t-matrix is evaluated at lower energies which are closer to the  $\Delta$ . This trend is supported by Yuly<sup>28</sup>, who performed calculations of the inelastic scattering reaction in  ${}^3\text{He}$  to compare with measurements at 120 MeV, 180 MeV, and 240 MeV. For the 120 MeV calculation, the IEP is higher since the incident energy is closer to the 180 MeV excitation energy of the  $\Delta$ , and at 240 MeV, the FEP is higher. At 180 MeV, both IEP and FEP are nearly equal.

The differences between the IEP and FEP calculations, in both the plane wave and distorted wave approximations, is greater than in the calculations<sup>37</sup> in  ${}^3\text{He}$ . This is presumably due to the greater nucleon separation energies in  ${}^4\text{He}$  ( $S_p = 19.8$  MeV) compared with  ${}^3\text{He}$  ( $S_p = 5.5$  MeV) leading to a greater difference between incident and outgoing pion energies. In addition, the  ${}^3\text{He}$  reactions were measured at higher incident energies making the relative importance of the separation and incident energies less than in the  ${}^4\text{He}$  measurement.

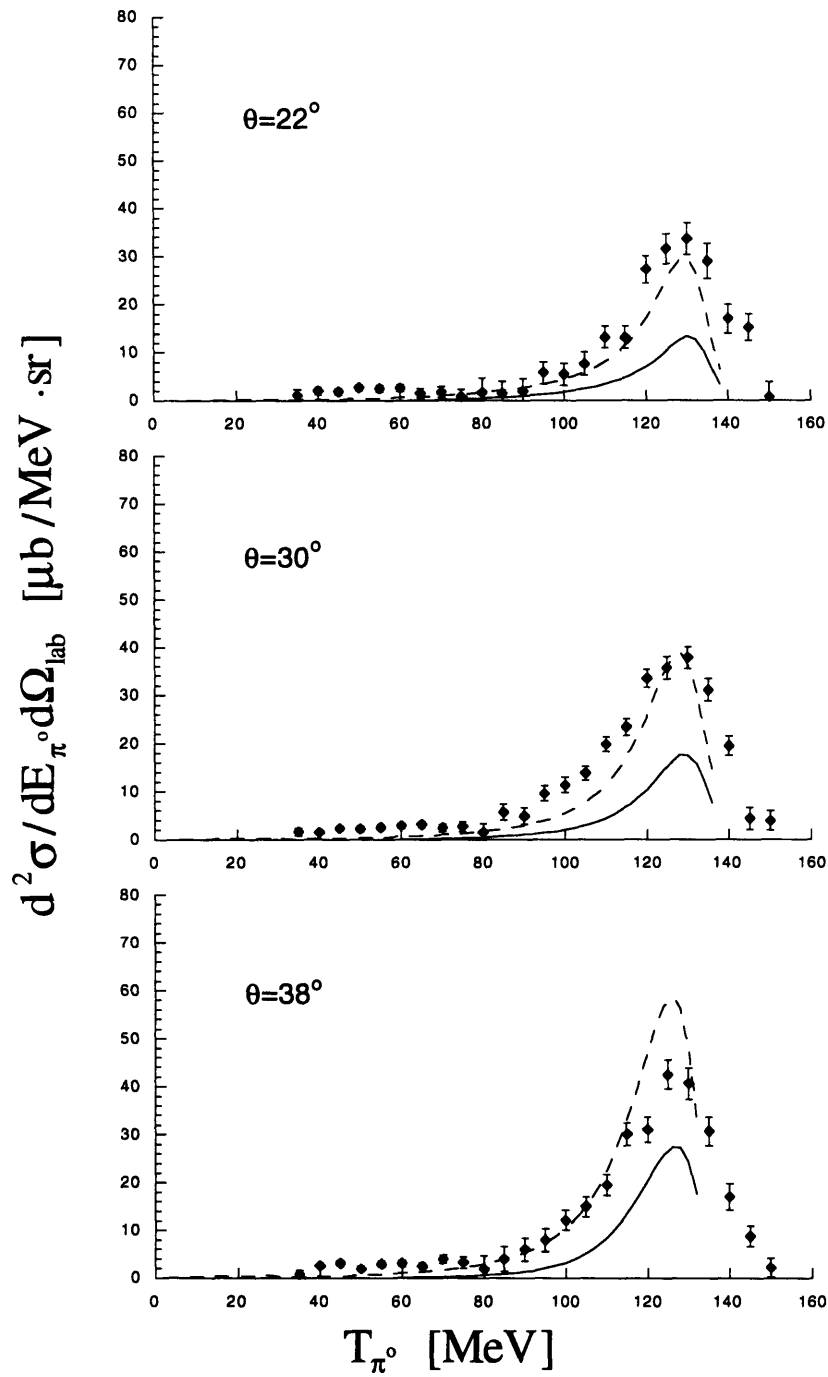


Figure 5.10: Results of the DWIA calculation using the initial (dashed) and final (solid) energy prescriptions for the  ${}^4\text{He}(\pi^-, \pi^0)\text{X}$  reaction at an incident energy of 160 MeV. The data were taken at the nominal spectrometer scattering angle of  $30^\circ$ .

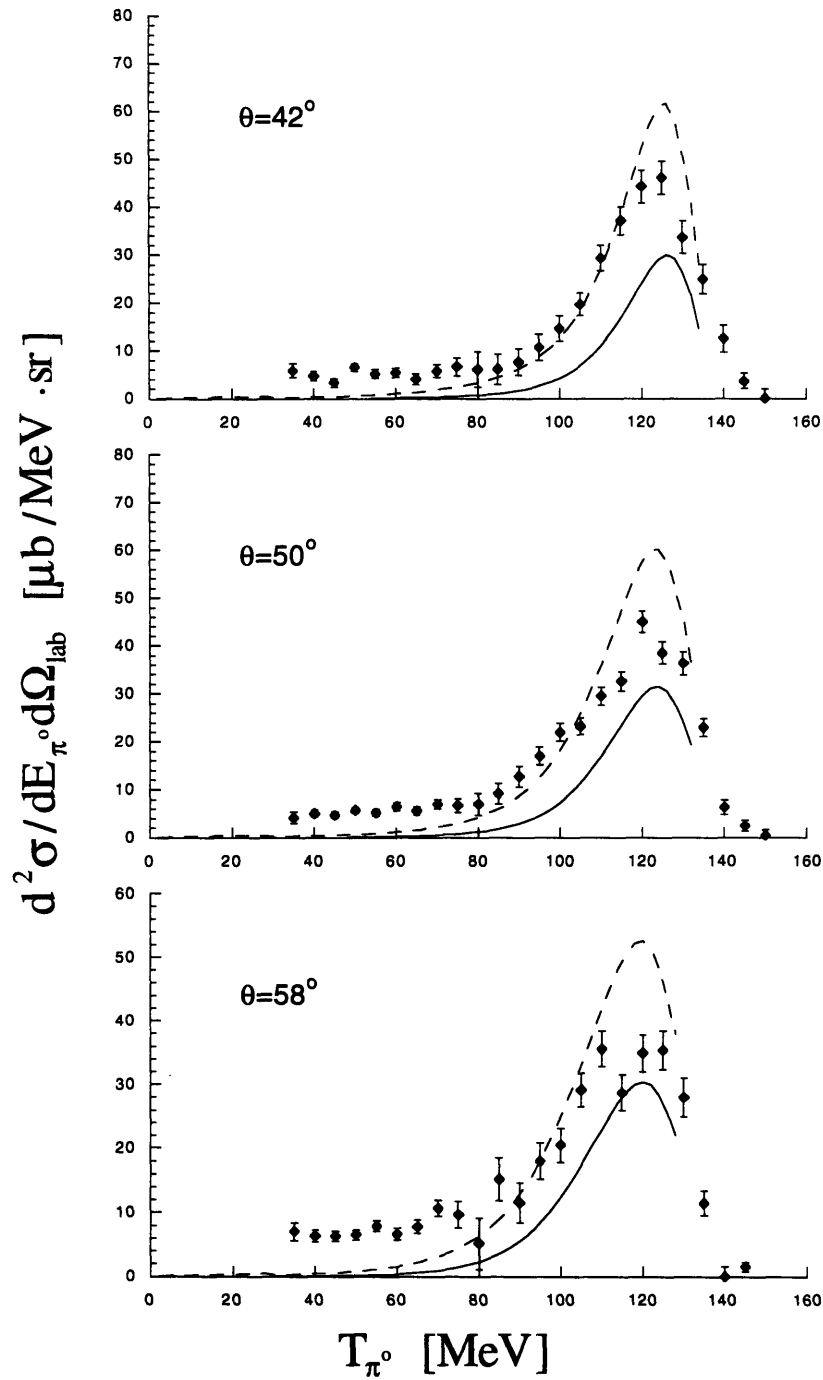


Figure 5.11: Results of the DWIA calculation using the IEP (dashed) and FEP (solid) for the  ${}^4\text{He}(\pi^-, \pi^0)\text{X}$  reaction at 160 MeV. The data were taken at the nominal spectrometer scattering angle of  $50^\circ$ .

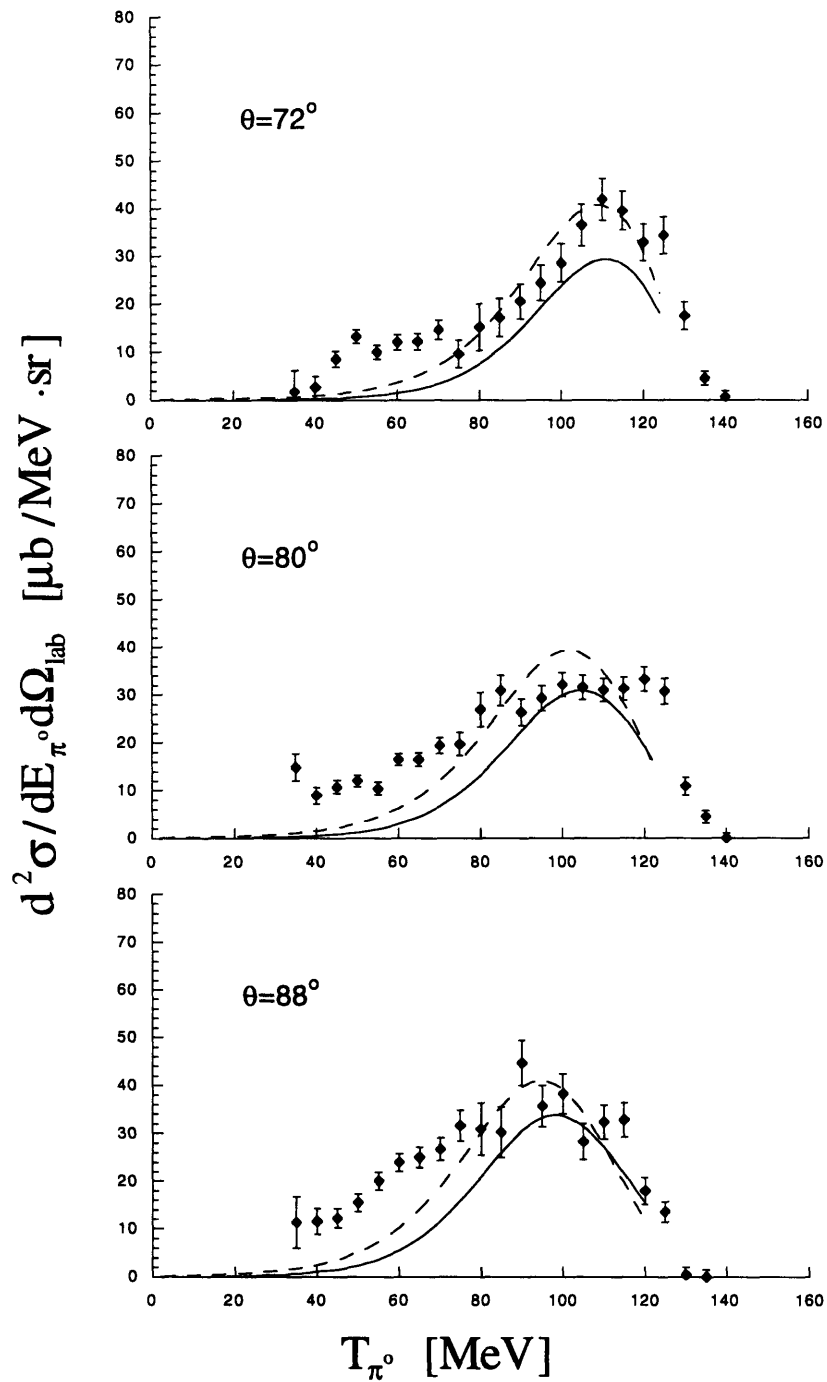


Figure 5.12: Results of the DWIA calculation using the IEP (dashed) and FEP (solid) for the  ${}^4\text{He}(\pi^-, \pi^0)\text{X}$  reaction at 160 MeV. The data were taken at the nominal spectrometer scattering angle of  $80^\circ$ .



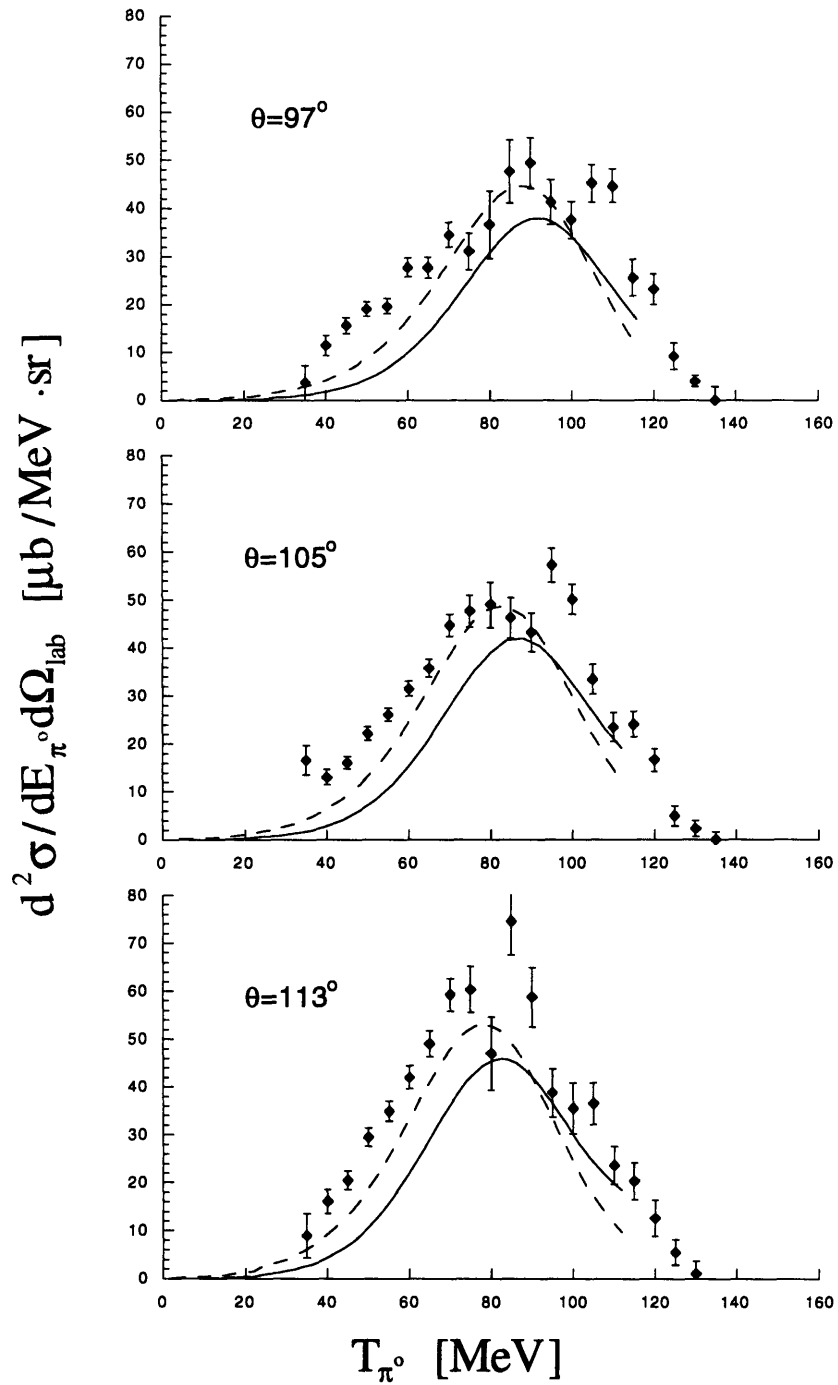


Figure 5.13: Results of the DWIA calculation using the IEP (dashed) and FEP (solid) for the  ${}^4\text{He}(\pi^-, \pi^0)\text{X}$  reaction at 160 MeV. The data were taken at the nominal spectrometer scattering angle of  $105^\circ$ .

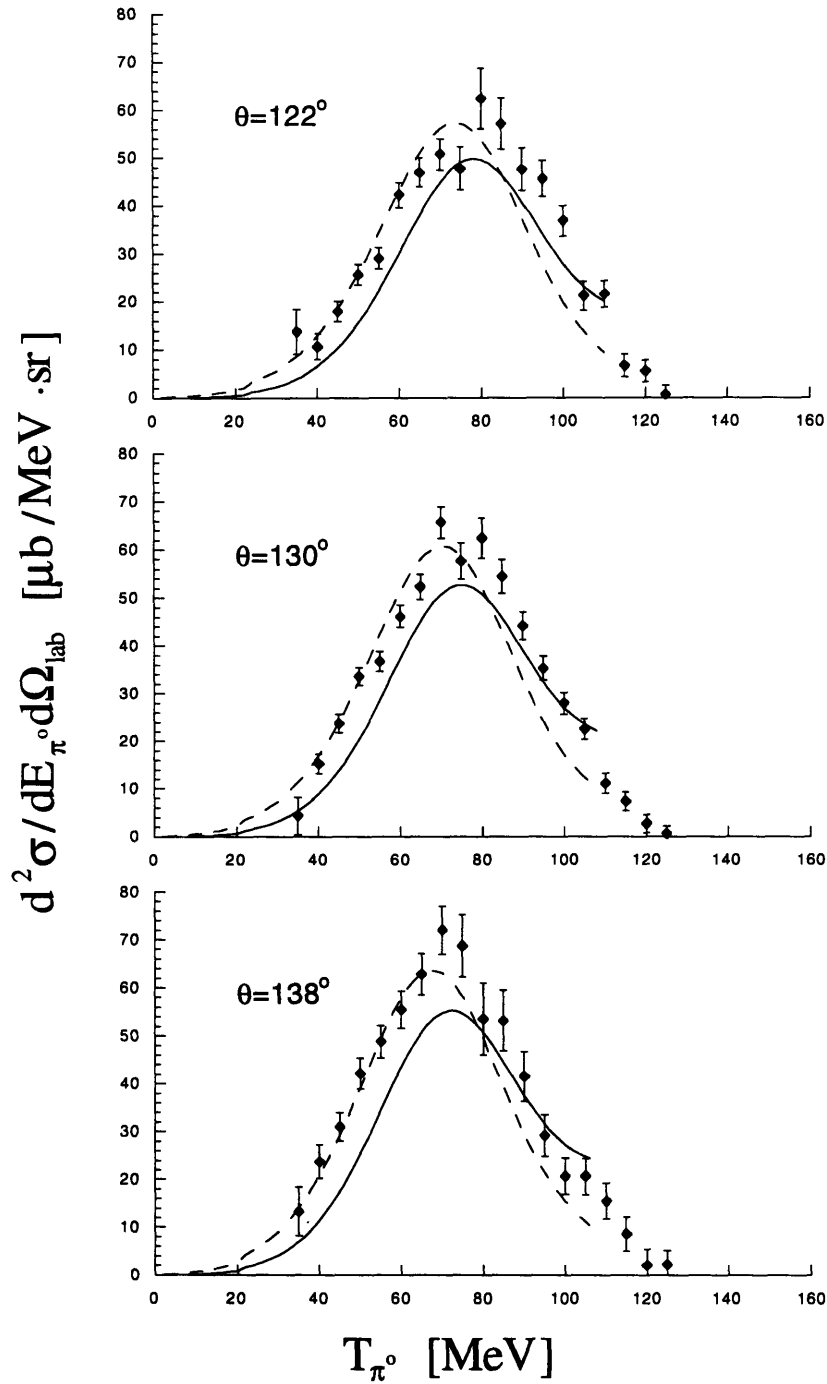


Figure 5.14: Results of the DWIA calculation using the IEP (dashed) and FEP (solid) for the  ${}^4\text{He}(\pi^-, \pi^0)\text{X}$  reaction at 160 MeV. The data were taken at the nominal spectrometer scattering angle of  $130^\circ$ .

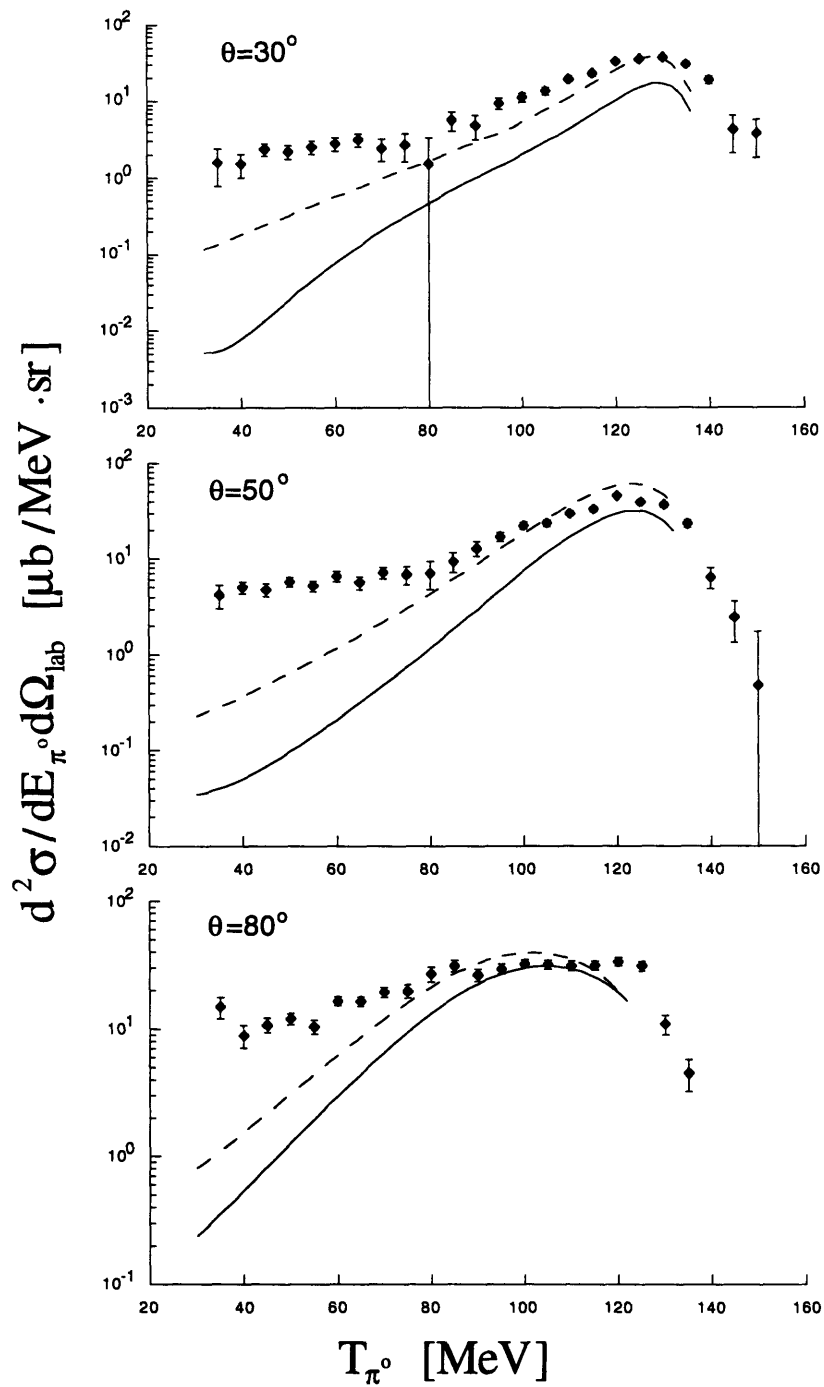


Figure 5.15: Semilogarithmic plots of the results of the DWIA calculation using the IEP (dashed) and FEP (solid) for the  ${}^4\text{He}(\pi^-, \pi^0)\text{X}$  reaction at 160 MeV at  $30^\circ$ ,  $50^\circ$ , and  $80^\circ$ . The data are higher than the IEP by an order of magnitude at the lowest energies.

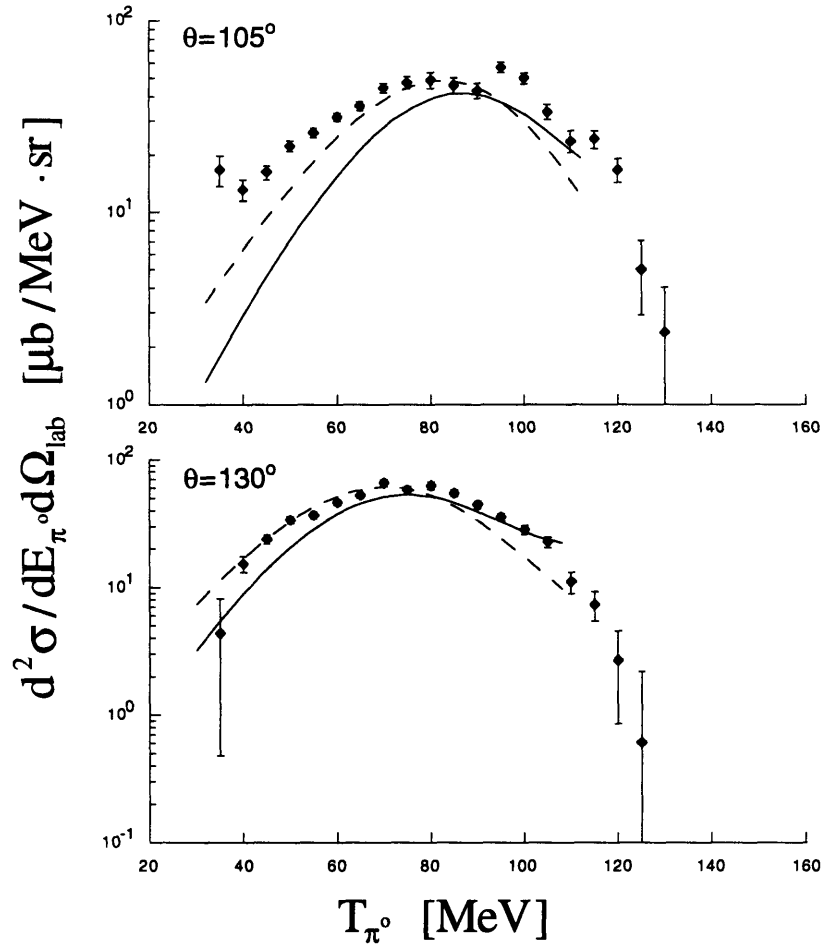


Figure 5.16: Semilogarithmic plots of the results of the DWIA calculation using the IEP (dashed) and FEP (solid) for the  ${}^4\text{He}(\pi^-, \pi^0)\text{X}$  reaction at 160 MeV at  $105^\circ$  and  $130^\circ$ .

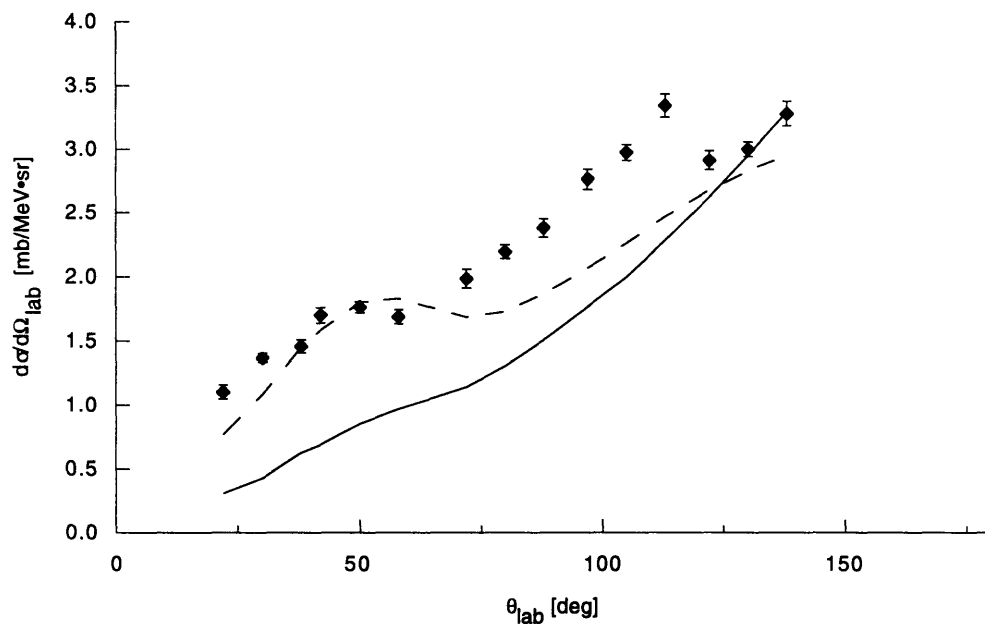


Figure 5.17: The angular distribution of the  ${}^4\text{He}(\pi^-, \pi^0)\text{X}$  reaction at 160 MeV and Results of the DWIA calculation using the IEP (dashed) and FEP (solid) . The errors are statistical only.

The measured angular distribution is compared with that predicted by the DWIA calculation in both the IEP and FEP in figure 5.17. As with the doubly-differential cross sections, the IEP reproduces the data better than the FEP. At forward angles, the IEP better describes the effects of Pauli blocking in the data.



---

## Chapter 6: Summary and Conclusions

The strength of the  $\pi N$  interaction guarantees that multiple-scattering effects will be important in pion scattering reactions. Pion single-charge-exchange (SCX) is one of three possible reactions, along with double-charge-exchange (DCX) and inelastic scattering, leading to a pion in the final state. Pion absorption plays a competing role in each, as the pion may be absorbed within the nucleus at each scattering. The  $\Delta$ -resonance in the  $\pi - N$  system influences all scattering reactions having a total energy within a hundred MeV of the peak of the resonance at 1232 MeV. In particular, the angular distributions and total cross sections are related to the isospin and spin properties of the  $\Delta$ .

The measurement of pion SCX in  ${}^4\text{He}$  in the  $\Delta$ -resonance region presented in this thesis allows for a complete study of the reactions in this nucleus since DCX and inelastic scattering have been previously measured<sup>13</sup>. Inelastic scattering reactions are dominated by quasifree scattering, or scattering from a single, bound nucleon. On the other hand, DCX is an inherently multiple-scattering process, requiring at least two like nucleons to proceed. The doubly-differential cross section for DCX at forward angles shows a distinctive double-humped shape consistent with a two-step sequential SCX mechanism. In both processes, the data indicate that the reaction mechanisms primarily involve only the minimum number of nucleons required.

SCX may be predicted to exhibit added signs of multiple scattering since the reaction cannot proceed through the intermediate  ${}^5S_2$   $\Delta - N$  state, which is the primary two-body absorption channel, due to isospin, parity, and angular momentum arguments. These signs should manifest as an enhancement of the low-energy tails of the doubly-differential cross sections since the pion loses energy with each interaction. Though measurements of SCX on heavier nuclei<sup>31,32</sup> reveal the process to be predominantly quasifree, there is indication of multiple scattering. A recently analyzed<sup>37</sup> measurement of SCX on  ${}^3\text{He}$  for an incident energy of 245 MeV, at the upper energy side of the  $\Delta$ , also gives indication for multiple scattering, though the data are not statistically precise enough and do not

extend to low enough energies to be conclusive.

This measurement of the SCX reaction  ${}^4\text{He}(\pi^-, \pi^0)\text{X}$  was made at the incident energy of 160 MeV at scattering angles  $30^\circ$ ,  $50^\circ$ ,  $80^\circ$ ,  $105^\circ$ , and  $130^\circ$ . It was conducted during the Summer of 1990 at the Clinton P. Anderson Meson Physics Facility in Los Alamos, NM using the LAMPF  $\pi^0$  spectrometer. The target was a 4-inch diameter liquid  ${}^4\text{He}$  cryostat at 4.2K, and solid  $\text{CH}_2$  and graphite targets were used to normalize the data to the known SCX cross section from the free proton. The analysis of the data required modifying the Monte Carlo simulation PIANG<sup>51</sup>, which calculates the geometrical acceptance of the spectrometer, to incorporate significant photon absorption effects due to the cryostat and its support structures.

The data show that SCX in  ${}^4\text{He}$  is dominated by quasifree scattering. This is supported by a comparison between the SCX and inelastic scattering doubly-differential cross sections which revealed the positions and shapes of the quasifree peaks to be in excellent agreement, an indication that the mechanisms behind each are similar. In addition, the magnitudes of the cross sections are in relatively good agreement with the predictions of isospin formalism assuming a single interaction between pion and nucleon. A theoretical calculation based on the DWIA, where single-scattering is assumed, was found to be in good agreement using the IEP with the data at the quasifree peak. At backward angles, the angular distribution agrees roughly with that of SCX from the free proton. Pauli blocking suppresses the cross section at forward angles.

The low-energy part of the spectrum was studied for indications of multiple scattering. There, the DWIA calculation using the IEP disagrees with the data by an order of magnitude at forward angles, an indication of processes other than single-scattering. A comparison of SCX, inelastic scattering, and DCX scaled by predictions from double-interaction isospin formalism are consistent with a double-scattering mechanism at energies below 45 MeV. The prediction that SCX may exhibit additional multiple scattering than inelastic scattering appears to be inconsistent with the data.



To help refine calculations of DCX as resulting from two, sequential SCX reactions, additional data are needed over a wide range of incident and outgoing pion energies and scattering angles. The investigation of issues addressed in this thesis could also be continued. With additional data, the energy dependences of the peak positions and widths, agreement with isospin formalism and theoretical calculations, and indications of multiple scattering could also be studied.



## Appendix A: SCX on a T=0 Pair of Nucleons

Pion scattering on a nucleon pair may proceed through the formation of an intermediate  $\Delta N$  state. In pion SCX, the T=1  ${}^5S_2$   $\Delta N$  state, which is the predominant absorption channel, is forbidden to couple to the  ${}^1S_0$  NN state for low momentum transfer. This intermediate state may only occur through coupling with higher momentum transfer which is energetically less probable. Or SCX may proceed through the formation of other intermediate  $\Delta N$  states which are not as strongly coupled to absorptive processes. As a result, absorption is suppressed, and one may expect that multistep processes in the SCX reaction will not be as strongly truncated as in NCX reactions.

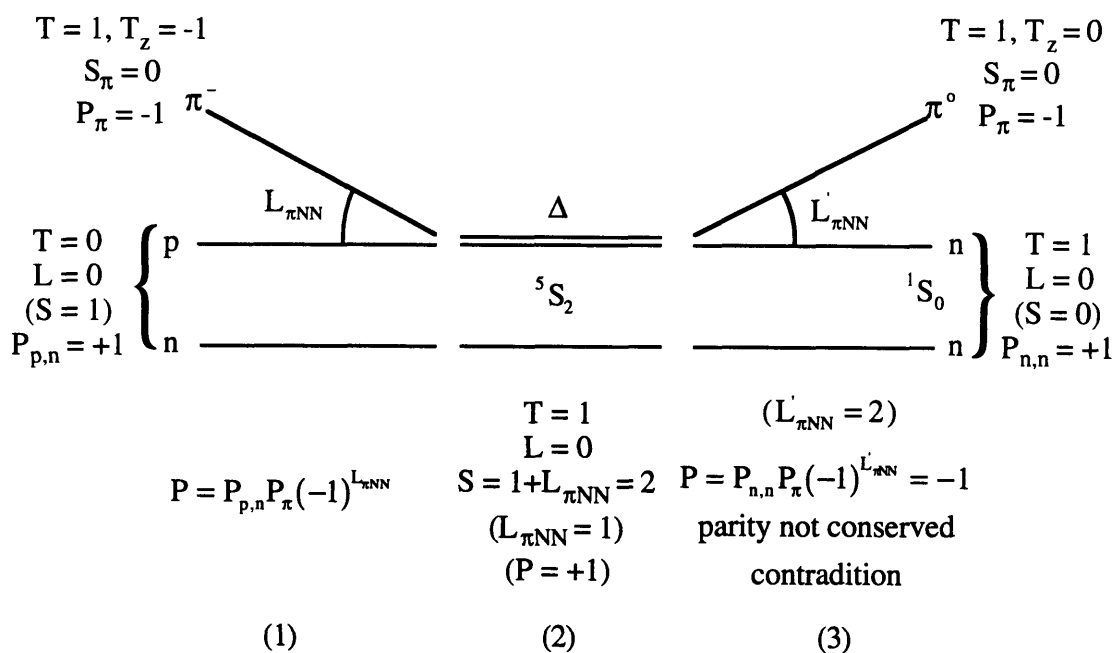


Figure A-1 : Single charge exchange on a T=0 nucleon pair has been split into three stages. At each stage, the values for isospin, orbital angular momentum, intrinsic spin, and parity are given with the deduced quantities in parenthesis. The intermediate T=1  ${}^5S_2$   $\Delta N$  state can not couple to a T=1  ${}^1S_0$  NN final state as argued in the body of the text.

To show why the intermediate T=1  ${}^5S_2$   $\Delta N$  state cannot couple to the  ${}^1S_0$  NN state, the SCX reaction is divided into three parts (figure A-1) which must all have the same total

parity: (1) the initial state of the T=0 two nucleon system and incident pion, (2) the intermediate  $\Delta N$  state, and (3) the final state of the two nucleons and pion following decay of the  $\Delta$ . At the first and third stages, the quantum numbers for angular momentum, parity, and isospin must be such that the two nucleon wavefunction be antisymmetrized, a necessity given that nucleons are spin  $\frac{1}{2}$  particles or fermions.

At stage (1), the assumption is that the two-nucleon pair is in a T=0 configuration, which is antisymmetric with respect to interchange of the two particles. This necessarily means that the two nucleons are a proton-neutron pair, and they are taken to be as in the deuteron ground state with orbital angular momentum L=0. (Note that the particular value of the orbital angular momentum has no bearing on the outcome of the argument, as only the total angular momentum is conserved throughout a reaction; the same conclusion could be reached for L=1 or greater.) To antisymmetrize the two-nucleon wavefunction with respect to isospin, orbital angular momentum, and spin, (i.e.,  $(-1)^{L+S+T} = -1$ ) the total spin must be symmetric, or S=1. The parity of the NN system is  $P_{p,n} = +1$ . When coupled to an incident pion, the total parity of the initial state is  $P = P_{p,n} P_{\pi} (-1)^{L_{\pi NN}}$ , a value which must be conserved across the three phases of the reaction.

The intermediate state (2) is taken to be a T=1  ${}^5S_2$   $\Delta N$  state, an assumption which will lead to a contradiction. Since the total spin S=2, the pion must couple to the nucleons with orbital angular momentum  $L_{\pi NN} = 1$ . This agrees with our understanding of the  $\Delta$ -N interaction, which is known to proceed through a relative p-wave. The total parity of the system, as determined from  $P = P_{p,n} P_{\pi} (-1)^{L_{\pi NN}}$ , must then be  $P = +1$ .

After decay of the  $\Delta$ , the final stage (3) is assumed to include an  ${}^1S_0$  NN state for low momentum transfer. To antisymmetrize the total nucleon wave function, the total spin must be S=0. Given that the pion has no spin, the outgoing pion must decouple from the two nucleons with two units of orbital angular momentum  $L'_{\pi NN} = 2$ . The contradiction reached is that the parity has not been conserved, and the parity of the final state  $P = P_{p,n} P_{\pi} (-1)^{L'_{\pi NN}} = -1$  is not the same as that for stages (1) and (2).

---

## Appendix B: Correction for Ionization Chamber Gating

For the first 79 data runs, the scaler which recorded the ion chamber signal was gated improperly, and the ionization chamber counts for these runs needed to be corrected during data analysis. During data acquisition, pedestal data were taken for approximately the first thirty seconds of the run to establish those parameters and write them to tape before any  $\pi^0$  data were taken. In addition, pedestal data were taken every half-hour, requiring an additional thirty seconds each time. The  $\pi^0$  event trigger was disabled during these periods, to allow for these necessary calibrations. The scaler recording ionization chamber counts, however, incremented during this period, and this was incorrect as it should have been disabled along with the  $\pi^0$  event trigger. This problem was discovered and corrected after run 79, and the ionization chamber scaler was gated properly so as not to increment during the taking of pedestal data. The correction to the ionization chamber scaler counts recorded before run 79 is small, amounting to a few extra seconds of counts for each run. Nonetheless, a precise manner for determining this correction is given below.

The first step in correcting for the additional ionization chamber counts is to determine how many times pedestal data were taken during each run. When pedestal data were taken, an "Event 16" was written to tape to record the newly established parameter values for the pedestals. The number of "Event 16"s for each run ranged from one to four, depending on the duration of the data run.

The next step is to determine the relationship between the corrected ionization chamber counts and the previously incorrectly gated counts. Both these quantities were recorded for the remainder of the experimental run, and each run was sorted by the number of "Event 16"s recorded to tape during the run. As shown in figure B-1, the relationship between both ionization chamber quantities is linear, and the differences in slope between runs with different numbers of Event 16s are slight.

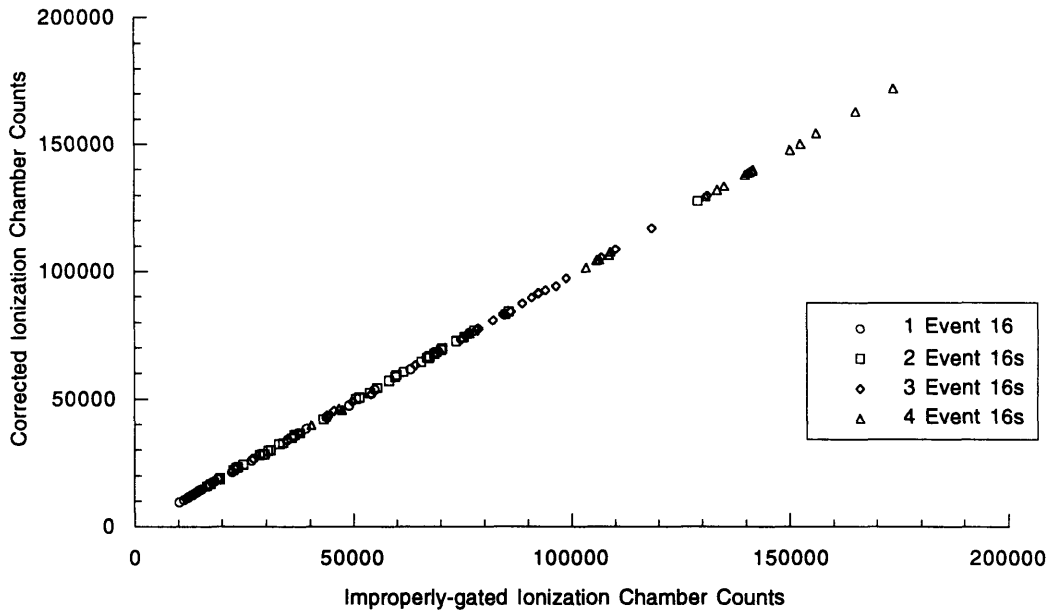


Figure B-1: Linear relationship between the improperly-gated and corrected ionization chamber scalers for all the data runs after run 79. The number of Event 16s is an indication of the number of times pedestal data were taken, which are the periods when the ionization chamber scaler incremented incorrectly.

Ionization Chamber Counts Relationship		
	slope m	intercept b
1 Event 16	0.989	-417
2 Event 16s	0.992	-445
3 Event 16s	0.989	-364
4 Event 16s	0.990	-528

Table B-1: Slope and intercept for least-squares linear fits of the correct ionization chamber scalers as a function of the improperly-gated scalers for all the data runs after run 79. They are grouped by the numbers of Event 16s which were recorded to tape, the periods during which the ionization chamber scalers had been incorrectly allowed to increment. The linear equation is  $y=mx+b$ , where  $x$  is the improperly-gated scaler, and  $y$  is the correction ionization scaler. These values are used to correct the ionization chamber scalers for data runs before run 79.

A least-squares linear fit was made of this relationship for all runs with the same number of Event 16s. The runs were found to have from one to four occurrences of Event 16, and

the slope and intercept for each group are given in table B-1. The intercept values are small compared to typical values of ionization chamber counts ( $\sim 10^5$ ), and the slope is very nearly unity; both quantities reflect the fact that this correction is small. Improperly-gated ionization chamber counts for the first 79 data runs were corrected by using these values.





## **Appendix C: Piang Modification Details**

The cryogenic targets used, both with the nickel vacuum vessel and the modified vessel featuring mylar windows, were modeled in the Monte Carlo simulation PIANG to determine the effects of the material upon the spectrometer's acceptance. The targets were first categorized as rings, cylinders, or domes as shown in figures C-1 and C-2. The large Fe plate of the support stand was modeled as five separate objects as shown in figure C-3. For both vacuum vessels used, the dimensions and laboratory coordinates of these objects are listed in tables C-1 and C-2.

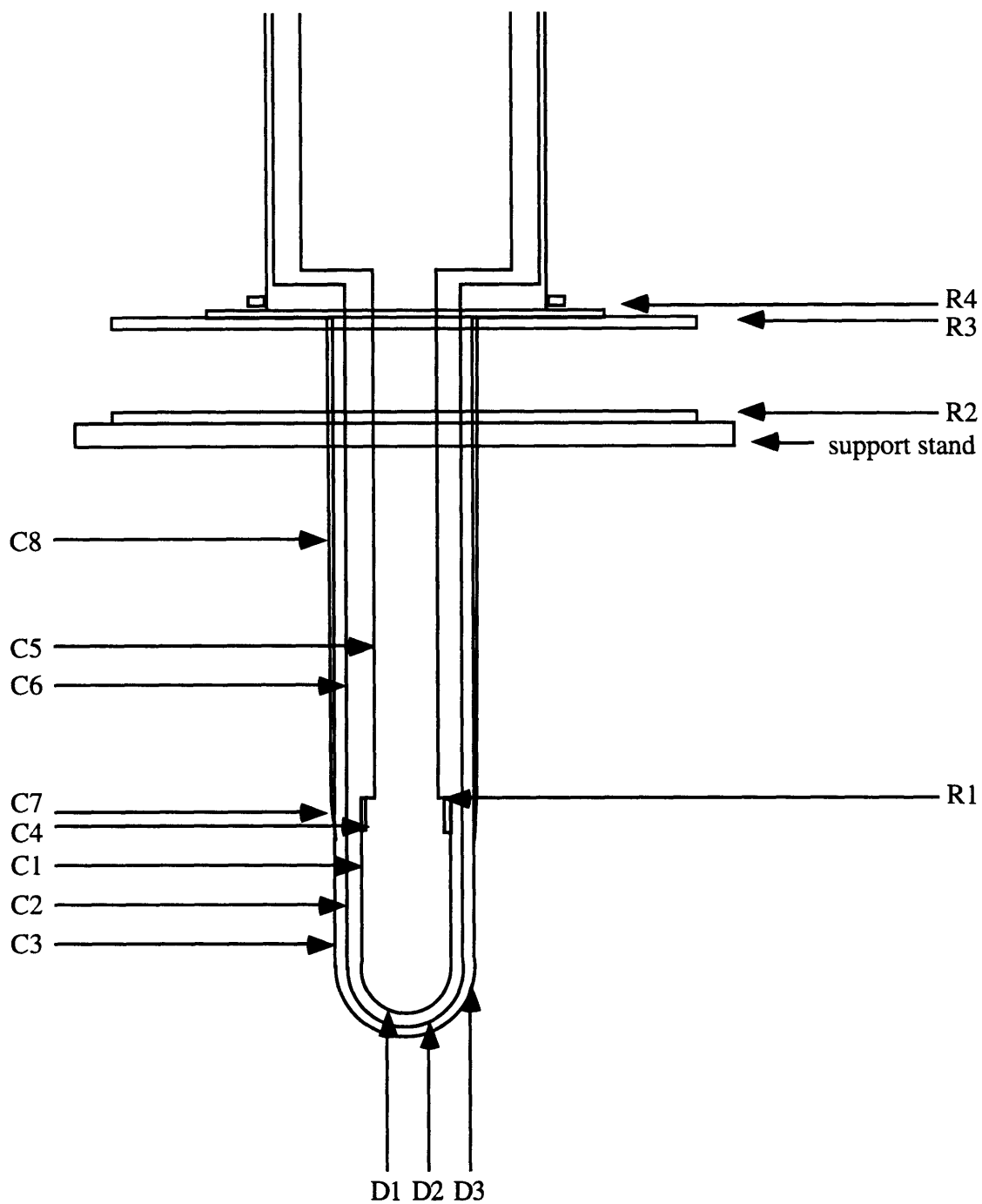


Figure C-1: Diagram of the cryogenic target with the nickel vacuum vessel. The cylinders, rings, domes, and support stand modeled in the Monte Carlo simulation PIANG are labelled.

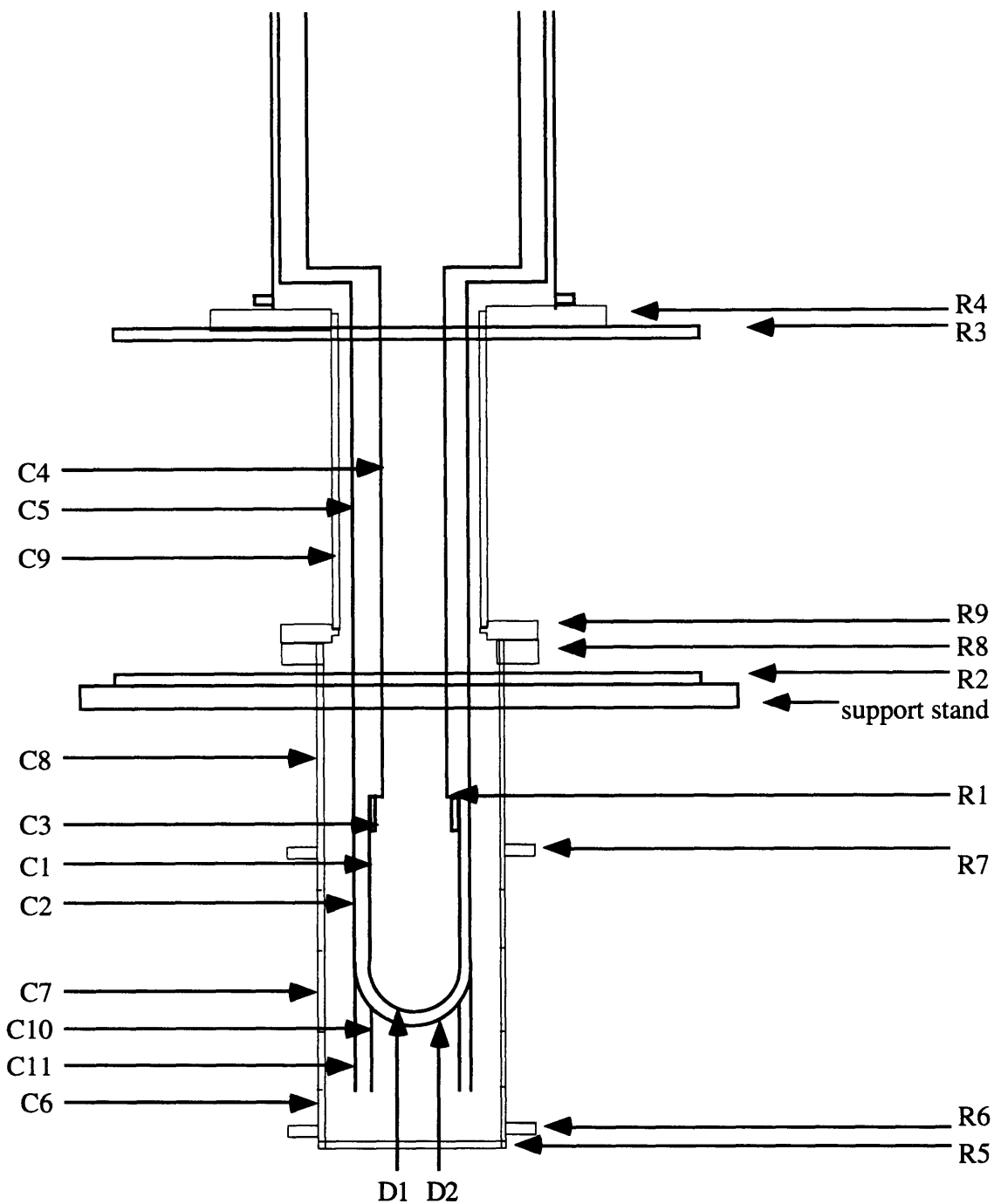


Figure C-2: Diagram of the cryogenic target with the vacuum vessel which featured mylar windows. The cylinders, rings, domes, and support stand modeled in the Monte Carlo simulation PIANG are labelled.

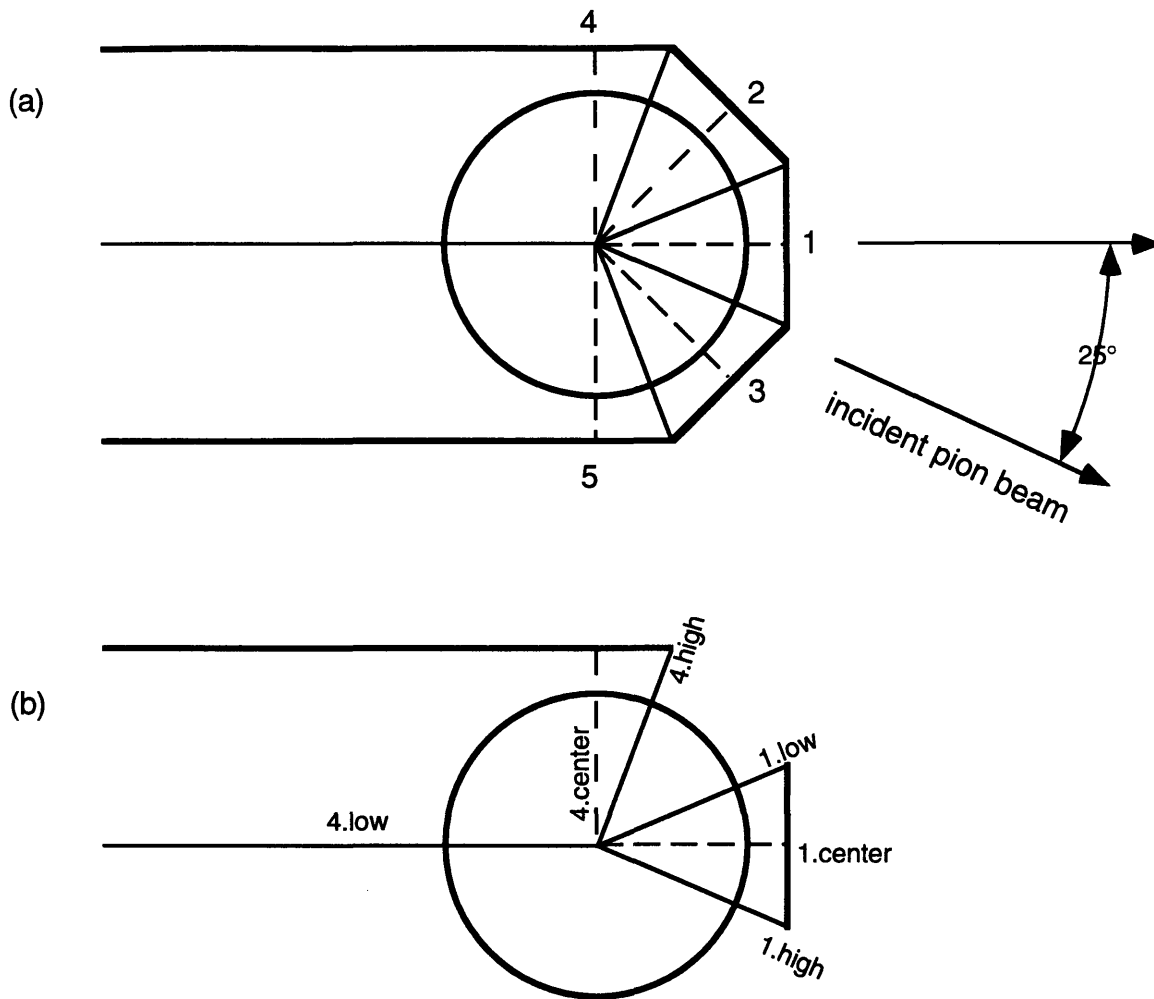


Figure C-3: The large Fe plate of the support stand was modeled as five separate objects, labeled in figure (a). Each object is characterized by three angles with respect to the direction of the incident beam, low, high and the center angle of the normal to the edge. In figure (b), these angles are labeled for objects 1 and 4.

<u>Cylinder</u>	<u>Top</u>	<u>Bottom</u>	<u>Radius</u>	<u>Thickness</u>	<u>Material</u>
C1	3.8	-2.0	2.0	0.005	Ni
C2	3.8	-2.0	2.5	0.002	Ni
C3	3.8	-2.0	3.0	0.020	Ni
C4	5.55	3.8	2.0	0.0625	Fe
C5	23.25	3.8	2.5	0.625	Fe
C6	6.38	3.8	3.0	0.125	Fe
C7	26.0	6.38	3.0	0.25	Fe
C8	26.3	5.55	1.25	0.625	Fe

<u>Ring</u>	<u>Height</u>	<u>Inner Radius</u>	<u>Outer Radius</u>	<u>Thickness</u>	<u>Material</u>
R1	5.55	1.25	2.0	0.09375	Fe
R2	21.5	8.5	12.5	0.5	Al
R3	25.5	6.5	12.5	0.5	Al
R4	26.0	3.0	8.5	0.5	Fe
support stand	20.5			1.0	Fe

<u>Dome</u>	<u>Height</u>	<u>Radius</u>	<u>Thickness</u>	<u>Material</u>
D1	-2.0	2.0	0.005	Ni
D2	-2.0	2.5	0.002	Ni
D3	-2.0	3.0	0.020	Ni

Table C-1: Dimensions and laboratory coordinates of the cylinders, rings, domes, and support stand used to model the cryogenic target with the nickel vacuum vessel. All dimensions are in inches. The top and bottom coordinates of each cylinder are measured with respect to the height of the incident pion beam. The radius of each cylinder is measured to the inside edge of the cylinder material. The heights of each ring and the support stand are measured from the beam height to the lower edges of the objects.

<u>Cylinder</u>	<u>Top</u>	<u>Bottom</u>	<u>Radius</u>	<u>Thickness</u>	<u>Material</u>
C1	3.8	-2.0	2.0	0.005	Ni
C2	3.8	-2.0	2.5	0.002	Ni
C3	5.55	3.8	2.0	0.0625	Fe
C4	26.3	5.55	1.25	0.0625	Fe
C5	26.3	3.8	2.5	0.0625	Fe
C6	-7.25	-9.75	3.75	0.25	Al
C7	-1.25	-4.75	3.75	0.25	Al
C8	12.0	1.25	3.75	0.25	Al
C9	26.125	12.25	3.0	0.25	Al
C10	-2.0	-7.25	2.5	0.002	Ni
C11	-3.5	-7.25	2.0	0.005	Ni

<u>Ring</u>	<u>Height</u>	<u>Inner Radius</u>	<u>Outer Radius</u>	<u>Thickness</u>	<u>Material</u>
R1	5.55	1.25	2.0	0.09375	Fe
R2	9.625	8.5	12.5	0.5	Al
R3	24.875	6.5	12.5	0.5	Al
R4	25.375	3.25	8.5	1.0	Al
R5	-9.375	0.0	3.75	0.375	Al
R6	-8.875	4.0	5.25	0.5	Al
R7	2.75	4.0	5.25	0.5	Al
R8	11.0	4.0	5.5	1.0	Al
R9	12.0	3.25	5.5	0.75	Al
support stand	8.625			1.0	Fe

<u>Dome</u>	<u>Height</u>	<u>Radius</u>	<u>Thickness</u>	<u>Material</u>
D1	-2.0	2.0	0.005	Ni
D2	-2.0	2.5	0.002	Ni

Table C-2: Dimensions and laboratory coordinates of the cylinders, rings, domes, and support stand used to model the cryogenic target with the vacuum vessel which featured mylar windows. All dimensions are in inches. The top and bottom dimensions of each cylinder are measured with respect to the height of the incident pion beam. The radius of each cylinder is measured to the inside edge of the cylinder wall. The heights are measured from the beam height to the lower edges of each ring and the support stand.

## Appendix D: Tables of Cross Sections

Table D-1:  ${}^4\text{He}(\pi^-, \pi^0)\text{X}$ ,  $T_{\pi^-} = 160$  MeV, Spectrometer Nominal Angle  $\theta_{\text{spec.}} = 30^\circ$

$T_{\pi^0}$ [MeV]	$\theta = 22^\circ$	$\theta = 30^\circ$	$\theta = 38^\circ$
	$d^2\sigma / dE_{\pi^0} d\Omega_{\text{lab}}$ [ $\mu\text{b} / \text{MeV} \cdot \text{sr}$ ]	$d^2\sigma / dE_{\pi^0} d\Omega_{\text{lab}}$ [ $\mu\text{b} / \text{MeV} \cdot \text{sr}$ ]	$d^2\sigma / dE_{\pi^0} d\Omega_{\text{lab}}$ [ $\mu\text{b} / \text{MeV} \cdot \text{sr}$ ]
35	1.10 $\pm$ 1.16	1.59 $\pm$ 0.82	0.77 $\pm$ 0.92
40	1.98 $\pm$ 0.70	1.51 $\pm$ 0.52	2.60 $\pm$ 0.57
45	1.86 $\pm$ 0.69	2.37 $\pm$ 0.44	3.14 $\pm$ 0.53
50	2.70 $\pm$ 0.64	2.19 $\pm$ 0.46	1.96 $\pm$ 0.49
55	2.49 $\pm$ 0.73	2.54 $\pm$ 0.50	2.93 $\pm$ 0.56
60	2.61 $\pm$ 0.77	2.83 $\pm$ 0.55	3.09 $\pm$ 0.58
65	1.51 $\pm$ 1.00	3.15 $\pm$ 0.63	2.45 $\pm$ 0.70
70	2.10 $\pm$ 1.09	2.13 $\pm$ 0.82	3.99 $\pm$ 0.82
75	0.82 $\pm$ 1.65	2.55 $\pm$ 1.22	3.16 $\pm$ 1.20
70		6.37 $\pm$ 2.98	2.62 $\pm$ 5.70
75	0.50 $\pm$ 4.09	3.09 $\pm$ 2.25	3.72 $\pm$ 3.24
80	1.59 $\pm$ 3.05	1.52 $\pm$ 1.79	1.83 $\pm$ 2.91
85	1.45 $\pm$ 2.61	5.69 $\pm$ 1.62	3.98 $\pm$ 2.59
90	1.94 $\pm$ 2.55	4.85 $\pm$ 1.73	5.98 $\pm$ 2.48
95	5.74 $\pm$ 2.32	9.53 $\pm$ 1.63	7.92 $\pm$ 2.39
100	5.48 $\pm$ 2.31	11.40 $\pm$ 1.56	12.10 $\pm$ 2.04
105	7.57 $\pm$ 2.40	13.81 $\pm$ 1.46	14.97 $\pm$ 2.10
110	13.18 $\pm$ 2.26	19.78 $\pm$ 1.55	19.54 $\pm$ 2.20
115	13.10 $\pm$ 2.36	23.38 $\pm$ 1.75	30.09 $\pm$ 2.33
120	27.25 $\pm$ 2.78	33.43 $\pm$ 1.81	31.07 $\pm$ 2.62
125	31.50 $\pm$ 3.07	35.56 $\pm$ 2.34	42.45 $\pm$ 2.97
130	33.65 $\pm$ 3.25	37.75 $\pm$ 2.31	40.56 $\pm$ 3.27
135	28.99 $\pm$ 3.67	31.05 $\pm$ 2.30	30.69 $\pm$ 3.01
140	16.97 $\pm$ 3.00	19.46 $\pm$ 1.99	17.02 $\pm$ 2.73
145	15.20 $\pm$ 2.80	4.36 $\pm$ 2.22	8.76 $\pm$ 2.13
150	0.73 $\pm$ 3.15	3.83 $\pm$ 1.99	2.19 $\pm$ 2.02
155	-3.92 $\pm$ 3.69	-1.47 $\pm$ 2.07	-1.38 $\pm$ 1.96
160	-3.41 $\pm$ 3.42	-0.77 $\pm$ 2.20	

The uncertainties listed contain only the statistical uncertainty of this measurement.

Table D-2:  ${}^4\text{He}(\pi^-, \pi^0)\text{X}$ ,  $T_{\pi^-} = 160 \text{ MeV}$ , Spectrometer Nominal Angle  $\theta_{\text{spec.}} = 50^\circ$ 

$T_{\pi^0}$ [MeV]	$\theta = 42^\circ$	$\theta = 50^\circ$	$\theta = 58^\circ$
	$d^2\sigma / dE_{\pi^0} d\Omega_{\text{lab}}$ [ $\mu\text{b} / \text{MeV} \cdot \text{sr}$ ]	$d^2\sigma / dE_{\pi^0} d\Omega_{\text{lab}}$ [ $\mu\text{b} / \text{MeV} \cdot \text{sr}$ ]	$d^2\sigma / dE_{\pi^0} d\Omega_{\text{lab}}$ [ $\mu\text{b} / \text{MeV} \cdot \text{sr}$ ]
35	5.81 $\pm$ 1.42	4.18 $\pm$ 1.16	7.00 $\pm$ 1.42
40	4.64 $\pm$ 0.99	5.05 $\pm$ 0.72	6.31 $\pm$ 0.96
45	3.29 $\pm$ 0.90	4.74 $\pm$ 0.66	6.24 $\pm$ 0.81
50	6.45 $\pm$ 0.77	5.70 $\pm$ 0.61	6.49 $\pm$ 0.78
55	5.12 $\pm$ 0.85	5.20 $\pm$ 0.68	7.86 $\pm$ 0.83
60	5.37 $\pm$ 0.99	6.49 $\pm$ 0.75	6.59 $\pm$ 0.96
65	4.03 $\pm$ 1.10	5.60 $\pm$ 0.86	7.72 $\pm$ 1.05
70	5.86 $\pm$ 1.28	6.22 $\pm$ 1.02	10.97 $\pm$ 1.24
75	6.45 $\pm$ 2.04	6.83 $\pm$ 1.73	8.60 $\pm$ 2.45
70	1.66 $\pm$ 7.27	16.88 $\pm$ 3.51	2.15 $\pm$ 6.54
75	7.10 $\pm$ 4.37	6.54 $\pm$ 2.65	12.84 $\pm$ 4.28
80	6.04 $\pm$ 3.76	6.98 $\pm$ 2.28	5.13 $\pm$ 4.02
85	6.09 $\pm$ 3.17	9.19 $\pm$ 2.16	15.18 $\pm$ 3.33
90	7.55 $\pm$ 2.80	12.68 $\pm$ 2.20	11.50 $\pm$ 3.12
95	10.62 $\pm$ 2.74	16.89 $\pm$ 1.87	17.95 $\pm$ 2.83
100	14.57 $\pm$ 2.69	21.95 $\pm$ 1.80	20.44 $\pm$ 2.64
105	19.68 $\pm$ 2.39	23.20 $\pm$ 1.73	29.13 $\pm$ 2.58
110	29.32 $\pm$ 2.61	29.50 $\pm$ 1.89	35.55 $\pm$ 2.76
115	37.18 $\pm$ 2.89	32.53 $\pm$ 1.98	28.71 $\pm$ 2.74
120	44.32 $\pm$ 3.41	44.90 $\pm$ 2.22	34.87 $\pm$ 2.91
125	46.16 $\pm$ 3.44	38.44 $\pm$ 2.32	35.34 $\pm$ 3.01
130	33.73 $\pm$ 3.46	36.25 $\pm$ 2.37	27.96 $\pm$ 3.08
135	24.97 $\pm$ 3.11	22.94 $\pm$ 1.93	11.46 $\pm$ 1.95
140	12.54 $\pm$ 2.84	6.36 $\pm$ 1.50	-1.17 $\pm$ 1.61
145	3.62 $\pm$ 1.62	2.43 $\pm$ 1.12	1.51 $\pm$ 0.76
150	-0.05 $\pm$ 1.90	0.47 $\pm$ 1.26	1.73 $\pm$ 1.85
155	1.51 $\pm$ 1.08	-2.58 $\pm$ 2.27	
160	1.84 $\pm$ 1.84		

The uncertainties listed contain only the statistical uncertainty of this measurement.



Table D-3:  ${}^4\text{He}(\pi^-, \pi^0)\text{X}$ ,  $T_{\pi^-} = 160$  MeV, Spectrometer Nominal Angle  $\theta_{\text{spec.}} = 80^\circ$ 

$T_{\pi^0}$ [MeV]	$\theta = 72^\circ$	$\theta = 80^\circ$	$\theta = 88^\circ$
	$d^2\sigma / dE_{\pi^0} d\Omega_{\text{lab}}$ [ $\mu\text{b} / \text{MeV} \cdot \text{sr}$ ]	$d^2\sigma / dE_{\pi^0} d\Omega_{\text{lab}}$ [ $\mu\text{b} / \text{MeV} \cdot \text{sr}$ ]	$d^2\sigma / dE_{\pi^0} d\Omega_{\text{lab}}$ [ $\mu\text{b} / \text{MeV} \cdot \text{sr}$ ]
35	1.75 $\pm$ 4.42	14.85 $\pm$ 2.87	11.41 $\pm$ 5.33
40	2.66 $\pm$ 2.35	8.90 $\pm$ 1.81	11.55 $\pm$ 2.67
45	8.57 $\pm$ 1.65	10.72 $\pm$ 1.37	12.20 $\pm$ 1.97
50	13.23 $\pm$ 1.37	12.00 $\pm$ 1.22	15.42 $\pm$ 1.83
55	10.00 $\pm$ 1.51	10.38 $\pm$ 1.27	20.04 $\pm$ 1.84
60	12.10 $\pm$ 1.61	16.47 $\pm$ 1.29	23.94 $\pm$ 1.88
65	12.26 $\pm$ 1.80	16.46 $\pm$ 1.41	25.00 $\pm$ 2.15
70	15.02 $\pm$ 2.01	18.62 $\pm$ 1.77	27.13 $\pm$ 2.42
75	9.73 $\pm$ 3.59	17.83 $\pm$ 2.95	36.79 $\pm$ 3.76
70	9.54 $\pm$ 7.37	27.91 $\pm$ 5.96	20.31 $\pm$ 9.85
75	9.48 $\pm$ 5.13	22.98 $\pm$ 3.85	18.57 $\pm$ 5.94
80	15.22 $\pm$ 4.86	26.84 $\pm$ 3.58	30.83 $\pm$ 5.41
85	17.21 $\pm$ 3.97	30.83 $\pm$ 3.16	30.17 $\pm$ 5.26
90	20.57 $\pm$ 3.72	26.30 $\pm$ 2.81	44.60 $\pm$ 4.72
95	24.44 $\pm$ 3.67	29.24 $\pm$ 2.62	35.61 $\pm$ 4.28
100	28.62 $\pm$ 4.03	32.12 $\pm$ 2.49	38.19 $\pm$ 4.13
105	36.55 $\pm$ 4.37	31.54 $\pm$ 2.58	28.22 $\pm$ 3.70
110	41.91 $\pm$ 4.31	30.97 $\pm$ 2.43	32.37 $\pm$ 3.54
115	39.56 $\pm$ 4.14	31.25 $\pm$ 2.44	32.75 $\pm$ 3.59
120	32.94 $\pm$ 3.84	33.29 $\pm$ 2.59	17.93 $\pm$ 2.81
125	34.36 $\pm$ 3.90	30.71 $\pm$ 2.68	13.54 $\pm$ 2.16
130	17.56 $\pm$ 2.87	10.93 $\pm$ 1.86	0.42 $\pm$ 1.56
135	4.60 $\pm$ 1.52	4.48 $\pm$ 1.26	-0.08 $\pm$ 1.42
140	0.65 $\pm$ 1.19	-1.13 $\pm$ 1.03	0.39 $\pm$ 0.40
145	-1.48 $\pm$ 1.43	0.75 $\pm$ 0.96	-0.53 $\pm$ 1.19
150	-2.04 $\pm$ 1.99	-0.50 $\pm$ 0.96	2.46 $\pm$ 1.24
155	-0.67 $\pm$ 1.94		
160	5.36 $\pm$ 5.39	2.24 $\pm$ 2.24	2.51 $\pm$ 2.51

The uncertainties listed contain only the statistical uncertainty of this measurement.

Table D-3:  ${}^4\text{He}(\pi^-, \pi^0)\text{X}$ ,  $T_{\pi^-} = 160$  MeV, Spectrometer Nominal Angle  $\theta_{\text{spec.}} = 105^\circ$ 

$T_{\pi^0}$ [MeV]	$\theta = 97^\circ$	$\theta = 105^\circ$	$\theta = 113^\circ$
	$d^2\sigma / dE_{\pi^0} d\Omega_{\text{lab}}$ [ $\mu\text{b} / \text{MeV} \cdot \text{sr}$ ]	$d^2\sigma / dE_{\pi^0} d\Omega_{\text{lab}}$ [ $\mu\text{b} / \text{MeV} \cdot \text{sr}$ ]	$d^2\sigma / dE_{\pi^0} d\Omega_{\text{lab}}$ [ $\mu\text{b} / \text{MeV} \cdot \text{sr}$ ]
35	3.65 $\pm$ 3.58	16.60 $\pm$ 2.98	8.94 $\pm$ 4.56
40	11.46 $\pm$ 2.09	13.05 $\pm$ 1.64	16.08 $\pm$ 2.46
45	15.71 $\pm$ 1.64	16.13 $\pm$ 1.33	20.48 $\pm$ 1.94
50	19.12 $\pm$ 1.59	22.12 $\pm$ 1.37	29.47 $\pm$ 1.94
55	19.72 $\pm$ 1.64	26.01 $\pm$ 1.45	34.88 $\pm$ 2.11
60	27.80 $\pm$ 1.97	31.47 $\pm$ 1.64	42.04 $\pm$ 2.44
65	27.77 $\pm$ 2.07	35.81 $\pm$ 1.88	48.97 $\pm$ 2.70
70	34.96 $\pm$ 2.63	43.21 $\pm$ 2.43	59.66 $\pm$ 3.47
75	32.59 $\pm$ 4.05	45.85 $\pm$ 3.88	62.27 $\pm$ 5.49
70	18.03 $\pm$ 16.05	66.71 $\pm$ 9.42	48.85 $\pm$ 16.97
75	21.82 $\pm$ 10.43	52.78 $\pm$ 6.45	53.89 $\pm$ 9.89
80	36.70 $\pm$ 7.04	48.97 $\pm$ 4.68	46.99 $\pm$ 7.59
85	47.67 $\pm$ 6.56	46.25 $\pm$ 4.29	74.50 $\pm$ 7.01
90	49.48 $\pm$ 5.20	43.24 $\pm$ 3.99	58.75 $\pm$ 6.13
95	41.36 $\pm$ 4.70	57.19 $\pm$ 3.47	38.78 $\pm$ 5.09
100	37.66 $\pm$ 3.80	50.10 $\pm$ 3.17	35.53 $\pm$ 5.37
105	45.23 $\pm$ 3.91	33.42 $\pm$ 3.08	36.50 $\pm$ 4.35
110	44.69 $\pm$ 3.46	23.45 $\pm$ 3.03	23.57 $\pm$ 3.95
115	25.64 $\pm$ 3.81	24.06 $\pm$ 2.65	20.35 $\pm$ 3.89
120	23.29 $\pm$ 3.27	16.64 $\pm$ 2.35	12.60 $\pm$ 3.75
125	9.29 $\pm$ 2.76	4.98 $\pm$ 2.08	5.54 $\pm$ 2.62
130	4.06 $\pm$ 1.23	2.37 $\pm$ 1.65	1.08 $\pm$ 2.66
135	-0.03 $\pm$ 2.82	-0.15 $\pm$ 1.61	4.12 $\pm$ 2.26
140	-1.27 $\pm$ 1.82	2.34 $\pm$ 0.78	2.43 $\pm$ 1.09
145		-3.11 $\pm$ 2.45	4.86 $\pm$ 1.72
150		2.24 $\pm$ 2.24	-1.25 $\pm$ 3.13
155			5.00 $\pm$ 5.00
160	6.79 $\pm$ 6.79		

The uncertainties listed contain only the statistical uncertainty of this measurement.

Table D-5:  ${}^4\text{He}(\pi^-, \pi^0)X$ ,  $T_{\pi^-} = 160$  MeV, Spectrometer Nominal Angle  $\theta_{\text{spec.}} = 130^\circ$ 

$T_{\pi^0}$ [MeV]	$\theta = 122^\circ$	$\theta = 130^\circ$	$\theta = 138^\circ$
	$d^2\sigma/dE_{\pi^0}d\Omega_{\text{lab}}$ [ $\mu\text{b}/\text{MeV}\cdot\text{sr}$ ]	$d^2\sigma/dE_{\pi^0}d\Omega_{\text{lab}}$ [ $\mu\text{b}/\text{MeV}\cdot\text{sr}$ ]	$d^2\sigma/dE_{\pi^0}d\Omega_{\text{lab}}$ [ $\mu\text{b}/\text{MeV}\cdot\text{sr}$ ]
35	13.77 $\pm$ 4.62	4.30 $\pm$ 3.83	13.28 $\pm$ 5.20
40	10.68 $\pm$ 2.78	15.22 $\pm$ 2.12	23.73 $\pm$ 3.58
45	18.03 $\pm$ 2.08	23.65 $\pm$ 1.91	30.95 $\pm$ 3.01
50	25.73 $\pm$ 2.15	33.57 $\pm$ 1.91	42.12 $\pm$ 3.18
55	29.11 $\pm$ 2.28	36.74 $\pm$ 2.07	48.81 $\pm$ 3.40
60	42.30 $\pm$ 2.63	46.19 $\pm$ 2.30	55.42 $\pm$ 3.81
65	47.00 $\pm$ 2.98	52.30 $\pm$ 2.60	62.80 $\pm$ 4.32
70	51.88 $\pm$ 3.40	66.98 $\pm$ 3.53	74.86 $\pm$ 5.30
75	45.63 $\pm$ 5.42	45.28 $\pm$ 5.11	63.33 $\pm$ 8.45
70	33.67 $\pm$ 13.85	58.73 $\pm$ 8.19	42.59 $\pm$ 16.95
75	53.44 $\pm$ 8.53	72.77 $\pm$ 5.65	76.37 $\pm$ 10.15
80	62.53 $\pm$ 6.40	62.42 $\pm$ 4.16	53.50 $\pm$ 7.49
85	57.22 $\pm$ 5.34	54.46 $\pm$ 3.45	53.14 $\pm$ 6.30
90	47.71 $\pm$ 4.42	44.19 $\pm$ 2.94	41.57 $\pm$ 5.18
95	45.70 $\pm$ 3.75	35.29 $\pm$ 2.53	29.15 $\pm$ 4.36
100	36.90 $\pm$ 3.23	27.92 $\pm$ 2.29	20.73 $\pm$ 3.81
105	21.23 $\pm$ 3.01	22.55 $\pm$ 2.15	20.64 $\pm$ 3.83
110	21.57 $\pm$ 2.82	11.01 $\pm$ 2.10	15.48 $\pm$ 3.81
115	6.73 $\pm$ 2.38	7.32 $\pm$ 1.96	8.57 $\pm$ 3.64
120	5.60 $\pm$ 2.25	2.67 $\pm$ 1.82	2.03 $\pm$ 3.31
125	0.66 $\pm$ 1.92	0.61 $\pm$ 1.55	2.16 $\pm$ 2.98
130	-1.95 $\pm$ 1.72	-0.23 $\pm$ 1.55	-2.94 $\pm$ 3.19
135	-0.90 $\pm$ 1.78	2.14 $\pm$ 1.62	5.42 $\pm$ 3.02
140	-0.37 $\pm$ 1.96	0.29 $\pm$ 1.67	3.18 $\pm$ 3.57
145	2.45 $\pm$ 1.76	1.41 $\pm$ 2.14	-0.72 $\pm$ 3.07
150		0.31 $\pm$ 1.49	-3.52 $\pm$ 3.29
155	1.36 $\pm$ 3.14	0.96 $\pm$ 1.68	-1.40 $\pm$ 3.50
160		7.39 $\pm$ 7.40	-3.58 $\pm$ 17.59

The uncertainties listed contain only the statistical uncertainty of this measurement.



## Bibliography

- 1 P. A. M. Gram, Nucl. Phys. **A527**, 45c (1991).
- 2 H. Yukawa, Proc. Phys.-Math. Soc. Jpn. **17**, 48 (1935).
- 3 C. M. G. Lattes, H. Muirhead, C. F. Powell, and G. P. S. Occhialini, Nature **159**, 694 (1947).
- 4 D. H. Perkins, Nature **159**, 126 (1947).
- 5 R. Bjorklund, W. E. Crandall, B.J. Moyer, and H. F. York, Phys. Rev. **77**, 213 (1950).
- 6 D.E. Nagle, M.B. Johnson and D. Measday, Phys. Today **56**, April 1987.
- 7 S. Wong, Introductory Nuclear Physics, Prentice Hall, NJ 1990.
- 8 H. L. Anderson, E. Fermi, E. A. Long, and D. E. Nagle, *Phys. Rev.* **85**, 936 (1952).
- 9 J. B. Walters and G. A. Rebka, Jr., SCATPI, A Subroutine for Calculating  $\pi N$  Cross Sections and Polarizations for Incident Pion Kinetic Energies Between 90 and 300 MeV, Los Alamos Technical Report LA-7731-MS (1979).
- 10 R. A. Arndt, J. M. Ford, and L. D. Roper, Phys. Rev. **D32**, 1085 (1985).
- 11 M. Baumgartner *et al.*, Nucl. Phys. **A399**, 451 (1983).
- 12 S. M. Levenson, *et al.*, Phys. Rev. Lett. **47**, No. 7, 479 (1981).
- 13 E. R. Kinney, Ph.D. Thesis, Massachusetts Institute of Technology, (unpublished) 1988; Los Alamos National Laboratory report LA-11417-T (1988).
- 14 A. Stetz, *et al.*, Phys. Rev. Lett. **47**, 782 (1981).
- 15 J. Bernabéu, T. E. O. Ericson, and C. Jarlskog, Phys. Lett. **69B** 161 (1977).
- 16 S.A. Wood, Ph.D. Thesis, Massachusetts Institute of Technology (unpublished) 1985; Los Alamos National Laboratory report LA-9932-T (1983); S.A. Wood, *et*

- al.*, Phys. Rev. Lett. **45**, No.7, 635 (1985).
- 17 F. Lenz, Proceedings of the Topical Meeting on Intermediate Energy Physics, Zuoz, 1976, Vol. 2, p.319.
  - 18 F. Adimi *et al.*, Phys. Rev. C, **45**, 2589 (1992).
  - 19 R.A. Schumacher, *et al.*, Phys. Rev. C **38**, 2205 (1988).
  - 20 D. Ashery *et al.*, Phys. Rev. Lett. **47**, 895 (1981).
  - 21 G. Backenstoss *et al.*, Phys Lett. **B137**, 329 (1984).
  - 22 P. Weber *et al.*, PSI preprint PR-89-03 (1989).
  - 23 U. Sennhauser *et al.*, SIN (PSI) proposal R87-13.1, "Proposal to Study Multi-particle Final States in Pion-Nucleus Reactions with a Large Acceptance Detector (LADS)" (1987).
  - 24 T. Altholz *et al.*, MIT Laboratory for Nuclear Science preprint LNS 94/56. Submitted to Phys. Rev. Lett. on April 6, 1994.
  - 25 H. Weyer, Phys. Reports **195**, No. 6, 295 (1990).
  - 26 D. Ashery, J. P. Schiffer, Ann. Rev. Nucl. Part. Sci. **36**, 207 (1986).
  - 27 M. Y. D. Wang, S.B. Thesis, Massachusetts Institute of Technology, 1987 (unpublished).
  - 28 M. Yuly, Ph.D. Thesis, Massachusetts Institute of Technology, 1993; Los Alamos National Laboratory report LA-12559-T.
  - 29 E. R. Kinney *et al.*, Phys. Rev. Lett. **57**, 3152 (1986).
  - 30 W. Fong, Ph.D. Thesis, Massachusetts Institute of Technology, (unpublished) 1993.
  - 31 D. Ashery *et al.*, Phys. Rev. **C30**, 946 (1984).
  - 32 D. Ashery *et al.*, Phys. Rev. Lett. **50**, No. 7, 482 (1983).
  - 33 M. Thies, Nucl. Phys. **A382**, 434 (1982).

- 34 D. Ashery *et al.*, Phys. Rev. **C23**, 2173 (1981).
- 35 T. J. Bowles *et al.*, Phys. Rev. **C23**, 439 (1981).
- 36 M. D. Cooper *et al.*, Phys. Rev. **C25**, No. 1, 438 (1982).
- 37 M. L. Dowell, Ph.D. Thesis, Massachusetts Institute of Technology, (unpublished) 1993.
- 38 *LAMPF Users Handbook*, Report No. MP-DO-3-UHB, Los Alamos National Laboratory, Los Alamos, New Mexico, 1984.
- 39 B. J. Dropesky *et al.*, Phys. Rev. C **20**, 1944 (1979).
- 40 G. W. Butler *et al.*, Phys Rev. C **26**, 1737 (1982).
- 41 G. Friedlander, Kennedy, and Miller, Nuclear and Radiochemistry, 2nd ed, pp. 420-424, Wiley and Sons, New York, 1964.
- 42 H. W. Baer *et al.*, Nucl. Instrum. and Methods **180**, 445 (1981).
- 43 S. Gilad *et al.*, Nucl. Instrum. and Methods **144**, 103 (1977).
- 44 S. Gilad, Ph.D. Thesis, Tel-Aviv University (unpublished) 1979.
- 45 Digital Equipment Corporation
- 46 R. D. Bolton *et al.*, Nucl. Instrum. and Methods **174**, 411 (1980).
- 47 Program NCA by T. Kozlowski, Los Alamos National Laboratory, Los Alamos, New Mexico, 1982 (unpublished).
- 48 Notes by H. W. Baer, Los Alamos National Laboratory, Los Alamos, New Mexico, 1985 (unpublished).
- 49 Program HOT by G. T. Anderson, Los Alamos National Laboratory, Los Alamos, New Mexico, 1982 (unpublished).
- 50 J. Ouyang, Ph.D. Thesis, University of Colorado (unpublished) 1992; Los Alamos National Laboratory report LA-12457-T (1992).

- 51 Program PIANG by H. W. Baer, Los Alamos National Laboratory, Los Alamos, New Mexico, 1986 (unpublished).
- 52 S. Høibråten, Ph.D. Thesis, M.I.T. (unpublished), Los Alamos Scientific Laboratory Report LA-11582-T (1989).
- 53 Program PIANG920 by H.W. Baer, modified by Z. Shariv, Los Alamos National Laboratory, Los Alamos, New Mexico, 1986 (unpublished).
- 54 Z. Shariv, *Modification of the PIANG86.FOR Program, Exp. 920/921 1986?* (unpublished).
- 55 Berger, M.J., and Hubbell, J.H., Photon Attenuation Coefficients, CRC Handbook of Chemistry and Physics, 74th Ed., 10-282, CRC Press (1993).
- 56 H. W. Baer, *et al.*, Nucl. Instr. and Meth. 180, **445** (1981).
- 57 The converter planes in the spectrometer were changed after publication of Ref. 42. Updated information is found in S.H. Rokni, Ph. D. Thesis, Report No. LA-11004-T, Los Alamos National Laboratory, Los Alamos, New Mexico, 1987.
- 58 R. A. Arndt and L. D. Roper, *Scattering Analysis Interactive Dial-in*, Report No. CAPS-80-3 (rev), Center for analysis of Particl Scattering, Virginia Polytechnic Institute and State University, Blacksburg, Virginia, 1983.
- 59 R. A. Arndt, J. M. Ford, and L. D. Roper, Phys. Rev. D **32**, 1085 (1985).
- 60 G. Jacob and T.A.J. Maris, Rev. Mod. Phys. **38**, 121 (1966).
- 61 G. Jacob and T.A.J. Maris, Rev. Mod. Phys. **45**, 6 (1973).
- 62 N. S. Chant, L. Rees, and P. G. Roos, Phys. Rev. Lett. **48**, 1784 (1982).
- 63 M.A. Khandaker, Ph.D. Thesis, University of Washington (1987).
- 64 M.A. Khandaker, *et al.*, Phys. Rev. C **44**, 24 (1991).
- 65 J. M. Eisenberg and D. S. Koltun. *Theory of Meson Interactions with Nuclei*. John Wiley and Sons, New York, 1980.



- 66 N. S. Chant and P. G. Roos, Phys. Rev. **C15**, 57 (1977).
- 67 J. M. Grebe, Phys. Lett. **115B**, 363 (1982).
- 68 E.H. Auerbach, D.M. Fleming, and M.M. Sternheim, Phys. Rev. **162**, 1683 (1967).
- 69 S. Fiarman, W.E. Meyerhof, "Energy Levels of Light Nuclei A=4," Nucl. Phys. **A206**, 1 (1973).
- 70 C.M. Lederer, ed., Table of Isotopes, 7th ed., Wiley-Interscience, New York, 1978.



## Biographical Note

Mark Yu Da Wang was born on December 28, 1965 in Troy, New York. He lived in Troy, Loudonville, and Latham, New York before moving to Oklahoma and graduating in 1983 from Norman High School. He continued his education at the Massachusetts Institute of Technology, where he was awarded the 1986 Joel Matthew Orloff UROP Prize for his work under Professor Matthews that became the basis for his bachelor's thesis entitled "Inclusive Pion Double Charge Exchange in Helium-3 in the  $\Delta$ -Resonance Region." He received S.B. degrees in mathematics and physics in May 1987. He continued as a graduate student at MIT, where he was a National Science Foundation Graduate Fellow and full-time research assistant participating on experiments at both the Bates Linear Accelerator in Middleton, Massachusetts, and at the Clinton P. Anderson Meson Physics Facility (LAMPF) in Los Alamos, New Mexico.

Music is a serious pursuit, as he has been a concerto soloist on both the piano and violin, and a violinist in the MIT Symphony and community orchestras in the Boston area. While an undergraduate, he served as an Entry chairman at MacGregor House and taught Boston-area high school students weekend physics and math team problem solving classes. As a graduate student, he spent four years as a graduate resident tutor at Baker House, MIT, where he authored the GRT manual, a residential guide for undergraduates, and edited the tutor newsletter "True GRiT." In 1992 and 1993, he was awarded the William L. Stewart, Jr. Award for his work in extracurricular activities, and in 1994, he received the Karl Taylor Compton Prize for citizenship and dedication to the welfare of the Institute. He was recently elected to serve a five-year term as a member of the MIT Corporation. He has accepted a position with the RAND Corporation in Santa Monica, California as a public policy analyst.